Development of lithium sulphur battery and insights into its failure mechanism

Assiya Yermukhambetova

A thesis submitted to University College London
for the degree of Doctor of Philosophy

Department of Chemical Engineering
Torrington Place, WC1E 7JE

May 2017

Declaration

I, Assiya Yermukhambetova, confirm that the work presented in this thesis is my own. Where information has been derived from other sources, I confirm that this has been indicated in the thesis.

Signature

May 2017

Abstract

Lithium–sulphur batteries are considered as a promising battery system due to its high theoretical capacity (1675 A h kg^{-1}), high energy density (~2500 W h kg^{-1}) and the natural abundance of sulphur. However, despite intensive research there are certain limitations to be overcome to bring Li/S to practical application; these limitations stem from the multiple reactions and phase changes in the sulphur cathode.

Herein, for the first time to author's knowledge, the effect of the cathode morphology as a function of charge cycles was studied by a multi-scale 3D *in-situ* X-ray tomography approach. The microstructural evolution within the same Li/S cell is studied without disrupting the contents and revealing significant changes to the electrode morphology. The uneven distribution of the sulphur phase fraction within the electrode thickness and sulphur agglomeration upon cycling were shown. The advantages of *in-situ* X-ray tomography are compelling, enabling a non-destructive imaging of battery.

Furthermore, the strategies for Li/S optimisation were reflected. A comparative study of the effect of widely available conducting polymers: polyacrylonitrile and polyaniline; and metal oxide additives: $Mg_{0.6}Ni_{0.4}O$ and Al_2O_3; on the Li/S performance, both capacity and cycle life was conducted. Commercially viable cell configurations were developed by a simple ball milling followed by a heat treatment; the best performance was by S/PANI/ $Mg_{0.6}Ni_{0.4}O$ composite with an initial discharge capacity of 1500 mA h g^{-1}.

Many problems arise due to polysulphides solubility; therefore, the optimised cathode was tested with electrolytes to investigate the effect of high concentration and viscosity, as well as $LiNO_3$ addition. It was shown that although increasing the electrolyte concentration leads to the higher battery performance and stability, the similar results could be achieved with the addition of $LiNO_3$.

Generally, it was shown the tailoring electrolyte and electrodes parameters for Li/S cell is as important as development of efficient and easy scale-up S electrodes.

.

Acknowledgements

Firstly, I would like to thank my supervisor, Dr. Paul Shearing, for his guidance, patience and encouragement, Dr. Dan Brett for his support and opportunity to join a great group of people in Electrochemical Innovation Lab.

I enjoyed being there and my further thoughts to the people with whom I probably spent most of time in this "PhD journey": to all members of the Electrochemical Innovation Lab. Special thanks to Dami for his helpful comments and suggestions, especially during the first stage of this work, to Aliya, Quentin and Alvin for their support. I am indebted to Toby for his assistance and spending his time to resolve any technical issues, to Leon, Tan for their valuable input, Donal and Bernard for their valuable comments on tomography aspects, Jay for solving many important lab issues and making things possible. Thank you to the Staff of Chemical Engineering Department.

Special thanks to Chun and Sohrab for their enormous contributions to the tomography work.

Thank you to all of you, I have thoroughly enjoyed working under Dr Shearing's supervision with such a great group of people.

I am grateful to Dr. Zhumabay Bakenov from Nazarbayev University for his invaluable support, guidance and introduction to the "battery world". Thanks to the members of Battery Research Group in Nazarbayev University: Murat and Aishuak for sharing with me your practical expertise.

Last but not least, I am grateful to my family for unconditional love and support throughout my PhD.

I would also like to thank Nazarbayev University for the financial funding of my PhD studies.

Table of Contents

LIST OF FIGURES

LIST OF TABLES

LIST OF ABBREVIATIONS

AC	Alternating current
AB	Acetylene black
AFM	Atomic force microscopy
BET	Brunauer Emmett Teller method
C	C-rate
CCD	Charge coupled device
CMC	Carboxyl methylcellulose
CT	Computer tomography
CV	Cyclic voltammetry
DC	Direct current
DEC	Diethyl carbonate
DMC	Dimethyl carbonate
DME	Dimethoxyethane
DOD	Depth of discharge
DOL	1,3-dioxolane
ξ_{col}	Coulombic efficiency
E, V	DC potential
EC	Ethylene carbonate
EDS	Energy dispersive X-ray Spectroscopy
EV	Electric vehicle
ϕ**, radians**	Phase shift
F	Faraday's constant, 96 485 C mol^{-1}
FIB	Focus ion beam
FTIR	Fourier Transform Infra red Spectroscopy
I, A	Current
I	Beams intensity after it traverses a thickness of material
I_0	Intensity of the incident X-ray
I(0), A	Amplitude of the signal

I(t), A	Instantaneous current
KB	Ketjen black©
Li/S	Lithium sulphur
LiB	Lithium ion battery
$\boldsymbol{\mu}$	Coefficient ,which is inversely related to the mean free path of the beam
$\boldsymbol{n}$	Number of electrons
NiCd	Nickel cadmium battery
NiMH	Nickel metal hydride battery
NMP	N-methyl-2-pyrrolidone
NWC	Non-woven carbon
OCV	Open circuit voltage
PAN	Polyacrolnitrile
PANI	Polyaniline
PC	Propylene carbonate
PEO	Polyethylene oxide
PPy	Polypropylene
PVdF	Poly (vinylidene fluoride)
Q_1 and Q_2, µF	Constant phase elements
$\boldsymbol{Q_T}$**, A h g^{-1}**	Theoretical capacity
$\boldsymbol{Q_p}$**, A h g^{-1}**	Practical capacity
R, Ω	Resistance
R_1, Ω	the internal resistance of the battery
R_2 and R_3, Ω	the passivation film and charge-discharge transfer
RPM	Revolutions per minute
SEI	Solid electrolyte interface
SEM	Scanning electron microscopy
t, s	Time
TEGDME	Tetra(ethylene glycol) dimethyl ether
TEM	Transmission electron microscopy

THF	Tetrahydrofuran
VACN	Vertically aligned carbon nanotubes
UV-vis	Ultraviolet–visible spectroscopy
W, Ω $s^{-1/2}$	Warburg impedance
x	Linear attenuation coefficient
XAS	X-ray absorption spectroscopy
x	theoretical number of moles of reaction associated with the complete discharge of the cell
XRD	X-ray diffraction
XRM	X-ray microscopy
X-ray CT	X-ray computer tomography
***ω*, radians per s**	frequency
Z	Complex impedance

CHAPTER I: INTRODUCTION

1.1 Motivation

In the past decade, the rapid development of a wide variety of electronics consumer products has led to the need for battery systems with a much higher energy per unit volume and superior discharge characteristics.

Furthermore the oil crisis and serious global environmental problems have brought into question the reliability on fossil fuels and this has led to the development of renewable energy sources, such as wind, solar, tidal. This also requires high performance energy storage technologies that can meet requirements for large-scale applications such as high energy density, environmentally friendliness and low cost. Moreover, the electrification in the transportation sector is crucial for future mobility to reduce the dependence on oil and minimize emissions.

In this light, energy storage systems are becoming one of the most important elements of smart grids and low-carbon transport; they can be utilised to store, normalize and efficiently deliver the energy produced by various means including alternative energy sources: this is considered to be a key factor in the sustainable development of modern society [1].

Among all of available energy storage systems technologies, the most attractive one is based on lithium. The interest in lithium-ion batteries (LiB) is growing because of their high gravimetric and volumetric energy densities [2], [3]. Commercialized since 1991 (by Sony), the LiB offer much better performance compared to other rechargeable systems (Pb, Ni-Cd, Ni-MH) and thus, are already widely used in

electronics [1]. Market shares in MW h, were ca.16% (40% in U.S. dollars) in 1999 rising to nearly 82% (75% in U.S. dollars) in 2010, reflecting the rise of popularity of this technology [4]. This interest in LiB is accentuated by the massive development of electric and hybrid vehicles. In fact, this technology is foreseen to equip the next generation of vehicles, due to its performance and is predicted to become the dominant technology for EVs just as it has become the leading battery technology for consumer electronics [5].

LiB technologies are successfully employed in electric vehicle and below a list (Table 1.1) of some companies which employed LiB in EV cars is presented. [5]

Table 1.1 Some current EV and the employed battery systems (*Source* [5])

Vehicle	**Battery supplier**	**LiB Positive/negative electrode**
Nissan Leaf EV	Automotive Energy Supply (Nissan NEC JV)	Graphite/$LiMn_2O_4$
Chevrolet Volt	Compact Power (subsidiary of LG Chem)	Graphite/$LiMn_2O_4$
Renault Fluence	Automotive Energy Supply (Nissan NEC JV)	Graphite/$LiMn_2O_4$
Tesla Roadster	Panasonic Energy	$LiNi_{0.8}Co_{0.15}Al_{0.05}O_2$ /C
BYD E6	BYD	$LiFePo_4$/C
Honda Fit EV	Toshiba Corporation	$LiCo_xNi_yMn_zO_2$/ $Li_4Ti_5O_{12}$

Thus, the LiB are gradually replacing nickel based batteries, which have equipped the majority of electric and hybrid vehicles since the 1990s (mainly Ni-MH) [6].

However there are certain limitations in existing LiB technologies, which are mainly the cost of components and assembly technology, and the limit of energy density (200–250 W h kg^{-1}) which is not sufficient to meet electric vehicle battery requirements for extended ranges [2], [3], [5]. In order, amongst other things, to

extend the autonomy of electric vehicles, research is turning to the use of new chemistries based on lithium, which offer higher potential for Li-ion systems.

The Lithium/Sulphur system (Li/S) is one of such technologies (**Fig. 1.1**), and is the subject of active research [7], [8].

In **Fig. 1.2** a comparison of available battery systems in terms of specific energy densities is presented, showing that theoretically, the Li/S battery could achieve ca. 2500 W h kg^{-1} [8]–[11].

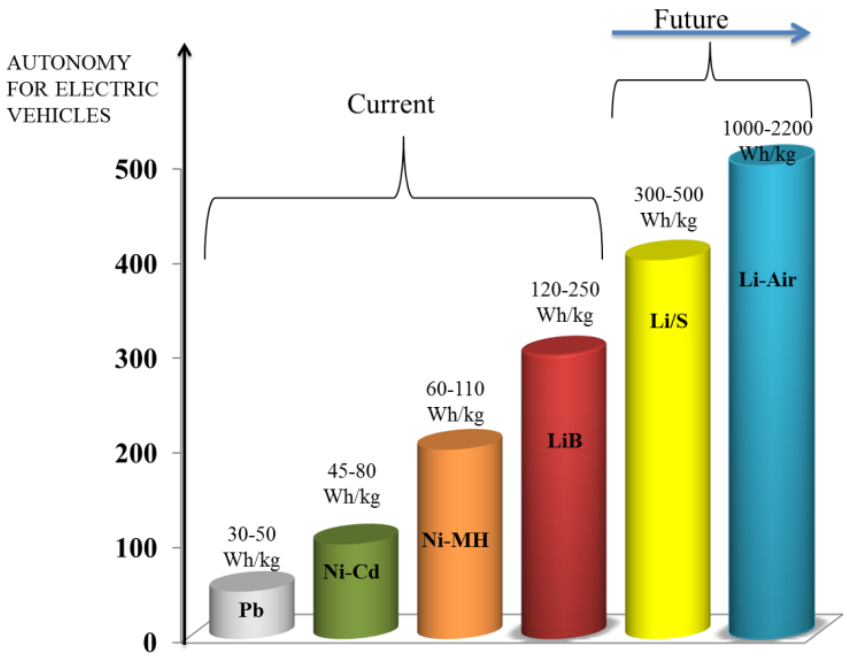

Ni-Cd: Nickel-Cadmium; **Ni-MH**: Nickel-Metal Hydride; **LiB:** Lithium ion Battery; **Li/S**: Lithium-Sulfur Battery, **Li-Air**: Lithium-Air Battery

Figure 1.1 Comparison of alternative battery technologies versus the existing commercial systems in terms of specific energy density converted into kilometers of autonomy for electric vehicles

The use of such a system could, if it reaches maturity, more than double automobile range obtained by LiBs and also lighten vehicle weight. The use of elemental sulphur as an active material, has the advantage of being both abundant and cheap, compared to the conventional materials of LiB [11].The decrease in the cost of the active

material at the positive electrode is expected to reduce the total cost of battery manufacturing, thus the Li/S battery appears to meet both criteria of cost and energy/power density, required for electric vehicle applications. The demand for Li/S battery technologies, as a promising alternative for LiB, has led in recent years to increasing attention from research groups worldwide, and has attracted significant investment for international research agencies including the US DoE [12] and Japanese NEDO [13].

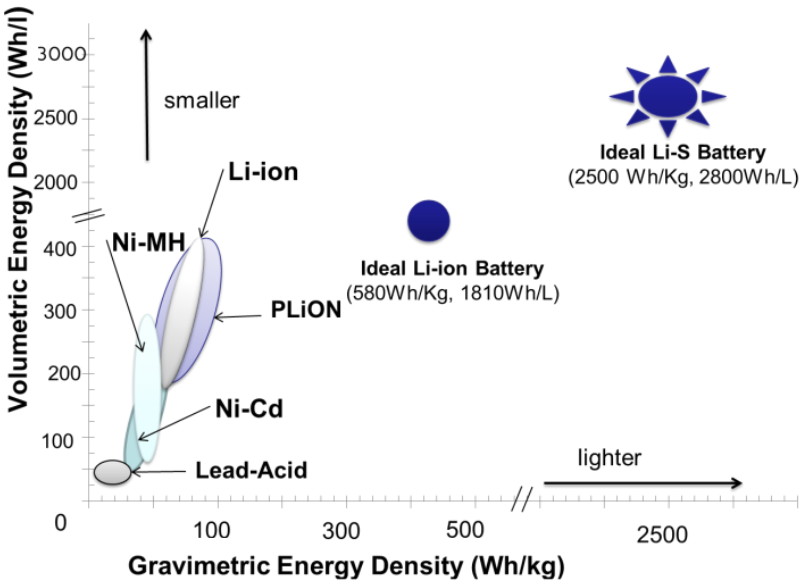

Ni-Cd: Nickel-Cadmium; **Ni-MH**: Nickel-Metal Hydride; **Li-ion:** Lithium ion; **PLiON**: Plastic Li-ion; **Li/S**: Lithium-Sulfur Battery, **Li-Air**: Lithium-Air Battery

Figure 1.2 Comparison of gravimetric and volumetric energy density

There is also active commercial R&D in this area: in 2012, the US based company Sion Power announced 50 million U.S. dollars equity investment from BASF, which is targeting the automotive market, Sion power has also successfully implemented a Li/S battery with the specific energy of 350 W h kg^{-1} in unmanned aerial vehicle in 2010 [14].

UK based company Oxis energy holds numerous patents on Li/S batteries, and also claim that their developed Li/S battery technology is safe and stable and is therefore

expected to be close to commercialization [15], [16]. Other international battery market key companies such as South Korea's Samsung, Japan's Sony, Germany's Bosch and BASF, and PolyPlus of the USA are also very active in the field, as evidenced by numerous patents currently held by these companies.

However, despite the intensive attention of the electrochemistry community for many years the reported practical specific energy at the prototype level is 350 W h kg^{-1}[14]. There are certain issues [17]–[19] that have to be overcome: mainly Li/S batteries suffer from rapid capacity fading and the practical capacity and cycle life of Li/S cells are usually lower than expected. Most of these issues arise due to high solubility of intermediates that leads to a parasitic reaction on the metallic-lithium anode and the accompanied "sulphur shuttle mechanism". This phenomenon decreases the active mass utilization in the discharge process and reduces the coulombic efficiency in the charge process [20]. Moreover, lithium polysulfide intermediates can spontaneously diffuse in the separator, thus leading to cell self-discharge and increase in electrolyte viscosity.

The listed issues are not new and have been intensively studied and numerous different approaches have been employed, mostly either on the positive electrode morphology or on the organic electrolyte composition which will be discussed further in chapter 2.

1.2 Battery Principles of operation

A brief introduction to batteries is given here. Unless otherwise stated, the concepts presented in this section are from the references [1], [21]–[24].

A battery is a device which enables the chemical energy contained in its active materials to be converted directly into electric energy by means of electrochemical oxidation – reduction reaction.

Batteries are widely applied as (1) portable electric power sources ranging from the small button cells used in watches to the lead-acid batteries used in vehicles with internal combustion engines; and as (2) energy storage systems since certain

electrochemical systems have an ability to store electrical energy from external source. The second application is becoming more important since such battery systems could be used for electric vehicles, as part of an electricity supply system to leverage load or in conjunction with renewable energy systems.

A battery is composed of several electrochemical cells that are connected in series and/or parallel to provide the required voltage and capacity, respectively. Each cell consists of a positive and a negative electrode (both sources of chemical reactions) separated by an electrolyte solution containing dissociated salts, which enable ion transfer between the two electrodes. An ideal combination of anode and cathode materials should give a high cell voltage and capacity and to be as light as practical.

The choice of anode based on high energy content, good conductivity, stability and low cost. Mostly metals are used as the anode material since the main requirement is the high energy content. As for the lithium-ion batteries due to safety issues the metal anode is replaced by Li containing compounds, such as Li intercalated in graphite. The choice of cathode is more flexible and based on its efficiency as an oxidizing agent, stability in contact with electrolyte and useful voltage window. The electrolyte has to have sufficient ionic conductivity, be non-reactive with electrodes, stable across a wide temperature range, safe and low cost. A separator is used in order to prevent short-circuiting and a current collector is attached to each electrode.

There are two major types of batteries:

a) Primary batteries, i.e. alkaline battery, aluminum battery, zinc-air battery, zinc-carbon battery, zinc-chloride battery etc.;

b) Rechargeable secondary batteries i.e. lead-acid battery, lithium air battery, lithium -ion battery, lithium-sulphur battery, Ni-MH, Ni-CAD, nickel-zinc battery, polymer-based battery etc.

Among all batteries systems, LiB can supply higher energy density as lithium is the most electropositive (-3.04 V v.s. standard hydrogen electrode) and the lightest metal ($M = 6.94$ g mole^{-1}).

1.3 Battery characteristics and performance criteria

1.3.1 Main characteristics

A battery may be characterised in terms of its available capacity, energy and power it can deliver. These characteristics are determined by the chemical properties of each component of the cell.

The amount of electrical energy, expressed either per unit of weight (W h kg^{-1}) or per unit of volume (W h l^{-1}), that a battery is able to deliver is a function of the cell potential (V) and capacity (A h kg^{-1}) and coulombic efficiency (%) that is determined by the internal resistance of a battery cell.

1.3.1.1 Capacity

The *theoretical capacity* (Q_T) of the cell of half-cell may be calculated as (2.1)

$$\mathbf{Q_T = x(nF)} \qquad \textbf{(2.1)}$$

where x – theoretical number of moles of reaction associated with the complete discharge of the cell, using the lower of the anode or cathode quantities;

n – number of electrons;

F – Faraday's constant, the magnitude of electric charge per mole of electrons, 96 485 C mol^{-1}

The *practical capacity* (Q_p) is lower than Q_T if utilization of electroactive material is not complete (less than 100 %) due to, for example, side reactions that consume some of the reactants.

The *coulombic efficiency* ($\boldsymbol{\xi_{col}}$) of the cell is defined as (2.2)

$$\boldsymbol{\xi_{col} = \frac{Q_p}{Q_T}} \qquad \textbf{(2.2)}$$

Coulombic efficiency is not always 100 % and may reach lower values due to losses in charge, such as the electrolysis of water or other redox reactions in the battery. The losses that reduce coulombic efficiency are primarily due to the loss in charge, largely caused by secondary reactions in the battery.

The irreversible capacity loss is defined as the difference between charge and discharge capacity of the same cycle.

In general, the coloumbic efficiency in LiB for the first cycle is low, therefore there is a high level of irreversible capacity. Desirably the value of irreversible capacity needs to be as low as possible. It is known that the irreversible capacity in the first cycle corresponds to the reductive decomposition of the electrolyte on the anode surface or the formation of so-called solid electrolyte interphase (SEI) layer. This value also depends on the morphology and composition of the electrode, such as for graphite electrodes it was found that the irreversible capacity is in linear relation to the specific surface area of the electrode: the smaller the surface area, the less is irreversible capacity loss.

For comparative purposes it is convenient to calculate specific capacity in terms of mass of the cell or half-cell and usually is given by A h kg^{-1} or A h g^{-1}.

1.3.1.2 Energy

The *gravimetric energy density*, in W h kg^{-1}, corresponds to the amount of stored energy per unit mass of battery. The *volumetric energy density* is also an important parameter, and is typically expressed in W h L^{-1}. They are themselves dependent on the mass storage capacity of the electrodes and the discharge voltage of the accumulator.

1.3.1.3 Power

The *specific power* corresponds to the amount of power delivered by a cell or battery to its weight, W kg^{-1}.

The *power density* is the ratio of power available from a battery related to its volume, W L^{-1}.

1.3.2 Performance criteria

There following criteria need to be satisfied prior successful battery commercialization:

- **High Energy Density:** Total amount of energy that can be stored per unit mass or volume.
- **High Power Density:** Maximum rate of energy discharge per unit mass or volume. The electrode should have high electronic conductivity and ionic conductivity in order to support high current density.
- **Safety:** At high temperatures, certain battery components will breakdown and can undergo exothermic reactions which need to be mitigated for safe operation
- **Cycle Life:** Stability of energy density and power density with repeated cycling is needed for the long life required in many applications.
- **Cost:** Must compete with other existing energy storage technologies.
- **Mechanical and Chemical Stability:** The electrodes must maintain their mechanical properties and chemical composition, structure and surface over time and temperature in the operating environment. Mechanical and chemical stability limitations come from reaction of electrolyte, phase change, corrosion and poor conductivity of materials in the discharged state.
- **Temperature range of operation**: The operating temperature range of a battery is between −50 °C to 80 °C for automotive and military applications. For a general application, the range is between 0 °C to 40 °C. The organic electrolyte and electrolyte interfaces will limit the performance of batteries operated at extreme conditions.
- **Shape of the discharge curve**: For operation of an electronic device, a flat voltage plateau is desirable. A sloping curve is preferred for applications when determining the state of charge is important. The shape of curve is determined by the one (sloping) or two-phase reactions (plateau).

1.4 Lithium ion battery

The primary lithium battery had been developed in 1970's. However, the lithium secondary battery utilizing metallic Li had severe safety problems due to dendrite formation of lithium metal during charge process that led to several accidents. In the

late 1970's a new "Rocking chair" concept was proposed and lately demonstrated by several research groups[25], [26]. This concept was applied by Japanese companies Sony and Sanyo following the fundamental researches by Goodenough [27] and Armand [28]. In 1990's, lithium ion battery had commercialized by Sony Energytech based on a carbon (non-graphitic) as an anode and $LiCoO_2$ as a cathode, that now dominates the market.

During charging, lithium is deintercalated from the cathode layers, then transported and intercalated into the carbonaceous anode (**Fig. 1.3**). In the discharge process, the lithium ions are deintercalated from the anode and intercalated again to the empty octahedral site between layers in the cathode.

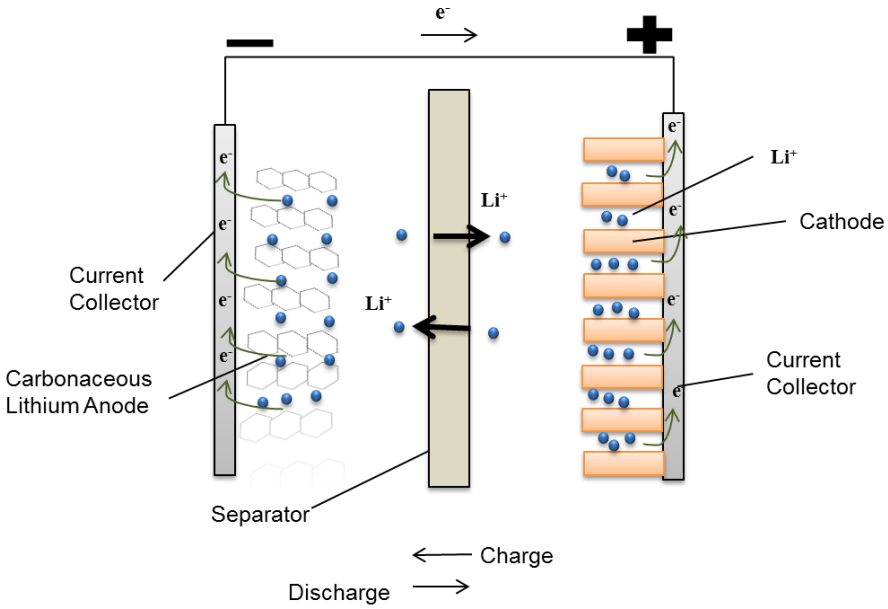

Figure 1.3 Schematic representation of Lithium ion battery charge-discharge process.

In **Fig.1.4** the major components of Li- ion battery are shown in terms of cost breakdown [6].

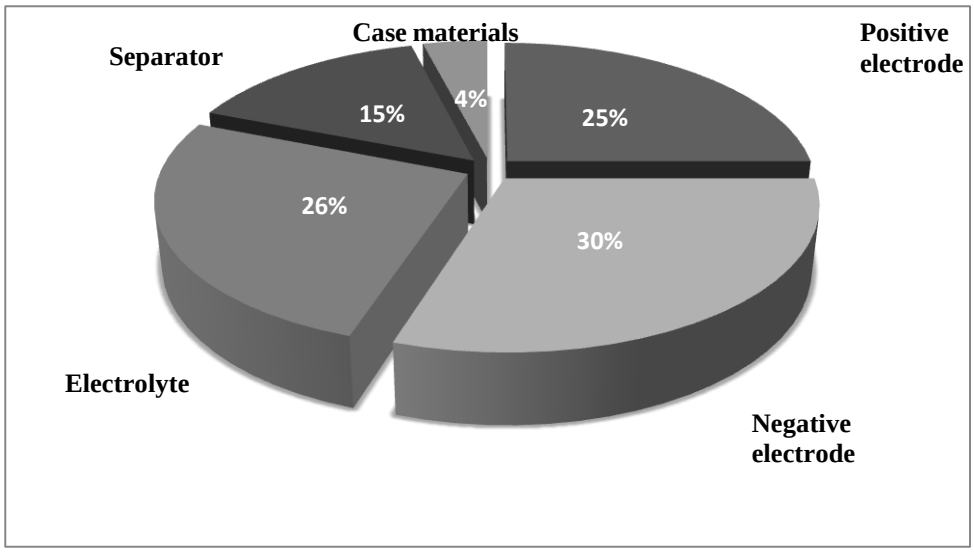

Figure 1.4 LiBs major components.

Typical cathode material (**Table 1.2**) is layered metal oxides with a general formula of $LiMeO_2$ (Me = Transition metal elements such as Co, Ni and Mn), in which the Li ion and Me-ion occupy the alternate planes of the rock salt structure.

Table 1.2 Main characteristics of commonly used positive electrode active material for LiBs *(Source* [29], [30]*).*

Material	**Q_{max} (mA h $g^{-1)}$**	**Midpoint $E_{eq}/(Li/Li^+)$/ (V)**	**Advantages or disadvantages**
Layered compounds			
LiCoO2	274	3.88	Most common, Co is expensive
$LiNi_{0.7}Co_{0.3}O_2$	190	3.7	Intermediate cost
$LiNiO_2$	274	3.55	Most exothermic decomposition
Spinels and olivines			
$Li_2Mn_2O_4$	213	4.00	Mn is inexpensive, low toxicity
$LiFePO_4$	170	3.4	Fe is inexpensive, low toxicity

Table 1.3 Main characteristics of negative electrode active materials for LiBs (*Source* [30]–[32]).

Material	**E_{eq}/(Li/Li^+)/ (V)**	**Q_{max} (mA h $g^{-1)}$**
Li	0	3861
LiC_6	0.1	372
$Li_{1/2}C_6$	0.13	186
LiAl	0.35	993
$Li_{22}Sn_5$	0.42	994
$Li_{21}Si_5$	0.3	4000
Li_XTiO_2	1.8	170

Most commercial LiBs are based on anodes with carbonaceous materials, but with regards to low gravimetric and volumetric capacities research is turning to lithium metal alloys as the most promising materials to replace current carbon based anodes.

As an example, Sony successfully implemented SnCo anode in their Nexelion battery, which has 50 % increase in volumetric capacity over conventional battery [33].

There are 4 types of electrolytes that have been used in Li ion batteries: liquid organics and ionic non aqueous, gel and organic/inorganic solid electrolyte.

The most popular electrolytes are the liquid-type ones where carbonates or esters of simple alcohol and glycol are frequently used as solvents which contain $LiPF_6$ as an electrolyte. Solvents are mixed in a solution of ethylene carbonate (EC) of high dielectric constant and methyl ethyl carbonate (MEC) of low viscosity. Sometimes a combination of γ-butyl-lactone and $LiBF_4$ is utilized. Propylene carbonates are excellent solvents, but they decompose vigorously on the surface of graphite. Currently research is looking to replace organic based electrolyte due to the flammability of the solvents [34], [35]. However, it is difficult to achieve the same Li ion conduction as in conventional organic electrolytes. Another main aspect that has to be considered in LiB is solid electrolyte interphase (SEI) which is a protective passivation film formed on negative electrode surfaces during the first charge or discharge cycle; it creates a barrier and thus reduces the transfer of electrons, solvent molecules and salt anions.

The separator used in LiBs has two important functions: one is to avoid the direct contact between the anode and cathode, while it allows a free mass transfer of the electrolyte, and the other is a shutter action to stop the mass transfer in the case of accidental heat generation. The material should be soft and flexible enough to act as buffer between the both sheets of cathode and anode and should be sufficiently stable for a long time while it is kept in contact with the electrolyte: orientated polyolefin film is commonly used.

1.5 Lithium ion battery cell diagnosis and testing

LiB have been extensively diagnosed and characterised to understand chemical, structural and morphological changes that lead to degradation, [36] and failure as they are aged, cycled or abused [37].

Both *in-situ* and *ex-situ* characterization have been carried out to study SEI formation and composition and the aging phenomenon in LiB, such as atomic force microscopy (AFM) [38], scanning electron microscopy (SEM) [39]–[41], transmission electron microscopy (TEM) [42], Raman spectroscopy and other X-ray [39], [43]–[46] and neutron techniques [47], [48] [30]. These studies were coupled with electrochemical cycling to study structural changes in complex and to understand the dynamic evolution of morphology during cycling. While the *ex-situ* studies have significantly broadened understanding of the LiB reaction mechanism; they can misguide interpretation and lead to the errors due to the sample post treatment and exposure to the air, i.e. during the washing away the electrolyte for the XRD studies some important crystals could be dissolved. In this light in-situ studies are crucial in obtaining the unambiguous information as this allows a real time investigation.

An *in-situ* electrochemical impedance approach [49] was used to measure the resistance for lithium ion permeation in SEI layer during cell cycling, thus electrochemical impedance was measured simultaneously with charge-discharge of the battery.

It can be seen that the current LiB technology fulfills the requirements of cycle life, power density and specific power and significant improvements have been made in the past decade. LiB technology leads the electronic consumer market and has been successfully implemented on larger scale in electric vehicles. However, further improvements in energy density, specific energy, calendar life, operating temperature range and further reduction of cost are required to satisfy requirements for EV market; also LiBs are subject to aging even if they are not in use, the operating temperature range and the thermal management of battery packs is still an issue.

In this light research is turning to new chemistries such as Li/S and Li/air batteries which are considered as the next generation batteries, having theoretical energy density 3-5 times higher than of conventional intercalation electrodes. [50]

1.6 Research objectives and thesis structure

Theoretically, the Li/S battery has the ability to outperform conventional lithium ion batteries and there are significant technological advancements in recent years and ongoing improvements on the chemical composition of the cell; however there are certain limitations, such as low cycle life, capacity degradation, and swelling that need to be addressed.

The objective of this work is therefore to gain a better understanding of the Li/S system; identify and develop electrode materials/electrolytes for Li/S batteries targeting performance enhancements required for practical implementation of high energy lithium/sulphur batteries, and thus the focus is on the:

a) development of a suitable sulphur electrode composite with enhanced conductivity;

b) fitting between optimised sulphur electrode and electrolytes.

In chapter 2, a general background on Li–S batteries and an overview of the most relevant research is provided. The description of the experimental work, as well as the results and discussion are presented in chapters 3-6.

Chapter 3 begins with the investigations into the preparation of the positive electrode and the influence of the fabrication steps on the cycling performance of the battery. The working principles of the characterization techniques used in this work are also described here.

The data obtained in chapter 3 were used for the positive electrode optimisation and subsequent investigations on the effect of the cathode composition and morphology on the battery performance. These data are presented in chapter 4 which concerns the development of positive electrodes by using high surface area mesoporous carbon materials and conducting polymers (S/C/Polyaniline), also the effect of metal oxide additives on the electrochemical performance of Li/S cell (S/C/Polyaniline with $Mg_{0.6}Ni_{0.4}O$ and Al_2O_3) is presented.

Since many issues arise due to polysulphides solubility, the design of an optimized Li/S cell requires adjustment between electrodes and electrolyte composition. The influence of both adsorbents and electrolyte content modifications with S cathodes developed in this work is shown in chapter 5. Furthermore, using electrochemical impedance spectroscopy (EIS), physical and chemical processes can be monitored during cycling of the battery and the impedance contribution can be determined.

In chapter 6 the development and application *in-situ* X-ray tomography of the Lithium Sulphur cell is presented for a better understanding of the Sulphur electrochemical reduction. This method allows us to track the morphology evolution upon cycling and correlate this information with electrochemical characterization data.

Finally, the summary of the thesis with the conclusions and future work recommendations are given in chapter 7.

CHAPTER II. Background & Literature Review

This Chapter introduces the background and the general operation of Li/S battery including its advantages and challenges that need to be overcome. Additionally, a literature review describes the current state of Li/S battery technology research and development and summarizes recent efforts in its optimisation by the development of new materials and concepts for electrodes and electrolytes and their subsequent characterisation.

2.1 Background

The Lithium/Sulphur (Li/S) battery system is one of the most promising next generation batteries due to their ten times higher energy density compared with LiBs [11], [8], [51], [52] and high theoretical capacity of sulphur 1675 mA h g^{-1}. Additionally Li/S system can provide environmental friendliness and low cost due to abundance and non-toxicity of elemental sulphur. Moreover, the Li–S battery can be operated over a wide temperature range, especially at low temperature [53], which is essential for the demands of power sources in cold environments, such as battery systems for electric vehicles, as well as some aeronautical applications.

2.2 Operating principles

The concept of elemental sulphur as a positive electrode material was first introduced by Helbert and Ulam in 1962 and the first demonstration of a Li/S battery was presented in the late 1960s [54]–[56].

In Li/S cell the overall redox couple described by the following reaction [57]:

$$S_8(s) + 16\ Li \rightleftarrows 8\ Li_2S(s); \quad \textbf{(2.1)}$$

$$\text{Reduction: } S_8(s) + 16\ e^- \rightarrow 8S^{2-} \quad \textbf{(2.2)}$$

$$\text{Oxidation: } Li \rightarrow Li^+ + e^- \quad \textbf{(2.3)}$$

The potential lies at an average voltage of 2.15 V with respect to Li^+/Li^0 .

In the earliest configuration, the Li/S cell consisted of an elemental sulphur electrode with non-electrochemically active additives conductors such as carbon and binders, separated from a lithium metal negative electrode by an organic electrolyte (a lithium salt in carbonate organic solvents) as shown in **Fig. 2.1**. This configuration has been a base for subsequent research. An electronic conductor is used to improve the electronic conductivity of the electrode, while a binder is added to ensure the cohesion between the materials. It is also important to note that conductive additives and binder must be added in a minimal quantity, and thus do not significantly decrease the gravimetric energy density of the battery.

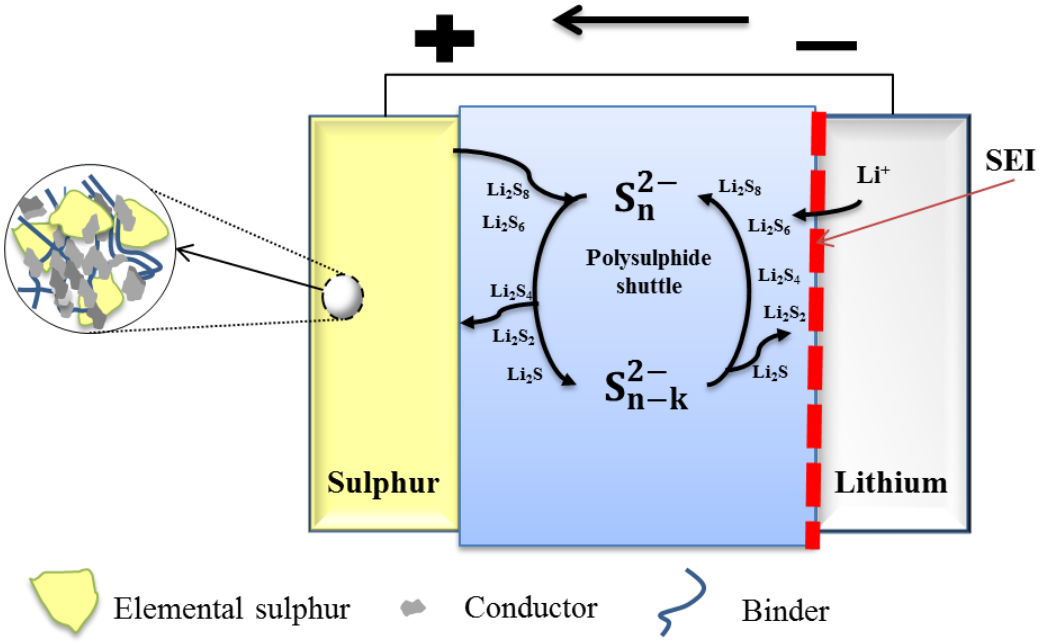

Figure 2.1 Li/S cell schematic representation

The reduction of sulphur by lithium in an organic electrolyte is a complex, multistep electrochemical process and involves different lithium polysulfide intermediates (Li_2S_8, Li_2S_6, Li_2S_4, Li_2S_2) and a final product of Li_2S [52], [58], [59]. This explains the multistage discharge characteristics of Li/S battery. Despite intensive research of the Li/S system its discharge mechanism is still not well defined and there are different theories on the S reduction mechanism [8], [10], [60], which are not in the agreement on intermediate products and steps.

The discharge process is believed to occur through three main steps (I) conversion of solid sulphur to soluble polysulphides; (II) shortening of the polysulphides chain length and their conversion to solid Li_2S_2; (III) conversion of solid Li_2S_2 to solid Li_2S. This usually results in two plateaus when discharging at room temperature as seen in **Fig. 2.2**. The first plateau is shorter as the longer chain polysulphides that mostly form in the initial discharge region are relatively unstable and can readily dissociate into lower order polysulphides. The second plateau is longer and defines the kinetics of the system. The concentration of the S_8 and the higher order polysulphides decrease as they are further reduced to the lower order polysulphides. This process has a slower rate as the chemical activity is reduced as well.

The final discharge products are highly insoluble in the electrolyte and they start to precipitate forming a passivation layer. At the end of discharge the passivation layer is built up and no further sulphide ions reduction is possible.

When recharging the cell, the opposite process takes place, where Li_2S is oxidized successively to soluble polysulphides and finally to solid sulphur. As the redox reaction is accompanied by phase change of active material (solid–liquid phases), structural and morphological changes occur at the positive electrode.

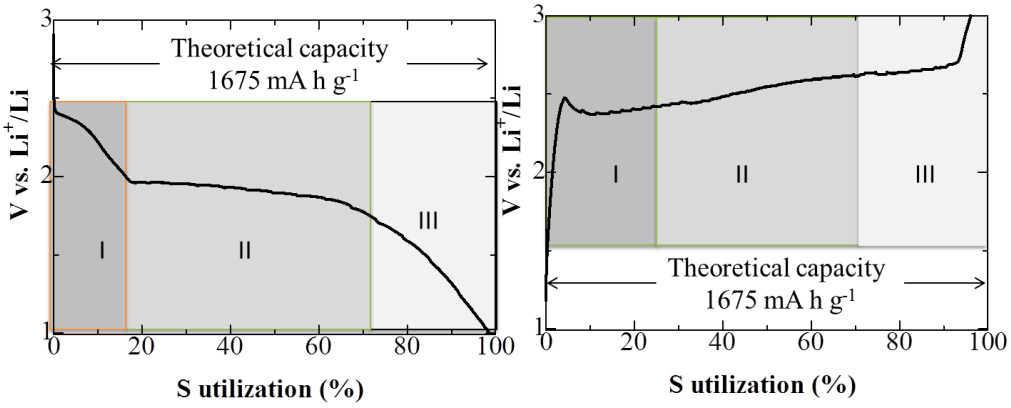

Figure 2.2 Typical discharge-charge profile of Li/S battery in organic electrolyte. illustrating regions (I) conversion of solid sulphur to soluble polysulphides; (II) conversion of polysulphides to solid Li_2S_2; (III) conversion of solid Li_2S_2 to solid Li_2S [8]

The enthalpy of formation of Li_2S, ΔH_f^0 (at 298 K) is – 445.59 kJ mol^{-1}. The specific capacity of sulphur is calculated in equation (2.4):

$$\text{Specific capacity} = \frac{n_e \cdot F}{M_S}(A \cdot s \cdot g^{-1}) = \frac{1000 \cdot n_e \cdot F}{3600 \cdot M_S}(A \cdot h \cdot kg^{-1}) =$$

$$= 1675\ A \cdot h \cdot kg^{-1} \quad \textbf{(2.4)}$$

where:

n_e - the number of electrons per atom of sulphur (2);

F - the Faraday constant (96485 C);

M_s - the molar mass of sulphur (32 g mol^{-1}).

Based on the discharge profile, the average discharge potential (E) is at around 2.15 V vs. Li^+ /Li (2.5) and the specific energy can be calculated as follows:

$$\text{Energy density} = E \cdot \frac{n_e \cdot F}{M_S}(A \cdot s \cdot g^{-1}) = E \cdot \frac{1000 \cdot n_e \cdot F}{3600 \cdot M_{Li_2S}}(W \cdot h \cdot kg^{-1}) =$$

$$= 2505\ W \cdot h \cdot kg^{-1} \quad \textbf{(2.5)}$$

Although here we present a typical 2 stage Li/S discharge curve, it is noted that the discharge mechanism could be very different in various electrolytes as it dictates the species equilibrium.

It is critical to understand the detailed mechanism of S reduction that will help to optimize the cathode. Unlike LiBs where the insertion mechanism is governing and each plateau is connected to a phase transition, in Li/S system the governing mechanisms are dissolution/precipitation reactions, thus it is difficult to predict the evolution of the discharge potential. Lithium polysulphides are soluble in the electrolyte and are not air stable, they react quickly with moisture and oxygen, the sulphur cathode itself is not stable and can self-discharge. These make conventional characterisation methods difficult to use to understand the Li/S battery mechanism.

2.3 System limitations and challenges

Despite the intensive attention of electrochemistry community for many years this system has not been commercialized yet. There are certain issues [17]–[19] that have to be overcome, mainly Li/S batteries suffer from rapid capacity fading; also the practical capacity and cycle life of Li/S cells are usually lower than expected. This comes from:

- **Insulating nature of sulphur and Li_2S;**

S is an insulator with a very high electrical resistivity of 1×10^{15} m Ω at 20 °C. The end discharge product, Li_2S, is highly insulating as well. This causes low active material utilization and thus low practical output capacities. To overcome this issue, conducting agents need to be added and well mixed with S in order to have smooth electron transport between conductor and active material interfaces.

- **Dissolution of lithium polysulfide intermediates that occur during battery charge and discharge;**

In Li/S cell the dissolution of the intermediate products in the liquid electrolyte is inevitable; lithium polysulphides dissolve in the liquid electrolyte during charge and

discharge. Although the polysulfide dissolution assists the utilization of active materials, as the dissolved polysulphides (Li_2S_n, $2<n<8$) can migrate freely to ensure intimate contact with conductive additives, the dissolution behaviour also brings numerous disadvantages, such as self-discharge, shuttle effect and Li_2S deposition on the surface of both electrodes.

- **Large volume change during intercalation processes by 79.2 % due to reduction from elemental sulphur to Li_2S** [64]**;**

There is a density difference between Sulphur (2.03 g cm^{-3}) and Li_2S (1.66 g cm^{-3}). The volume expansion of the electrode can lead to the crack formation and thus the failure of battery. To buffer the volume change flexible materials or 3 dimensional current collectors can be used in the cathode. This will be discussed further in the following subsection.

- **Use of Li metal electrode;**

Li metal anode brings dendrite formation problem leading to low coulombic efficiency and safety issues. There are different approaches could be found in the literature, such as protection of the lithium electrode with a layer or replacing it by lithiated electrode (lithiated graphite or lithiated metal alloys). This will be discussed further in the subsection 2.6.

- **Shuttle effect.**

The parasitic reactions happening on the surface of the anode leads to a so-called “shuttle mechanism”. High-order soluble polysulphides diffuse through the separator to the anode, where they are reduced to insoluble Li_2S or Li_2S_2; and the reaction between this high order polysulphides and the insoluble products form the lower order polysulphides. They diffuse back to the cathode and are re-oxidised to the high order polysulphides. These reactions lead to the low coloumbic efficiency and low utilization of active material and rapid decrease in the cell cyclability.

- **Self-discharge,**

Self-discharge is also results from the active material dissolution. As the cell storage time increases, active sulphur in the cathode structure reacts with the lithium ions in

the electrolyte and, therefore, produces soluble lithium polysulphides, which could gradually diffuse out of the cathode.

Most of the above mentioned issues arise due to the high solubility of intermediates that leads to a parasitic reaction on the metallic-lithium anode and accompanied by "sulphur shuttle mechanism". This phenomenon decreases the active mass utilization in the discharge process and reduces the coulombic efficiency in the charge process [20]. Moreover, lithium polysulfide intermediates can spontaneously diffuse in the separator, leading to cell self-discharge and increased electrolyte viscosity.

The listed issues are not new and have been intensively studied. There are different approaches that have been employed, mostly either on the positive electrode morphology or on the organic electrolyte composition. However, for the successful implementation all components of the cell must be addressed as a whole.

Most recent studies on cathode optimisation have aimed to find the best configuration to trap sulphur and lithium polysulphides by applying mesoporous or nanostructured carbon materials [62]–[66], thus preventing sulphur material diffusion through the electrolyte, and improving discharge capacity and cycle life. The use of mesoporous carbon materials prevents diffusion of the sulphur compounds through the electrolyte and improves cell cycle life. In some studies a cathode composite is also coated using conducting polymers such as polypyrrole [67]–[71], polyacrylonitrile [72]–[74] or polyaniline [75]–[77]. Sun *et al*. [67] report that conducting polymers can improve cathode electronic conductivity and also present other advantages, i.e. polypropylene can act as an agent favouring homogeneous sulphur distribution within the composite. Further details will be described subsequently. As for the electrolyte there are numerous publications [78]–[80] on the optimisation of organic liquid electrolyte composition with an aim to find a solvent in which polysulphides are less soluble [17], [81]–[83] and studies on solid and polymer electrolyte [84]–[86] (see 2.5). There are also a few studies [87]–[89] on a cell without metallic lithium as anode, instead it is proposed to use alloy anodes or lithiated graphite (see 2.6).

2.4 Sulphur Cathode

2.4.1 Basic Sulphur properties

Sulphur is a widely available element and has over 30 solid allotropes. The most common form is cyclic octasulphur (S_8), followed by the cyclic S_{12} allotrope [59], [90], [91]. There are three octasulphur forms: α-sulphur, β-sulphur, and γ-sulphur, of which the β-sulphur and γ-sulphur are metastable and convert to α -sulphur in storage at ambient temperature.

The α-sulphur melts at 115.21 °C, boils at 444.6 °C, and sublimes easily. Sulphur exhibits a unique viscosity and temperature behaviour in the molten state. On heating, the viscosity of the sulphur melt slowly decreases, followed by a remarkable increase around 160 °C as a result of the opening and polymerization of the S_8 rings until near 190 °C at which sulphur starts depolymerising and the viscosity decreases. Therefore, there is a minimum viscosity value near 160 °C. This feature has been widely adopted to impregnate sulphur into porous materials for the preparation of sulphur composite materials. Allotropes with rings of 9-5, 18 and 20 sulphur atoms are formed above 160 °C, and quenching of this melt forms amorphous sulphur, which is elastic and metastable. Upon storage, the amorphous sulphur reverts to a crystalline allotrope. The allotropes with 2-5 sulphur atoms are only present in vapour above 720 °C or slightly lower temperatures under lower pressure. These small molecular sulphur allotropes revert to the solid allotrope (S_8) once the temperature cools down. Sulphur is slightly soluble in many polar electrolyte solvents. Unlike elemental sulphur, small polysulphide anions can be formed readily and stably in solution.

2.4.2 Carbon materials

Carbon materials have been widely used in Li/S battery starting from bulk carbon in the structure of macro composite electrodes to mesoporous carbons employed more recently [8]. Improving the specific surface area of the cathode enables precipitation of polysulfide compounds on the electrode, thus delaying the full passivation of the sulphur electrode and the end of discharge [62], [64].

There are different carbon materials have been employed and these have been summarized in the **Table 2.1**:

Table 2.1 Carbon materials used in Li/S battery structure

Characteristics	**Super P**	**Ketjen black©**	**Carbon active**	**Carbon fiber**	**Carbon nanotubes**	**Graphene**
BET, m^2g^{-1}	60	800-1600	1900	13	-	640
Particle size, nm	≈ 40	≈ 30	≈8000-15000	Diameter 150, Length, more than 10 000	Diameter 150, Length, More than 1000	5.2
References	[92]	[93]	[94] [95]	[96]	[97]	[98]

Carbon black is the most common additive in sulphur electrodes: such carbon materials as ketjenblack or activated carbon are used due to their high specific surface which enables homogeneous distribution and fine particles in the electrode [99], [100]. Wu *et al*. [101] reported a capacity of 1200 mA h g^{-1} after the first discharge, as well as good cycling behaviour with a reversible capacity of 750 mA h g^{-1} after 60 cycles (100 mA g^{-1}, with 49% S in the electrode).

Carbon nanotubes and carbon fibres have long been investigated as a conductive form of carbon that might provide an encapsulation effect. According to Yuan *et al*. [102] adding carbon nanotubes allowed a battery to reach a capacity of 900 mA h g^{-1} and ca. of 75 % capacity retention after 60 cycles.

Recently graphene was tested in a structure of Li/S battery [66], [72], [103]–[105]. Two different approaches have been employed to combine sulphur and graphene: envelop large sulphur particles by graphene sheets or sandwiching sulphur particles between functionalized graphene sheets using Nafion coating.

2.4.3 Conductive polymers additives

Conducting polymers have gained extensive attention as a host or coating media for S cathodes due to their good environmental stability and electrical conductivity as well as their useful mechanical and electronic properties, so along with the increase of conductivity polymers can also encapsulate S in their matrix as carbon materials. Unlike carbon nanostructures, where fabrication processes require temperatures up to 600 ºC [64], [102], polymers can form different structures at much lower temperatures up to 100 ºC; also their unique chain structure gives possibility of further chemical confining of S and its products. Another advantage of polymers is their mechanical softness and self-healing, that can help to address an issue of S cathode volume change during charge-discharge [106]–[108].

Thus conductive polymers such as polyacrylonitrile (PAN) [72]–[74], polypyrrole (PPy) [67], [68], [70], [71], [109], polythiophene [110] and recently polyaniline [75]–[77], [111] have been tested in Li/S batteries. It was shown that adding conducting polymer improves composite conductivity along with improved homogeneity of sulphur distribution in composite and thus can enhance the electrochemical performance of the cell.

There are various approaches that can be used to make S – polymer composite. This includes: a) coating by mixing conductive polymer and sublimed sulphur with further heat treatment, thus letting organo -sulphur bonds to be formed; b) mimicking the structure of carbon nanotubes; c) *in-situ* deposition of sulphur with conductive polymer.

In [70] S/PPy composite was prepared by ball milling without heat treatment, that allowed to avoid sulphur loss and it has been reported a high discharge capacity at ca. 600 mA h g^{-1} after 20 cycles and 500 mA h g^{-1} after 40 cycles. Wang *et al*. [74] reported a battery with PAN/S composite as cathode material that exhibited a specific capacity of ca. 850 mA h g^{-1} at the initial cycle and after 50 cycles remained ca. 600 mA h g^{-1}. Another conducting polymer, polyaniline, has also been used as a coating agent by an *in-situ* chemical- oxidative-polymerization method and by simple ball milling. The performance of Li/S battery with various conductive polymers has

been summarized in **Table 2.2.** Based on the review PAN and PANI are promising conductors in S cathode. S composites based on them are giving the highest energy density compared to the composites based on other conductive polymers, therefore in this work PAN and PANI were used as a conductor along with the high surface area carbon material, details are in chapters 3 and 4.

Table 2.2 Summary of the performance of Li/S battery systems with different conductive polymers

Conductive Polymer	Approach	First discharge capacity (mA h g^{-1})	Reversible discharge capacity (mA h g^{-1})	Current rate	Total cycle number	Sulphur loading in electrode	Ref.
Polypropylene (PPy)	core-shell structured S-PPy composites	900	672	335 mA g^{-1} (C/5)	50	65.8 wt %	[69]
	a simple one-step ball milling without heat-treatment	1320	500	100 mA g^{-1}	40	65 wt%	[70]
	in-situ deposition of sulphur with polypyrrole pre-synthesized by an oxidation method	1010	400	837.5 mA g^{-1} (C/2)	50	53 wt %	[109]
	the sublimed sulphur is incorporated with a tubular polypyrrole (T-PPy) fiber	1151.7	650	0.1 mA cm^{-2}	80	30 wt %	[71]
Polythiophene	*in-situ* chemical oxidative polymerization method	1120	≈ 806	100	80	72	[110]
Polyacrolonitrile (PAN)	mechanical mixing, the S/PAN with sulphur in carbonate based electrolyte	1403.6	700	0.25 mA cm^{-2}	80	42 wt %	[74]
	ball milling with heat-treatment a) ternary S/PAN/$Mg_{0.6}Ni_{0.4}O$ and b) binary S/PAN	a)1545 b)1000	a) 1223; b) ≈ 400	167.5 mA g^{-1} (C/10)	100	a)38.5 wt %; b) -	[73]
Polyaniline (PANI)	ball milling with heat-treatment S/PANI/Carbon composite	1150	732	335 mA g^{-1} (C/5)	100	-	[75]
	PANI Nanotubes via an *in-situ* vulcanization	755	837	167.5 mA g^{-1} (C/10)	100	-	[76]
	PANI layer was covered onto the surface of the S/C composites by an *in-situ* chemical-oxidative-polymerization method	635.5	≈ 380	16750 mA g^{-1} (10 C)	200	43.7 wt%	[111]

2.4.4 Metal oxide additives

Metal oxide additives to S cathode such as $Mg_{0.6}Ni_{0.4}O$ [73], [112], Al_2O_3 [113]–[116], V_2O_5 [117] have been employed to adsorb lithium polysulphides.

In most of these studies, the S – metal oxide composite was prepared by thermo-treating and ball milling: in [115] a liquid phase methodology for the S- Al_2O_3 composite was employed. The authors claim that it allows homogenous mixing of Al_2O_3 within the electrode structure. In this study it has been demonstrated that Al_2O_3 can effectively trap polysulphides and enhance the electrochemical performance of the Li/S cell, so the initial discharge capacity of the cathode with the added alumina was 1171 mA h g^{-1}, and the retained capacity was 585 mA h g^{-1} after 50 cycles at 0.25 mA cm^{-2}.

Song *et al*.[112] introduced the use of $Mg_{0.6}Ni_{0.4}O$ prepared by sol-gel method and demonstrated that this additive can improve the electrochemical performance and achieve the initial capacity of 1185 mA h g^{-1} at a constant current 167.5 mA h g^{-1} (0.1 C) by adding 12 wt.% of it to the active material. Zhang *et al*. [50], [73] have optimised this approach by simplifying the preparation method and minimising the amount of $Mg_{0.6}Ni_{0.4}O$ added to 4 wt. % and investigated its effect conventional S cathode and on S/Polyacrylonitrile (PAN) composite cathode. The initial capacity for S cathode and on S/PAN composite cathode was 850 mA h g^{-1} and 1223 mA h g^{-1} at constant current 167.5 mA h g^{-1} (0.1 C) respectively.

2.4.5 Binders

The most commonly used binder in Li/S cell is poly-vinylidene fluoride (PVdF) in a solution of N-methyl-2-pyrrolidone (NMP). This polymer is a chemically stable organic electrolyte, which allows the electrode to maintain its morphology and accommodate mechanical stress. In some papers [58], [118], [119] poly (ethylene oxide) (PEO) is used in acetonitrile or isopropanol, as well as polytetrafluoroethylene (PTFE) in ethanol or water [52], [99]. Some authors also report the preparation of

positive electrodes in aqueous phase, where they used carboxymethylcellulose (CMC) or gelatine [120], [121].

2.4.6 Current collectors

In most studies aluminium foil was used as a current collector of sulphur cathode [122]. However, Al metal can react with sulphur at certain conditions [123]. It is suggested to carbon coat Al foil to avoid direct contact with sulphur, so current collectors can be made of metal-coated polymer layers, such as polyamide [124].

There are few publications where porous current collectors for sulphur cathode were used [70], [73], [82], [125]. Barchasz *et al*. [19] tested various current collectors Ni foam, C foam, non-woven carbon (NWC) and vertically aligned carbon nanotubes (VACN) to investigate how they influence on battery performance and made a conclusion that NWC current collector provided stable morphology during cycling, carbon foam increased significantly increased discharge capacity up to 1400 mA h g^{-1}. Another aspect that has to be considered when choosing the current collector is its compatibility with electrolyte.

Therefore porous current collectors proved to be the best option for Li/S batteries, and can also be optimised in terms of their porosity and the thickness. Current collector characteristics have to be carefully considered in Li/S system and this can help to increase cell discharge capacity along with gravimetric energy density.

2.5 Electrolyte

In the literature, different approaches have been employed to optimise Li/S cell electrochemical performance, including the optimisation of the electrolyte. Li/S cell electrochemical performance is known to be highly dependent on the electrolyte, [81], [123], [126], [127]. It acts not only as ionic conductor, but also dictates the solubility of electroactive components: S and lithium polysulphides. Lithium polysulphides are highly reactive and it is known that they react with most of the common electrolyte solvents, such as esters, carbonates and phosphates [45].

As described in 2.2, the electrochemical reduction of sulphur in lithium–sulphur cells occurs through the formation of intermediate lithium polysulphides with a general formula Li_2S_n ($2<n<8$) followed by the final reduction product to Li_2S. During discharge, it is assumed that the elemental sulphur in the solid phase $S_8(s)$ is firstly dissolved in the electrolyte as S_8 (solvated), which is then gradually reduced to lithium polysulphide. Intermediate products of high order lithium polysulphides (Li_2S_n, $4 < n < 8$) are soluble in most of the commonly used organic solvents, but the lower order lithium sulphides Li_2S_2 and Li_2S are insoluble. However, the detailed sum of stable polysulphide intermediates during the discharge of a Li/S cell has not yet been identified beyond doubt. Also it was found that the discharge behaviour is different in various electrolytes [81], such as OCV values are different and the plateaus length and voltage are also electrolyte dependent.

The most common electrolytes in conventional Li-ion batteries are liquid ones that consist of solutions of lithium salt in organic solvents, i.e. lithium hexafluorophosphate ($LiPF_6$) dissolved in a mixture of carbonate solvents such as ethylene carbonate (EC), propylene carbonate (PC) and dimethyl carbonate (DMC) [128]. However, this type of liquid organic electrolyte is not commonly used in batteries Li/S, as it was suggested that carbonates are not chemically stable against polysulphide intermediates [83]. State-of-the art electrolytes for Li/S batteries are mostly based on ethers as they are chemically stable against highly nucleophilic polysulphides and stable against the lithium metal anode. Another advantage of ether based electrolytes is their polysulphide solvation ability. Further details on electrolyte composition and its optimisation could be found in chapter 5.

2.5.1 Ether based liquid electrolytes

There are several studies where different electrolyte, ether and carbonate solvents were compared in different combinations and volume ratios. Gao *et al*. [45] has compared seven different organic electrolytes with ether and carbonate solvents and studied their effects on lithium sulphur cell performance electrochemically and by X-ray absorption spectroscopy studies. This study revealed that products of sulphur in

1,3-dioxolane (DOL)/ dimethoxyethane (DME) and tetra(ethylene glycol) dimethyl ether (TEGDME) are similar and are promising solvents for the Li/S batteries. It also revealed that carbonate solvents undergo a variety of reactions with reduced S species.

With the dissolution of polysulphides, the viscosity of the system increases, the solvents used in Li/S cell should have low viscosity and demonstrate high polysulphide solubility, as well as high ionic conductivity. DME due to its low viscosity and high polysulphide solubility is one of the most common solvents used in Li/S cells, however it is more reactive with Li compared to DOL or TEGDME. TEGDME has higher ionic conductivity but is more viscous compared to other ethers. Thus in most of Li/S cells with liquid electrolyte a combination of DOL, DME, TEGDME in different ratios are used. [78], [123], [81], [129].

One of the issues that have to be overcome for liquid electrolytes is that all solvents are gradually depleted with cycling of the cell which results in the cell performance fading and swelling.

Lithium salts used in electrolyte also should be chemically stable with polysulphides. The reason why conventional lithium salts used in Li-ion battery technology are not compatible with S cathode is reactivity with Li polysulphides [123].

There are few comparative studies on the effect of lithium salts in the electrolyte. In the literature LiTFSI salt is commonly used, as it is exhibited better electrochemical performance according to several studies [81]. Lithium perchlorate has been used by some groups [130], [131], but the performance was inferior, presumably due to inability to form a stable SEI layer on metallic lithium anode.

2.5.2 Electrolyte Additives

Some additives can also be added to the electrolyte composition in order to improve battery performance: Choi *et al.* [79] reported that toluene can help to decrease the electrolyte viscosity, thus providing higher ionic conductivity to the system, and possibly decrease the intermediate products dissolution. A recent study from Zhang[132] reveals that introducing a quaternary ammonium, either a solid salt or an

ionic liquid, into the liquid electrolyte can effectively decrease the passivation of polysulphide intermediates, which increases the Li/S cell's capacity retention, but is unable to mitigate with the redox shuttle.

Lithium nitrate ($LiNO_3$) as an additive to electrolyte is effective in suppressing the redox shuttle and is one of the most promising additives, it has been introduced by Mikhaylik [80] who first disclosed that the "redox shuttle" of polysulphides could be effectively suppressed by employing lithium nitrate and allows close to 100% coulombic efficiency.

2.5.3 Alternative electrolyte configurations

The effects of varying the amount of electrolyte and salt concentration are also factors to influence the battery performance. There are few studies on these parameters in the literature [133]. More recently the idea of pushing salt concentration to solvent solubility has been presented by Suo *et al.* [134] in the so-called "solvent-in-salt" principle. Their results showed remarkable stability and cyclability of the cell. Together with Shin *et al* [135] works these solutions are promising grounds for further studies.

Gel polymer and solid state electrolytes are also potential candidates for the electrolyte in Li/S cells. Soluble polysulphides do not migrate extensively in the high-viscosity gel and solid-state electrolytes, which could decrease the loss of active material and restrain the shuttle effect. Various glass ceramics are used as the solid-state electrolytes, such as Li_2S-P_2S_5 and Li_2S-GeS_2-P_2S_5 glass compounds. These electrolytes make all-solid-state Li/S battery possible, but lower ionic conductivity might sacrifice the rate capability of the cell.

Another approach is the use of polymer electrolytes, such as polyethylene oxides [136]. The solid electrolytes delay the lithium polysulphides dissolution; however it is difficult to achieve the ionic conductivity of ether-based electrolytes.

2.6 Anode

As mentioned above, the negative electrode of conventional rechargeable Li /S is composed of a lithium metal foil. However, due to its high reactivity with organic electrolytes, and its property to form dendrites, different research groups are trying to develop ways to protect the lithium electrode. Li-ion conductor Li_3N [137], [138] and LiPON [139] have been coated on the surface of the lithium foil. Lee [140] introduced a protective film on the surface of the Li by UV cured polymerization for the lithium sulphur battery. This film was acted as a guarantee to protect the lithium from the corrosion by the soluble polysulphides. However, the fabrication procedure is complicated and costly.

An alternative to the metal lithium foil is the use of a lithiated negative electrode, such as LiAl alloy type LiGe, LiSi, described by Kobayashi *et al*., Huang *et al*., or Machida *et al*.[141]–[143]. The use of these alloys as negative electrode materials is an avenue to remove the dendrite formation during charging. The operating potential of these negative electrodes is slightly higher than 0 V, between 0.1 and 0.7 V vs. Li^+ / Li, but the energy loss is largely offset by the gain in battery safety. Other research groups propose the use of graphite lithium [144]–[146]. However there is a disadvantage of this method since it is complicated to implement for mass production and has low industrial feasibility. Finally, an alternative to lithium metal is the use of a negative electrode of tin (Sn) or silicon (Si), in combination with a positive electrode of Li, this alternative allows the production of Li-ion/S, and is described by Cui *et al*. and Scrosati *et al*. [87], [88], [147], however there is a drawback of the this system as Si/Li_2S cells cannot withstand over-discharge [123].

2.7 Selected research on Li/S battery diagnostics and testing

The Li/S battery is a complicated system due to the multistep process happening during discharge and charge: the precise reaction mechanism still is a subject of debate and may not even be the same for different electrolytes. Moreover the nature of sulphur and intermediates adds some limitations to conventional characterization techniques, such as low melting point, high vapour pressure, polysulphides instability

in air, all these add difficulties in obtaining information on the morphological, structural and compositional structure of the sulphur cathode. In this subsection an overview of the main characterization techniques applied for Li/S battery is given, details on the techniques used in this work and its basic principles could be found in chapter 3.

Sulphur cathode characterization methods employed in most of publications include following techniques: scanning electron microscopy (SEM) [119], [148] transmission electron microscopy (TEM) [113], Raman spectroscopy [68], [149], atomic force microscopy (AFM) [149], X-ray Diffraction (XRD) [79], [148], X-ray Absorption Spectroscopy (XAS) [45] and X-ray imaging [150], [151].

Ex-situ studies have been significantly employed in Li/S battery characterisation and helped to broaden understanding of its chemistry and processes, however they bring many controversies related to some details of S cathode, such as S reduction mechanism and S_8 formation at the end of charge, i.e. S_8 was observed in some cases [152], [153] whereas other studies claimed that soluble polysulphides never transform back to solid S_8 [119], [154]. These results are from XRD, SEM, TEM studies, where pre-treatment processes involved and electrolyte has to be washed out with a possibility that some sulphur is removed. Therefore, *in-situ* and *in-operando* methods can give more accurate analysis.

In-situ studies using AFM, TEM, Raman and UV-vis spectroscopy, XRD, X-ray computerised tomography (X-ray CT) etc.were already developed and performed successfully on lithium-ion batteries, for example in [38], [46], [49], [155]–[157]. So far, however, there has been limited application of these techniques in Li/S batteries, partly due to the S cathode specifics aforementioned techniques developed for Li-ion batteries cannot be directly used for Li/S battery characterisation.

There are only few studies on *in-situ* and *in-operando* XRD characterization of sulphur cathodes [150], [151], [158], *in-situ* Raman [159]; *in-operando* UV-vis [160].

These techniques provide insight into the working mechanism of Li/S battery, in particular in determining of qualitative and quantitative amount of the S species

dissolved in the electrolyte or on the cathode/ anode surfaces, S products appearance at different depth of charge and discharge. The group of Nelson [150], were the first to apply synchrotron based *in-situ* and *in-operando* XRD and TXM on Li/S battery, and they did not observe any Li_2S up to the full discharge which is contradictory to the results gained lately by Canas *et al*. [151] and Walus *et al*. [158]. Canas *et al*. observed Li_2S at 60 % of depth of discharge, whereas Walus *et al*. [158] observed Li_2S formation in the early stage of discharge and moreover they report on appearance of another sulphur allotrope. Indeed such different results require further investigation to understand the reaction mechanism and provide information on the local volume changes during charge-discharge as well as the morphological changes by diverse *in-situ* techniques.

In-situ studies can reveal not only the cathode operation mechanism, but also enhanced understanding of the electrolyte composition effect on the cell performance. *In-situ* XAS studies [45] have yielded valuable information about the effects of solvent on sulphur electrochemistry and reduction mechanism of sulphur in ether based solvents. It also proved the chemical reaction between carbonate-based electrolytes and S cathode.

The above mentioned *in-situ* techniques are mainly aimed on the investigation of chemical and electrochemical behaviour of Li/S battery, they are also one or two-dimensional, therefore the study on morphological evolution of S electrode upon charge or discharge is limited. One such technique that allows observation of the morphology of the electrode in three dimensions and its evolution upon cycling is X-ray CT. The X-ray CT technique has also proved valuable to characterize microstructure of the electrodes in a non-destructive manner. Shearing et al. [156] were the first to apply X-ray tomography to reconstruct a high resolution 3D microstructure of Li-ion graphite anode. In a number of studies [157], [161]–[163] performed on lithium ion batteries it was shown that analytical tools can be used to extract a range of different properties of the electrodes' microstructure which can be coupled with simulations.

Zhou *et al*. applied X-ray tomography to for post-mortem analysis of individual parts of graphene pure sulphur sandwich structure electrode in means of porosity, surface structure and confined sulphur.

Recently Zielke *et al.* [164] has reported the first *ex-situ* X-ray micro tomography images of an elemental S cathode on a 3D current collector and extracted the morphological parameters influencing on the degradation of Li/S positive S electrode in 3 dimensions, like interfacial contact areas, size distributions and spatial distributions. It was shown that the electrode morphology changes drastically after the initial cycle and does not change significantly afterwards moving into an equilibrium state, they also showed the particles size distribution upon cycling. However they have disassembled the cell and thus exposed it to air. This adds up the uncertainty in the results obtained and does not allow to see the change upon cycling in the system with electrolyte and metallic lithium anode.

Additionally the Li/S cell electrochemical behaviour has been investigated by means of electrochemical impedance spectroscopy (EIS) [165]. An important advantage of this method is the capability to characterize and identify in a single measurement, without external influences, different physical or chemical steps taking place in a complex system.

Summary

There is an extensive research on Li/S batteries and it has been significantly improved from the earliest configuration, however there is significant room for its improvement.

In the typical Li/S battery, lithium metal is used as the anode and it is separated from S-based composite cathode by an electrolyte. These three main components should be designed with an integrated approach that focuses on improved cycling stability, high efficiency, and high energy density. All these are in correlation with the following parameters reviewed here: S host structure and matrix, its amount, the electrolyte and additives, separator, current collectors, binder and lithium metal surface.

In the past few years certain improvements of Li/S cell have been achieved by acting on some of these parameters, thus helping to solve issues of poor ionic and transport conductivity of sulphur, volume changing, polysulphides dissolution, leading to significantly improved cell capacity, cycle life and power capability. However the nature of some of these changes is not well understood and still is the subject of discussions.

Ex-situ and *in-situ* studies helped to better understand the Li/S reaction mechanism and processes, but S reduction mechanism is still not fully understood.

In general, the positive electrode should retain its morphology over the cycles so as to decrease the capacity fading. Thus, it is not only the S trapping that is important, but the whole structure of the S cathode. Therefore this research began with the investigation into the preparation of S electrodes in chapter 3. This also provides valuable insights into the links between powder synthesis and electrode optimization.

There are different approaches have been investigated; one of the promising is the use of conductive polymers. The previous studies on conductive polymers in Li/S cell have shown promise for high capacity with good reversibility. The unique properties of the soft polymers and the relatively simple method of fabrication make this type of S cathode attractive for further investigation. Metal oxides, such as Al_2O_3[113]–[116] and $Mg_{0.6}Ni_{0.4}O$ [73], [112] that act as electrolyte absorbents and locally limiting the

polysulphide shuttle effect were added. Electrochemical performances of materials were evaluated and are presented in chapter 4.

As for the electrolyte, since most of the Li/S issues arise due to polysulphides solubility, its composition controls the precipitation reactions happening and its further improvement could boost cell capacity and prevent the shuttle mechanism. Thus, the study on the design of new liquid electrolytes, considering both poor/good solvents for Li polysulphides is important. In the initial study 1 M LiTFSI in TEGDME has been employed. In general, ether based electrolytes proved to be the best solvents for Li/S system. Electrolyte composition could be improved by adding different additives, such as $LiNO_3$, and applying other ether solvents, such as DOL. Although most of these approaches have been applied previously, here we study them with S/conductive polymer composite and metal oxide additive. Thus, the performance of different concentrations of the electrolytes and $LiNO_3$ additive on the overall Li/S cell performance studied. This is described in chapter 5.

Sulphur does not behave like a conventional intercalation or alloy material, and changes in physical state upon cycling. It is solid when fully charged or discharged, i.e. in the form of elemental sulphur S_8 or lithium sulphide Li_2S state form, while the reaction intermediates - ionic or free radical species are soluble in the electrolyte. The cycling behaviour of rechargeable Li/S is dictated by the evolution of the morphology of both electrodes. It is not satisfactory for composite electrodes prepared in conventional manner, because of the dissolution of the active material during the first discharge, which induce significant changes in morphology of the sulphur electrode. X-ray tomography can help to better understand and visualise the structural changes over the cycles. 3-dimensional reconstruction of a Li/S battery electrode can provide the data for the electrode architecture and geometrical parameters, allowing improving the physics-based model for the Li/S battery. Therefore *in-situ* X-ray tomography for the morphology studies is done and shown in chapter 6.

To conclude, it could be noted that though there are still some challenges prior to successful Li/S battery practical implementation, it is one of the most promising high

energy density battery technology. The successful development of the lithium sulphur battery requires careful coordination of the choice of modified electrolyte with the specific nature of cathode material, as lithium sulphur cell is considered as liquid electrochemical cell and the dissolution of polysulphides is unavoidable [81], [166].

CHAPTER III: METHODOLOGY

In this chapter, the general experimental procedure for Li/S battery manufacture, i.e. S composite preparation, mixing, milling, coating and thermal treatments, and battery testing is described. This chapter along with the fabrication steps of the battery introduces the main characterization techniques used.

3.1 Introduction

The experimental work on Li/S battery preparation was carried out in the following order:

- **Synthesis and characterisation of powders and materials for a cathode;**

  This included ball milling of the materials with S and further examination of their morphology, structure and mass ratio of different components in S composites.

- **Fabrication of electrodes and electrolyte;**

  The second phase involved the fabrication of selected S composite into cathodes and the preparation of electrolyte solutions.

- **Battery assembly and electrochemical testing;**

  Battery assembly and cell-testing were performed in the final phase. Electrochemical performances of Li/S cells were evaluated, and are presented in the following chapters 4 and 5.

In the **Table 3.1** the list of characterisation techniques used in this work are summarized. These techniques are described further in this chapter.

Table 3.1 Characterisation techniques

Characterisation	**Method**
Elemental analysis	CHNS
Phase analysis	X-ray diffraction (XRD)
Specific surface area	Brunauer Emmett Teller method (the nitrogen adsorption method) (BET)
Particle morphology	Scanning Electron Microscopy (SEM); Transmission Electron Microscopy (TEM) X-ray Computer Tomography (X-ray CT)
Thermal properties	Thermo gravimetric Analysis (TGA)
Electrochemical properties	Galvanostatic charge-discharge, Cyclic voltammetry (CV), Electrochemical impedance spectroscopy (EIS)

3.2 Materials and chemicals

The list of materials and chemicals used for the synthesis, characterization and electrochemical testing are summarized below:

Table 3.2 List of materials and chemicals

Name	**Manufacturer**	**Additional information**
1-methyl-2-pyrrolidinone (NMP)	Sigma-Aldrich	anhydrous, ≥99.5% purity
Aluminium oxide (Al_2O_3)	Sigma Aldrich	nanopowder, ≤50 nm particles size, 98% purity
Al foil	MTI	≥ 99% purity
Argon		≥99.9995 % purity
Carbon black	Timcal	super C65
Coin cell cases, CR2032	MTI	SS304
1,3-Dioxolane (DOL)	Sigma Aldrich	≥98.5% purity
Glass fibre separator	Whatman	grade GF/D, ≥99.99% trace metals basis
Glycine	Fisher Scientific	≥98.5% purity
Ketjen black© (KB)	AkzoNobel	EC 300 J
Lithium nitrate ($LiNO_3$)	Sigma Aldrich	≥98% purity
Lithium bistrifluoromethanesulfonimide	Sigma Aldrich	≥96% purity

(LiTFSI)		
$Mg(NO_3)_2$	Sigma-Aldrich	≥98% purity
Nickel foam	GoodFellow	≥99% purity
$Ni(NO_3)_2$	Sigma-Aldrich	≥98% purity
Polyacrylonitrile (PAN)	Sigma-Aldrich	average M_w 150,000
Polyaniline (PANI)	Sigma–Aldrich	emeraldine salt, 20 wt. % polyaniline on carbon black
Polypropylene separator	Celgard, USA	25um trilayer membrane
Polyvinylidene fluoride	Kynar	HSV900
Sulphur (S)	Sigma-Aldrich	100-mesh particle size powder
Swagelok© cells	Swagelok©	PFA-220-6
Tetraethylene glycol dimethyl ether (TEGDME)	Sigma-Aldrich	≥99% purity

3.3 S composites synthesis

Sulphur has a very poor electronic conductivity, thus must be mixed with an electronically conductive additive, typically carbon black. In the literature different ways of sulphur electrode preparation are reported, with different types of sulphur and other components as well as various dispersion methods including ball milling, cold and hot sulphur dispersion into carbon or conductive polymer matrix.

In this work “refined” grade, elemental sulphur powder with particle size of 100 mesh, was mixed with commercially available conducting polymers PAN or PANI and ketjen black (KB) as a conducting framework for trapping sulphur.

PAN and PANI were chosen based on the literature review, as they have been reported previously as a buffer for the S cathode volume expansion and adsorbents of the lithium polysulphides.

KB, having an amorphous structure, a median particle size ca. 40 nm, and a surface area of ca. 60 m^2 g^{-1} was selected as conductive material for its high specific surface area and high electrical conductivity. KB nano-particles create a conductive carbon network which allows the electron transfer between sulphur and collector. To create this network S is mixed with KB, this leads to a reduction of the electric conductivity of the S/KB composite due to the destruction of conductive paths when intensive shearing forces are applied.

Ball milling was selected as the best mixing technique, whereby a powder mixture placed in the ball mill is subjected to high energy collision from the milling media. It has been reported by several groups that ball milling process improved the cycle life of the cathode materials for rechargeable lithium ion batteries [29-31] and for lithium sulphur batteries.

The processes included in the electrode fabrication, such as mixing, milling, coating and thermal treatment, significantly influence the electrochemical performance of the battery in general, therefore the fabrication steps have to be well considered and optimised. The influence of the selected preparation steps on the battery performance was studied.

Sulphur with different additives has been mixed by using ball milling technique in a certain weight ratio at 800 RPM for 3 hours with ethanol as a dispersant. After ball milling the composites were dried in oven for 2 hours at 80 ^{0}C to remove ethanol. Subsequently the composites were heat treated for 6 hours up to 300 ^{0}C under argon.

The S content of the heat treated samples was determined by chemical analysis (CHNS) and Thermogravimetric analysis (TGA).

3.4 Characterisation of S composites as cathode materials

For material characterization studies, small batches (0.2 - 0.3 g) of powder were prepared and dried. Prior to fabrication as electrodes, the synthesized powders were characterized for basic powder properties such as specific surface area, density, particle size, particle morphology and phases present. Here the list of techniques that were used in this work.

3.4.1 Chemical analysis of S-composite (CHNS)

To find the S content CHNS analyser based on the classical Pregl-Dumas method [167] was applied, where samples are combusted in a pure oxygen environment, with the resultant combustion gases measured in an automated fashion. This combustion technique allows determination of the percentage of carbon, hydrogen, nitrogen and sulphur in organic compounds. Samples encapsulated in aluminium vials are inserted automatically in the instrument (Vario Micro Cube, Elementar). In the presence of excess oxygen and combustion reagents, samples are combusted completely and reduced to the elemental gases CO_2, H_2O, N_2 and SO_2.

3.4.2 Phase analysis was carried out with X-ray diffraction

Phase analysis was carried out with X-ray diffraction (XRD, a Bruker-AXS D4 system Philips Analytical PW-1710) with Mo radiation at a scanning speed of 2 °/min. by comparing the obtained patterns with relevant JCPDS (Joint Committee for Powder Diffraction Standards) patterns. This technique was applied to determine the structure of magnesium nickel oxide synthesised in this work, the details are given in chapter 4.

3.4.3 BET surface area measurements

The nitrogen adsorption method (Brunauer-Emmett-Teller (BET)) was used for specific surface area measurements and to determine the average particle size (the surface diameter). This measurement technique is based on the physical adsorption of nitrogen at low, constant temperatures.

In this work, liquid nitrogen was used, having a boiling temperature of 73 K. (BET, Micromeritics, Gemini 2370).

Before measurement of pure $Mg_{0.6}Ni_{0.4}O$ and Al_2O_3, the samples were degassed at 150 °C in a vacuum line following a standard protocol, but owing to the volatility of the sulphur, no pre-treatment of the S composites was used. Therefore, due to possibility of water entrapment, and/or pore blockage in the micropores, the obtained values could represent the lower estimates; however, these results demonstrate the trends for comparison between different S composites.

3.4.4 Scanning Electron Microscopy

Scanning Electron Microscopy (SEM, JEOL JSM-840) was employed to investigate the particle morphology and for further confirmation of particle size determined by BET.

Samples were prepared by fixing a small piece of sample with a double-sided adhesive tape on a stub. In order to increase the contrast and quality of images, the samples were sputter coated with a ca. 3 nm layer of gold prior to analysis. Samples after charge/discharge tests were washed with 40 mL solvent composed by TEGDME (to remove soluble components) prior to SEM and EDS measurements.

3.4.5 Transmission electron microscopy

Transmission electron microscopy (TEM) was performed using a Libra 200 transmission electron microscope (Carl Zeiss Microscopy GmbH) operated at 200 keV. The specimen was prepared by dispersing carbon-sulphur powder in ethanol followed by placing a drop on a holey copper film TEM grid. The TEM grid was dried at 50 ºC to remove all traces of ethanol before TEM investigation.

3.4.6 Thermogravimetric Analysis

Thermogravimetric analysis (TGA) is an analytical technique used to observe the change of the sample mass when exposed to the controlled change of mass as a function of time and temperature, thus the thermal properties of the S composites were

established. The TGA measurements were carried out on a TGA Q50 V20.8 Build 34 for a temperature range of 20 to 600 ºC.

3.5 Electrolyte preparation

Electrolyte solutions were prepared in an argon-filled glove box by dissolving LiTFSI in ether based solvents: as the baseline TEGDME solvent was chosen. Additionally for electrolyte optimisation mixture of DOL and TEGDME (1:1 by volume) and $LiNO_3$ additive were employed; the details are given in chapter 5. The electrolyte solution was stirred for 8 hours.

The residual water content was measured by using a Metrohom Karl- Fisher titrator and was found to be below 20 ppm. $LiNO_3$ was dried under vacuum at 80 ºC for 48 h prior mixing. Ionic conductivity of electrolyte solutions was measured using a Mettler Toledo FiveGo FG3 Portable Conductivity Meter and this measurement provides the total ionic conductivity of the solution.

3.6. Fabrication procedure for Li/S coin cells

3.6.1 Electrode coating

The positive electrode consist of 80 % of S composite, 10 % of KB and 10 % polyvinylidene fluoride (PVDF) as a binder. These materials were dispersed in NMP using agate mortar and pestle for approximately 15 minutes to create a uniform mixture.

The resultant slurry was spread onto an Al foil (MTI, ≥h99% purity) by doctor blade technique that allows spreading active material of controlled thickness. Doctor blade is a widely used technique for producing thin films on large area surfaces with accepted precision. The slurry is placed on an Al foil beyond the doctor blade; the thickness of the layer is metered by adjusting the gap between the doctor blade and the current collector. The layer is formed by a doctor blade that moves by a frame along a stationary casting surface.

Once coated the electrodes were dried in an air ventilated oven for 10 h at 55 ºC to remove NMP. At this temperature sulphur volatilization and formation of cracks in the layer due to rapid drying is avoided.

The achieved thickness of electrodes on Al foil current collector is ca. 20 μm weighing in the range of 1.0 – 2.0 mg of sulphur per cm^{-2} depending on the rate pre-treatment techniques. For the cell assembling the coated electrode was cut into discs with 1.6 cm in diameter by disc cutter.

Additionally a 3D porous current collector Ni foam was used. It is heavier and thicker compared to conventional Al foil, thus the coating process is different. The Ni foam was cut into discs prior the coating process. The slurry was spread onto a circular nickel foam (≥99% purity) with 1.6 cm in diameter as shown in **Fig. 3.1** by dip-coating and then dried in an air ventilated oven for 10 h at 55 ºC, after the positive electrode was pressed at 5 MPa by a hydraulic press. The achieved thickness of electrodes on Ni foam is ca. 60 μm, weighing in the range 3 - 5 mg of sulphur per cm^2. An image of pure circular Ni foam, after drying and pressing is presented in **Fig. 3.2**.

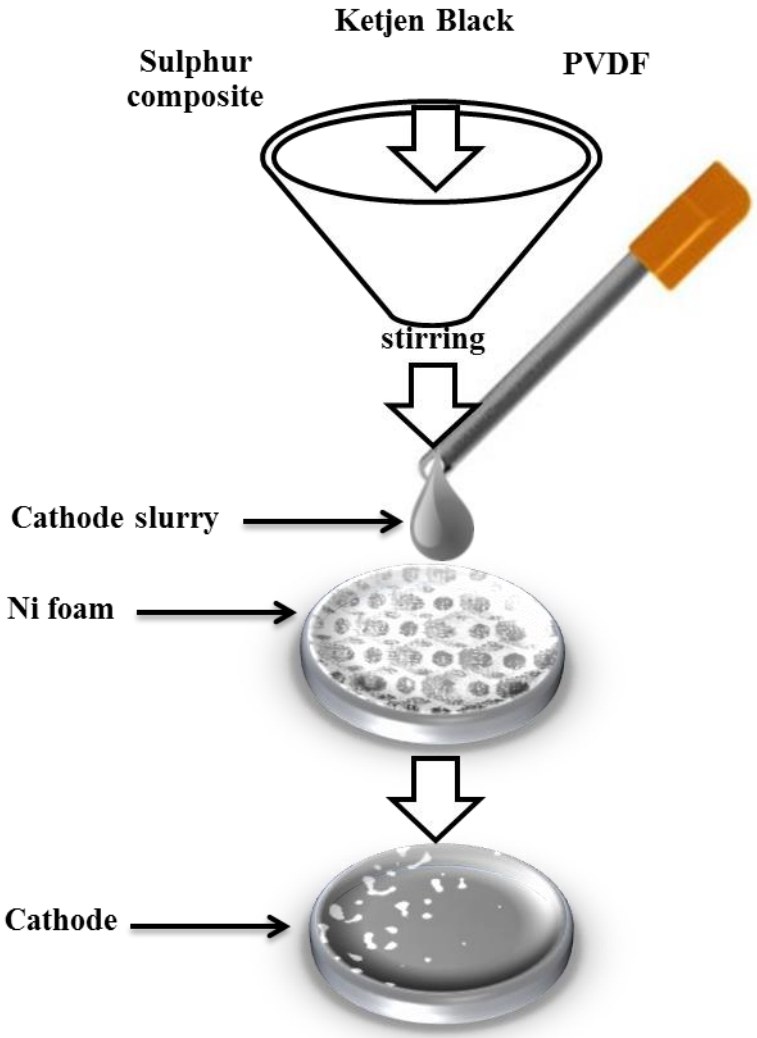

Figure 3.1 Schematic diagram of Ni foam coating

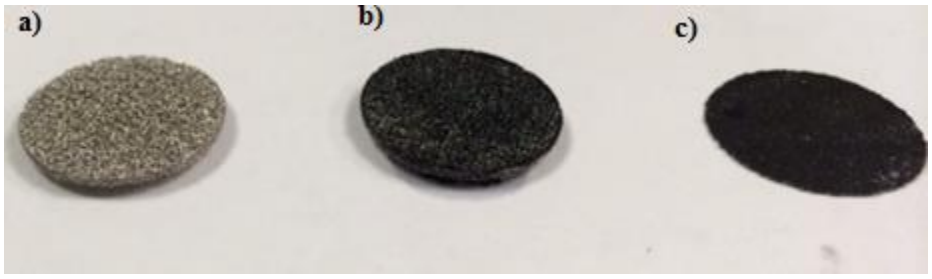

Figure 3.2 Image of a) a pure circular nickel foam; b) the positive electrode on Ni foam after drying; c) after the positive electrode was pressed

3.6.2 Cell assembly

Materials

- Coin cell hardware: includes bottom cell casing, 11/16" stainless steel disc, spring, top enclosure, and insulating ring (MTI);
- Anodes: punched lithium foil for half-cells;
- Cathodes: punched laminates;
- Separator (Celgard, USA);
- Electrolyte: 1M LiTFSI in TEGDME (in chapter 5 other electrolyte composition were examined as well);

CR2032 coin-type cells were assembled inside the glove box by sandwiching a polypropylene separator between the composite cathode and lithium anode (**Fig. 3.3**), and using electrolyte. The cell was placed in the slot of in an MSK 110 hydraulic crimping machine. There is an additional die for cell disassembling purpose as well.

The amount of liquid electrolyte was fixed for simplicity to already existing procedures in coin cell preparation and was ca. 140 μL.

Sulphur/electrolyte ratio for the cells on Al foil, given the mass of sulphur per one coin cell of 0.5-1 mg is 3.5-7 g L^{-1}; and for Ni foam, with the mass of sulphur per coin cell 1.5-2.5 mg, is 10.7-17.8 g L^{-1}. One should note that the exact amount of electrolyte in the coin cell configuration is practically unknown, as while crimping electrolyte is coming out. To control the amount of electrolyte in the system pouch cells are more preferable. The optimised sulphur/electrolyte ratio may be different for each system studied and was not considered here. In the literature the value for sulphur/electrolyte ratio was reported [133] but standard one does not exist, as other parameters have to be taken into consideration: additives' surface area, porosity of the electrode, nature of current collector and thickness & porosity of separator.

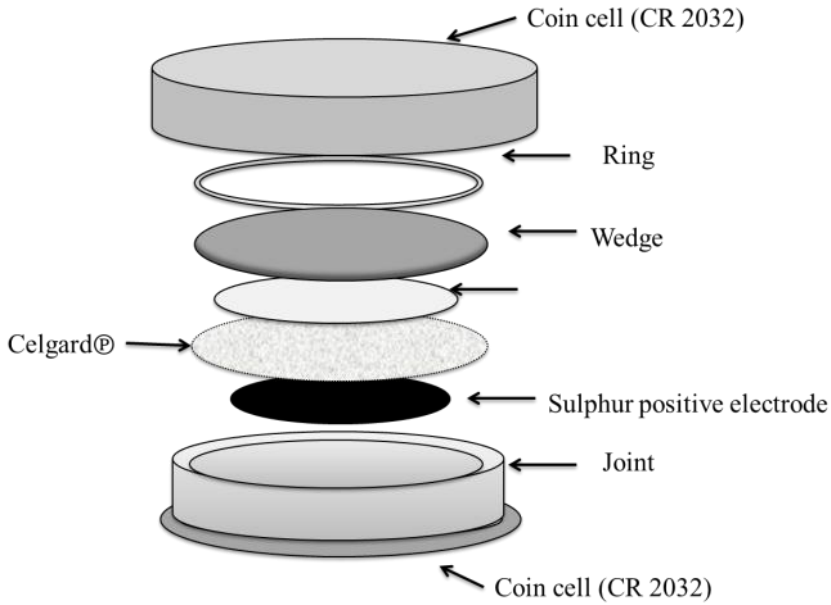

Figure 3.3 Schematic diagram of a 2 electrode coin cell

A bespoke battery for tomography studies was built and tested in a so-called Swagelok© cell. More information concerning the selection of material for Swagelok© is described in chapter 6.

The lithium half cells were kept under rest for 24 hours prior any testing.

Symmetric cell composed of two identical lithium anodes were prepared for studying solely the contribution of electrolyte and its interaction with lithium, and assembled in the glove box in the similar manner by sandwiching a polypropylene separator (Celgrad, MTI Inc.) soaked in the electrolyte between two lithium metal discs. Symmetric cells were tested just after assembling and kept in the same room at controlled temperature.

3.7 Battery characterisation techniques

3.7.1 Electrochemical measurements

Galvanostatic charge/discharge and cyclic voltammetry were used to test electrochemical properties of the cathode materials. Cyclic voltammetry (CV) is used to elucidate cathodic/anodic peaks; from galvanostatic test charge/discharge profile and cycle performances could be achieved. AC electrochemical impedance spectroscopy (EIS) could indicate the resistance of batteries during the reactions.

At least three cells with the same electrode mass loading and electrolyte were tested and average results are presented. All electrochemical measurements were performed at room temperatures and maintained in the range of 19-25˚C.

3.7.1.1 Galvanostatic charge-discharge

Galvanostatic charge-discharge is a useful technique to assess the electrochemical performance of an electrode and its active material and is the most routine experiment to study the behaviour of batteries in operation. The performance of an electrode material is determined as a function of its charge and discharge conditions a given constant current, within a given potential range. The specific current is often expressed as mA g^{-1}, with mass being relative to the amount of active material or it can be expressed in terms of a "C-rate", which is the theoretical amount of charge that can be extracted from a given material within one hour. 1C rate means that the current applied on the battery discharge it within one hour; hence, a 1675 mA h g^{-1} battery discharged at a 1C rate should deliver a current of 1675 mA g^{-1} for 1 hour.

In this study applied currents and specific capacities were calculated on the basis of the weight of S in the cathode. Different voltage windows and current rates were used depending upon the experimental settings. Cycle performances were evaluated by discharging and charging the cells at a fixed current density within a fixed voltage window or charge capacity.

The cells were tested on multichannel battery tester (BT-2000, Arbin), potentiostat/galvanostat (VMP3, Biologic) and battery tester (Neware).

3.7.1.2 Cyclic voltammetry

Cyclic Voltammetry (CV) is a commonly used DC electrochemical technique for studying an electrochemical cell. It allows acquisition of qualitative and quantitative data on the thermodynamics of redox processes and on the electron-transfer kinetics. In a cyclic voltammetry experiment, the voltage of a working electrode vs. a reference electrode is measured in a voltaic cell. The voltage applied to the working electrode is scanned linearly vs. time from an initial value to a predetermined limit. The current represents the rate at which the anodic or cathodic processes are taking place.

The resulting current flowing at the working electrode versus the applied voltage plot is called a cyclic voltammogram (CV). As an example, a typical S electrode arranged into a voltaic cell with lithium metal acting simultaneously as the counter and reference electrode is seen in **Fig. 3.4.** The cell was cycled between 1.5 and 3 V vs. Li/Li+ at 0.1 mV/s.

The redox process corresponds well with the CV of the Li/S battery, which shows two pairs of redox peaks that match with the plateaus on the discharge–charge profiles. The two reduction peaks at ca. 2.4 V (I) and 2.0 V (II) correspond to the conversion of, respectively, high-order lithium polysulphides (e.g., Li_2S_8) to low-order lithium polysulphides (Li_2S_x, $8 > x > 4$) and lithium polysulphides to solid-state Li_2S_2/Li_2S. When the voltage sweep was reversed, the CV plot exhibited a peak at 2.35 V (II') with a shoulder at 2.4 V (I'). This indicates that two oxidative peaks exist and overlap with each other, which corresponds to the reverse reactions of Li_2S_2/Li_2S to low-order lithium polysulphides and low-order lithium polysulphides to high-order lithium polysulphides.

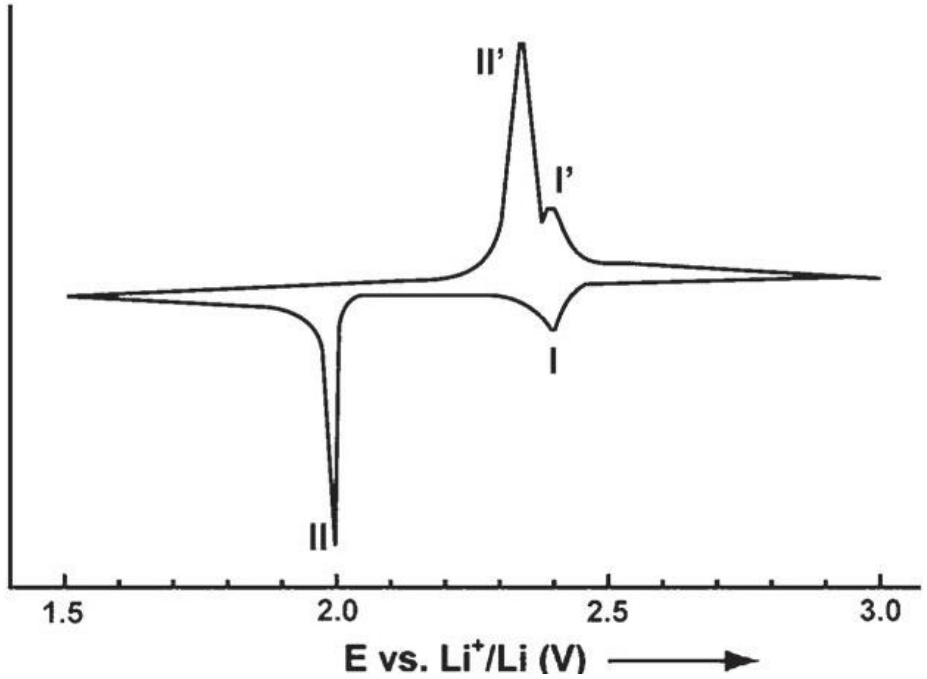

Figure 3.4 Typical cyclic voltammogram of S electrode. (Source: [168])

In this study the CV test was based on two electrodes model, where lithium metal anode acts as reference and counter electrode. Cyclic voltammetry was conducted by means of potentiostat/galvanostat (VMP3, Biologic, Gamry 1000) and on multichannel battery tester (BT-2000, Arbin) at different scanning rate and voltage windows depending upon the experimental settings.

3.7.1.3 Electrical Impedance Spectroscopy

Electrical impedance spectroscopy (EIS) is an AC technique that allows determining the kinetic parameters of the electrode process including processes in the electrolyte, passivation layers, charge transfer and diffusion. EIS is widely used to study the electrochemical behaviour of LiBs [40], [169], [170] and more recently Li/S batteries [129], [148], [171], [172].

EIS is usually measured using a small sinusoidal AC potential of known amplitude and frequency to the electrochemical cell over a constant DC current. The AC

amplitude and phase response are simultaneously recorded. The AC perturbation is applied usually from a high frequency to a low frequency, typically from 10 kHz to 1 Hz. The high frequency perturbation is usually associated with processes in the system that happens quickly, such as charge transfer, whereas low frequency perturbations are linked to the processes that are limiting, such as diffusion.

In DC theory, resistance is defined by Ohm's Law:

$$E = I \times R \qquad \textbf{(3.1)}$$

where E – DC potential, V;

I - current, A;

R – resistance, Ohm

An AC the frequency is non-zero, the analogous equation is:

$$E = I \times Z \qquad \textbf{(3.2)}$$

As in the equation 3.1 E and I are here defend as potential and current respectively. Z is defined as impedance, the AC equivalent of resistance.

In an EIS measurement, the applied current I_t and the resulting AC voltage E_t can be described mathematically as a function of time *t* according to equations:

$$I(t) = I(0)\sin(\omega t + \phi) \qquad \textbf{(3.3)}$$

where I(t) - instantaneous current, A;

I(t) – amplitude of the signal, A;

ω- frequency, in radians per s;

t – time, s;

ϕ - phase shift, in radians.

The excitation signal, expressed as a function of time, has the form:

$$E(t) = E(0)\sin(\omega t) \qquad \textbf{(3.4)}$$

The impedance then is represented as a complex number:

$$Z = \frac{E(t)}{I(t)} = \frac{E(0)sin(\omega t}{I(0)sin(\omega t+\phi)} = Z(0)\frac{\sin(\omega t)}{\sin(\omega t+\phi)} \qquad \textbf{(3.5)}$$

The expression for Z is composed of a real and an imaginary part. If the real part is plotted on the X-axis and the imaginary plot is plotted on the Y-axis, we get the Nyquist plot, which is the most common way of representing complex impedance.

To extract physically meaningful properties of the electrochemical system from the recorded impedance spectra an equivalent circuit model is usually required. Typically the impedance curves for lithium sulphur batteries show two compressed semicircles in the high and medium frequency regions that could be assigned to the charge-transfer resistance and an inclined line approximately 45˚ in the low frequency range, which can be considered as Warburg impedance. An example of a generalized equivalent circuit element for a single cell fuel cell is shown below.

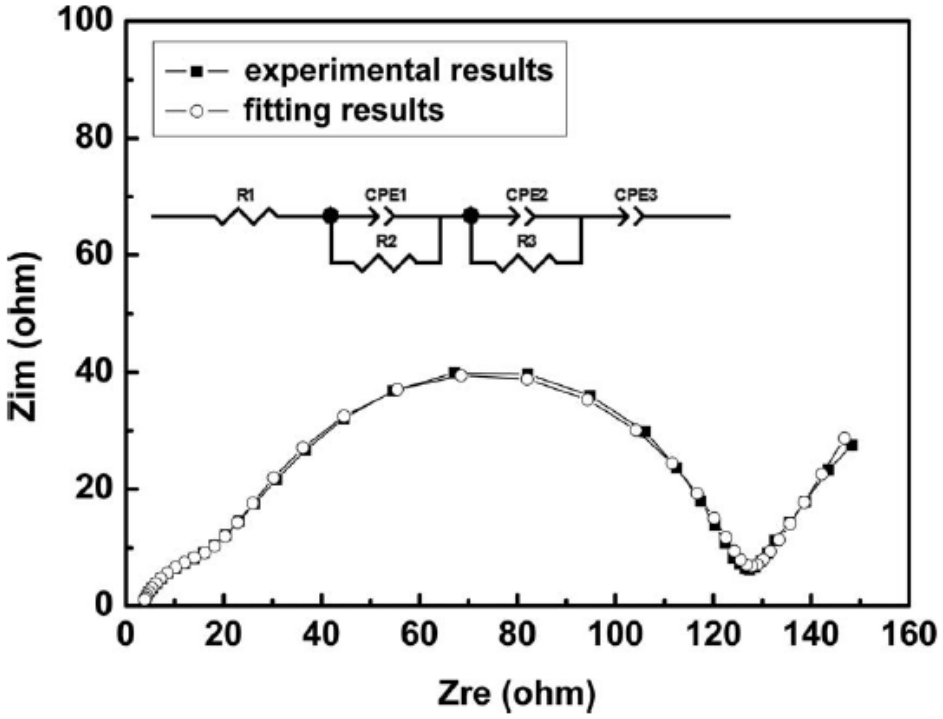

Figure 3.5 Nyquist plot of Li/S cell and its equivalent circuit after fitting (*Source*:[127])

Impedance measurements were conducted on Li/S batteries and symmetrical cells by means of a potentiostat a frequency response analyser (Gamry, Reference 3000). To improve the measurements' accuracy tested cells were placed in Faraday cage, wiring kept as short as possible and where a comparative study was in place the relevant measurements were taken in the same room conditions. The settings of frequency of AC impedance and the applied voltage amplitude are given in the relevant chapters.

3.7.2 Tomography

In conjunction with electrochemistry this research project was focused on the micro-structural characterisation of sulphur based electrodes since the electrode morphology has a profound effect on the cell performance. Although S electrodes can dissolves and therefore behaves differently from the standard Li battery intercalation electrodes, the study of morphological changes upon cycling is crucial in order to design optimal electrode morphologies. There is a link between battery cycle retention and the morphology of the positive electrode.

In electrochemical devices, the primary techniques used to study the microstructural properties and achieve three dimensional microstructural data are focused ion beam (FIB) milling in combination with SEM and X-ray computed tomography (CT). However due to the difficulty of studying sulphur containing materials under high vacuum, here we focus solely on X-ray CT.

X-ray tomographic microscopy is an advanced form of transmission X-ray microscopy and is becoming increasingly popular as a non-destructive *in-situ* technique for studying electrochemical device morphology. This technique as a diagnostic tool was initially introduced in medicine and was then widely used across different disciplines; detailed reviews of the use of X-ray computed tomography have been published by Maire *et al.* [173] and Stock *et al* [174].

An X-ray beam penetrates an object and is attenuated due to interactions with the electrons of the material. The sample is rotated through 180˚ while the transmitted x-rays are recorded and then converted to visible light by a scintillator, these data are

digitized and a series of 2D images are obtained. From these images a 3D representation can be reconstructed using back-projection algorithms.

Attenuation is the extent to which X-ray energy is lost in a material, so the denser the object is the more X-rays incident on it are attenuated according to the Beer-Lambert Law (3.6) which states that the attenuation is exponential. By measuring this attenuation, material properties and microstructures can be identified and characterised.

$$I = I_0 \exp(-\mu x) \qquad \textbf{(3.6)}$$

where I_0 is the intensity of the incident X-ray;

I is the beams intensity after it traverses a thickness of material;

x - linear attenuation coefficient;

μ - coefficient, which is inversely related to the mean free path of the beam.

Mass attenuation is dependent on the effective material atomic number and the photon energy of the X-ray beam.

In conventional X-ray CT, also referred to as X-ray absorption tomography, X-rays which traverse an object along different path are differentially absorbed, and the intensity pattern of the emerging beam registers the distribution of absorbing materials within the object. An alternative approach that is useful for low attenuating objects is phase contrast imaging which instead records variations of the phase of the emerging radiation.

X-ray CT has already been performed on lithium-ion batteries. Shearing *et al.* [156] were the first to apply this technique for studying a 3D microstructure of a graphite negative electrode from a Li-ion battery. *In-situ* X ray tomography on lithium ion batteries has become increasingly popular for example the work of Ebner *et al.* [175] who studied the morphological evolution of SnO particles upon lithiation/delithiation in modified Swagelok© cell.

In order to study batteries *in –situ* using X-ray CT, and to allow for the required rotation, bespoke cells have been developed with cylindrical shape and manufactured from X-ray transparent materials, such as the polymeric Swagelok© cell [175] and Kapton capillary tube [176]. Ordinary pouch cells have also been used [177], but due to its flat shape the angular range is limited to 140˚.

In this work *in-situ* X-ray micro-tomography was performed on a lab-scale micro tomography instrument, the Xradia Versa 520, (Carl Zeiss Inc) utilizing a polychromatic microfocus source containing a tungsten target with the tube voltage set at 50 kV and a low energy filter. The battery for the tomography study was assembled and tested in a modified Swagelok© cell (PFA-220-6, Swagelok) before and after cycling.

During tomographic data collection, an optical magnification of 20X was used, and a binning of 2 was set on the 2048x2048px CCD detector, resulting in a pixel size of approximately 780 nm and a field of view of approximately 750 μm. For each set of tomography data, 1601 radiographic projections were obtained at discrete angular steps. The radiographic projections collected were reconstructed using ZEISS Xradia's proprietary cone beam filtered back projection algorithm to produce a set of tomographic slices making up a cylindrical volume.

In addition *ex-situ* X-ray absorption contrast nano-tomography was performed on Xradia Ultra 810, Carl Zeiss Inc utilizing a microfocus rotating anode X-ray source (MicroMax-007HF, Rigaku), with the voltage set at 35 kV and current at 25mA. The S electrodes coated on the Al foil were scraped onto a fine needle to obtain a sample of approximately 65 μm in diameter.

The transmission images were reconstructed in 3D using standard reconstruction methods, the reconstructed tomograms were processed using Avizo 7 Fire (FEI, SVG, France). The details for each setting are given in chapter 6.

.

Summary

In this chapter the experimental techniques and methods used are described. An overview of the different characterisation techniques adopted has been presented.

The research work consists of two main parts: the first covers the fabrication and characterisation of the electrochemically active material, the second part involves the application of these S composites as electrodes in Li/S battery and further study on their performance and degradation..

CHAPTER IV: OPTIMISATION OF CATHODES

The processes included in the cathode fabrication play an important role in the electrochemical performance of the battery. In this chapter the cathode materials used in this work and the influence of selected preparation steps on the battery performance are presented. Nanostructured magnesium nickel oxide $Mg_{0.6}Ni_{0.4}O$ and alumina Al_2O_3 were studied as additives to sulphur/polyaniline (S/PANI) composites via wet ball-milling of sulphur and polyaniline followed by heat treatment.

4.1 Introduction

One of the main objectives in cathode development is that processes should be easily and reproducibly fabricated with industrial scale throughput. The cathode should present high capacity at the beginning of the cycle to assure a high conversion of the active material.

Here we report the use of commercially available conducting polymers: PAN and PANI; and KB, as a conducting framework and as a host or coating media for S cathodes. Additionally small amounts of metal oxide additives such $Mg_{0.6}Ni_{0.4}O$, Al_2O_3 were also tested in the system for their adsorbing and catalytic properties.

The compositional details of the S composites with conductive polymers, metal oxides prepared in this study are given below in **Table 4.1**:

Table 4.1 List of S-composites investigated in this study

N	S composite	Initial mass ratio respectively
1	S/PAN/KB	40/10/50
2	S/PANI/KB	40/10/50
3	S/ PANI/$Mg_{0.6}Ni_{0.4}O$	4:1:0.25
4	S/PANI/Al_2O_3	4:1:0.25
5	S/PANI	4:1

In S cathode synthesis it is important to obtain a homogenous layer in which the sulphur particles are covered and in contact with conductor, while PVDF creates bindings between particles and with the current collector. Moreover the cost associated with the synthesis method has to be taken into account, therefore this chapter starts from the study on the influence of the synthesis route on the performance of the Li/S battery.

There are various approaches that can be used to prepare a S/polymer composite, which include: a) coating by mixing conductive polymer and sublimed sulphur with further heat treatment, thus letting organo-sulphur bonds to be formed [70], [73], [75]; b) incorporation of the sublimed sulphur on polymer nanotubes [71], [76]; c) *in-situ* deposition of sulphur with conductive polymer [109], [111]. In this work we have adopted the first approach due to its simplicity and ease of scale up.

Several parameters and steps in the cathode fabrication were modified during the course of this work and final cathode fabrication settings were selected and optimized based on the process simplicity and battery performance. The aim is to understand the impact of the composition and preparation of the positive electrode on the performance of Li/S batteries.

Furthermore, in this work, inorganic ceramic fillers (oxide additives) such as $Mg_{0.6}Ni_{0.4}O$ and Al_2O_3 have also been employed to further improve the cathode

conductivity and to prevent polysulphides shuttling into organic electrolytes by using them as electrolyte absorbents, locally limiting the polysulphide shuttle effect. In the second part of this chapter we report comparative studies of the effect of two metal oxides on the S/polyaniline (PANI) composite cathode performance in lithium cell, both capacity and cycle life.

4.2 Optimization of cathode preparation parameters

In this work we have selected the method of sulphur preparation that involves two steps: coating by mixing conductive polymer and sublimed sulphur with secondary heat treatment. In the first step S is mixed in a defined ratio with additives by ball milling technique in ethanol. In the second step obtained S-composites are heat treated in an argon atmosphere. Therefore the ball milling and heat treatment settings could be optimized.

Additionally, two different current collectors were used: Al foil and Ni foam. In most studies in the literature aluminium foil was used as a current collector of sulphur cathode [122]. However, it was suggested by Zhang [123] that Al metal can react with sulphur. Therefore porous Ni foam current collectors have also been used here.

To study the effect of preparation settings polyacrylonitrile (PAN) and polyaniline (PANI) have been mixed with S along with KB in the certain ratio (**Table 4.1**), made into slurry and coin cells as it was described in chapter 3.

4.2.1 Effect of ball milling

The ball milling method is a mechanical mixing route which uses high energy collision from the balls. The ball mill can grind and homogenize small sample volumes at the nano scale. The ball milling time and speed have been optimized based on its effect on the S composite properties and performance in Li/S battery.

In the initial step, S was mechanically mixed with PANI and KB in 4:1:5 mass ratio respectively with 1 ml of ethanol as dispersant using a high-energy planetary ball-milling machine (Fritsch, Pulverisette 7) in 45 ml cubic zirconium jars using 2 mm

cubic zirconium balls. At first, the ball mill was operated at different rotational speeds: 400, 600, and 800 RPM for 3 h. Then the duration of the ball mill was also optimized and powders were milled for the different duration at 800 RPM: 1 h, 2 h, 3 h, 4 h and 5 h.

After milling the resulting S composites were dried at 80 C for 2 h in an air-ventilated-oven. The milled powders were subjected to a two stage heat treatment in a tube furnace (Elite Thermal Systems Ltd.) under a constant flow of argon gas. The first stage consisted of a ramp up in temperature from ambient conditions to 160°C at a rate of 10°C per min, followed by a dwell step at 160°C for 3 hours. The second stage consisted of a ramp up in temperature from 160°C to 300°C at a rate of 10°C per min, followed by a dwell step at 300°C for 3 hours.

In order to observe the influence of the ball milling on capacity S/PANI/KB composites were made into slurry with PVDF and KB in 80:10:10 mass ratio respectively, coated on Ni foam as a current collector, dried in a vacuum oven and assembled into an electrochemical cell with Li metal and 1M LiTFSI in TEGDME as electrolyte. The performance was measured at 0.1C between 1 to 3 V.

It was found out that ball milling speed and time affect the specific surface area of the samples.

The effect of the rotation speed on the specific surface area of the milled S composites synthesized with a milling time of 3 h is shown in the **Fig. 4.1**. It can be seen that the BET specific surface area slightly increases with the increasing rotation speed. However, the difference is not significant and is ca. 2 $m^2 g^{-1}$; whereas the effect of milling time (**Fig. 4.2**) is noticeable and the difference between S composites ball milled for one hour and for three hours is ca. 25 $m^2 g^{-1}$.

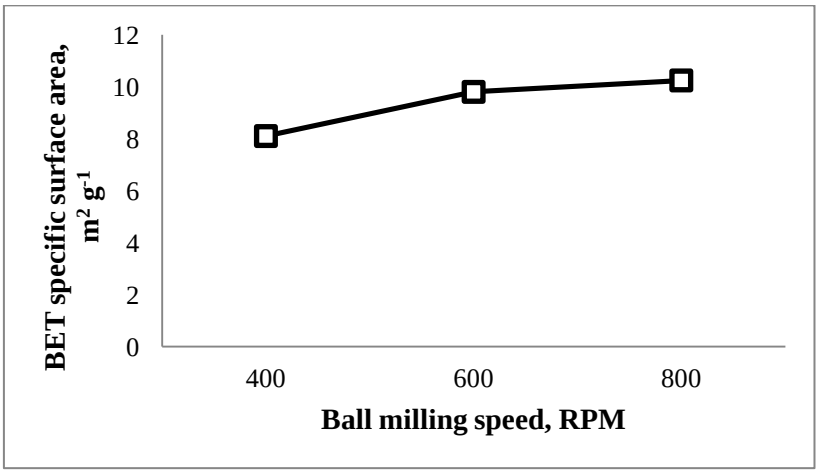

Figure 4.1. BET specific surface area of the milled S/PANI/KB at different ball mill RPM speed, duration is 3h

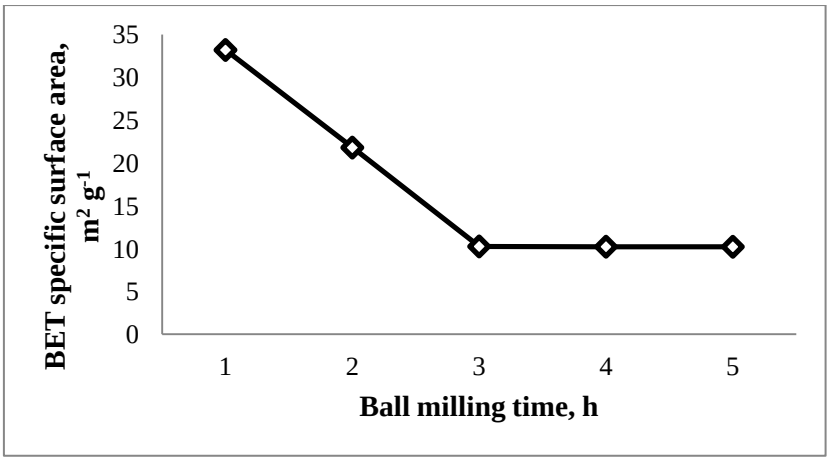

Figure 4.2. BET specific surface area of the milled S/PANI/KB at different milling times, ball mill speed 800 RPM

The specific area of the composite decreases with the increasing milling time, as primary structures of KB can be destroyed when intensive shear stress is applied, and reaching a fixed value since milling of coarse particles and agglomeration of finer particles may happen simultaneously after reaching 3 h of ball milling. Therefore, a further increase after 3 h does not change the surface area of the samples.

Fig. 4.3 indicates the variation of the first discharge capacity of the milled S/PANI/KB composites with the ball mill rotational speed. It can be observed that the initial discharge capacity increases with the increase of ball mill rotational speed: ca. 1400 mA h g^{-1} at 800 RPM and ca. 800 mA h g^{-1} at 400 RPM.

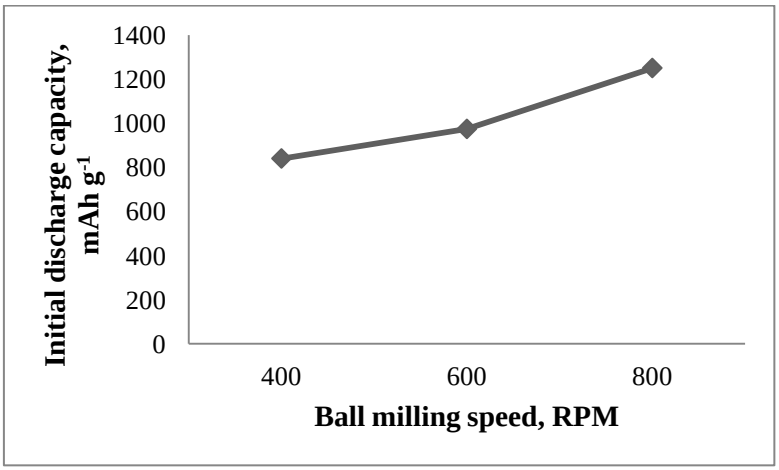

Figure 4.3. Effect of the ball mill RPM speed on the initial discharge capacity of the battery, duration 3 h

Fig. 4.4 indicates the variation of the first discharge capacity of the milled S/PANI/KB composites at 800 RPM with the milling time. The initial discharge capacity increases remarkably from 680 mA h g^{-1} to 1250 mA h g^{-1} after prolonging the milling time from 1 h to 3 h respectively. There is no noteworthy change after further increase to 5 h; this correlates to the BET data, as the surface area after 3 hours of ball milling did not change as well (**Fig. 4.2**).

However, the BET surface area decreases with the raise of milling time, whereas the capacity remarkably increases after prolonging the milling time to 3 hours. Theoretically high surface area provides the greater capacity for charged particles, however these results demonstrated that other factors i.e. the contact between S and conductive carbon and polymer also affect the battery capacitance. SEM and EDS studies of the ball milled S composites should be performed in the future to confirm this pattern.

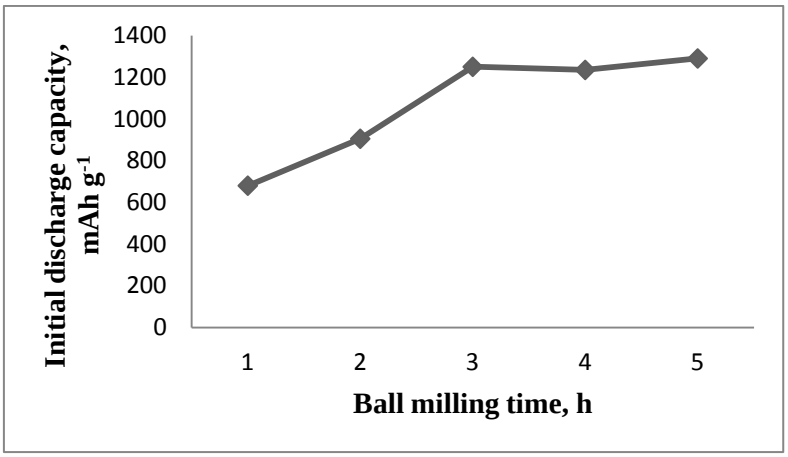

Figure 4.4 Effect of the milling time on the initial discharge capacity of the battery. 800 RPM

As a result, a rotation speed of 800 RPM with a milling time of 3 hours was selected as the optimized process conditions. All subsequent ball milling of S composites was carried out at 800 RPM for 3 hours.

4.2.2 Effect of the heat treatment

The second step in S composite preparation that could be optimized is heat treatment. A variety of different heat treatment parameters are found in the literature, for example in [100] there are two steps at 150°C for 5 hours and 300°C for 3 hours. In [178] S/PANI/AB composite, after ball milling the sample was heat treated also in two steps at 160°C and at 300°C but for 24 hours in total, in [77] similar settings were used but shorter in duration heated at 155 °C for 3 h and at 300 °C for 2 h. Although the time and temperature is variable, the common pattern is that S composite heat treatment includes two steps.

The first heat treatment step is essential for the encapsulation of elemental sulphur in the conductive carbon host [179]. At 160°C temperature the molten sulphur has the lowest viscosity [180], which enhances the diffusion and encapsulation of sulphur into the pores of the conductive host, acting to improve the cycling stability of the S-composite.

The second step, carried out at 300°C, acts both to increase the rate of sublimation of excess bulk sulphur and to encourage the formation of a ternary composite consisting of C-S bonds under the presence of polyaniline [178], this also prevents the formation of large areas of insulating elemental sulphur and at the same time increasing the adsorption of sulphur into the matrix.

Based on the literature review here we have adopted two-stage process: the first stage was at 160°C for 3 hours and the second stage at 300°C for 3 hours. In contrast in [70] S/PPy composite was prepared by ball milling without heat treatment and cell still exhibited competitive electrochemical performance and reached ca. 600 mA h g^{-1} after 20 cycles. Therefore we have also investigated whether the heat treatment step could be avoided and thus the preparation process simplified.

S was mechanically mixed with PAN or PANI and KB in 4:1:5 mass ratio respectively with 1 ml of ethanol as dispersant using a ball-milling machine at 800 RPM for 3 hours. After milling the resulting S composites were dried; and part of the milled powders was subjected to a two stage heat treatment in a tube furnace under a constant flow of argon gas. Part of the S-composites did not undergo any heat treatment (non-heat treated composites).

The heat treated and non-heat treated composites were made into slurry with PVDF and KB in 80:10:10 mass ratio respectively, coated on Ni foam as a current collector, dried in a vacuum oven and with Li metal as anode and reference electrode, 1M LiTFSI in TEGDME as electrolyte were assembled into coin cells. CV was conducted using a potentiostat (Gamry, Reference 3000) at a scan rate of 0.05 mV s^{-1} between 1 and 3 V *vs.* Li^+/Li.

Fig. 4.5 shows the cyclic voltammetry curve of a lithium battery with the heat treated S/PAN/KB composite, which provides more detailed information of equilibrium of electrochemical reaction within the full charge-discharge voltage range 1.0 V - 3.0 V. The cathodic peak located at 2.4 V corresponds to the reduction of elemental sulphur to soluble polysulphides (Li_2S_x, $2<x<8$). The second cathodic peak at 2.0 V can be assigned to the further polysulphides to insoluble polysulphides (Li_2S or Li_2S_2). The

sharp anodic peak around 2.35 V corresponds to the conversion of polysulphides to sulphur during the charge process. On the initial first cycle there was a pronounced reduction process, it is believed that this is due to the SEI formation, as it was not observed with further cycling.

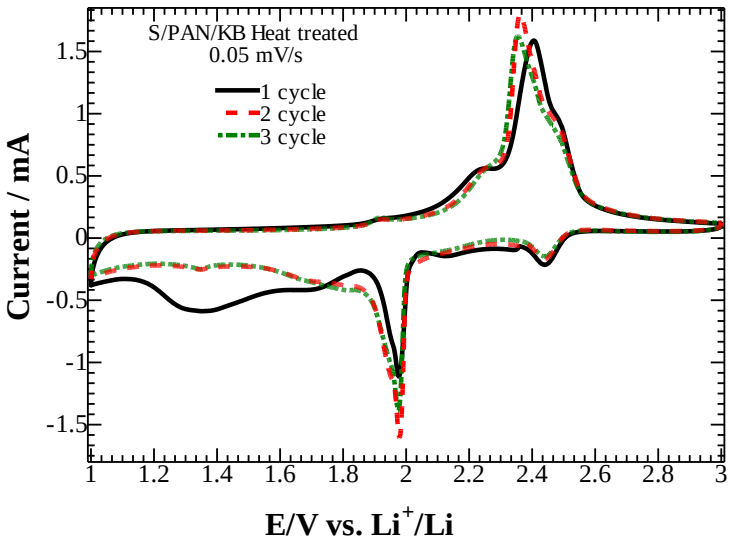

Figure 4.5 Cyclic voltammogram of the cell with heat treated S/PAN/KB, cycling rate 0.05 mV/s

In **Fig. 4.6** the cyclic voltammogram for the same non-heat treated composition is shown. The cells failed to discharge to 1 V, thus the operating window was decreased to 1.5 – 3 V; however, the CV is not similar to the typical of Li/S battery. The cathodic and anodic peaks not coincident with the peaks for heat treated sample (**Fig. 4.5**), with much less reproducibility. There is a clear indication that after heat treatment these cells have better electrochemical performance.

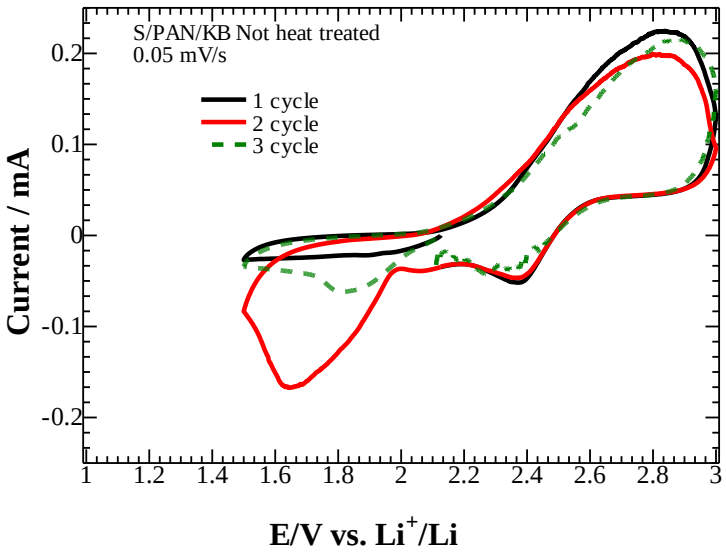

Figure 4.6 Cyclic voltammogram of the cell with not heat treated S/PAN/KB, cycling rate 0.05 mV/s

Fig. 4.7 shows the cyclic voltammogram of a Li/S battery with heat treated S/PANI/KB composite, the cyclic voltammogram is coincident with typical electrochemical reactions of elemental S. Two cathodic peaks at 2.45 V and 1.9 V represent two-stage process as in S/PAN/KB voltammogram.

In **Fig. 4.8** a cyclic voltammogram of the cell with non heat treated S/PANI/KB is presented. It could be seen that cathodic and anodic peaks are coincident with the peaks for the heat treated composite. However, the peaks for reduction processes are less intense and wider, thus confirming that the heat treatment enhances the cell electrochemical performance.

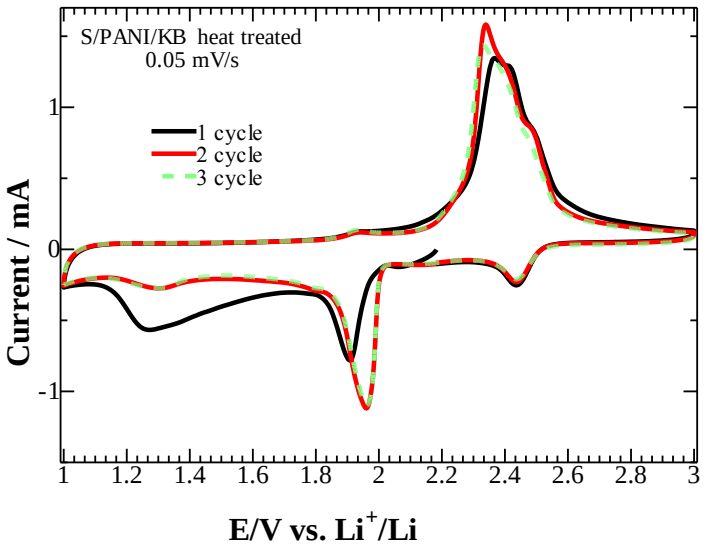

Figure 4.7 Cyclic voltammogram of the cell with heat treated S/PANI/KB, cycling rate 0.05 mV/s

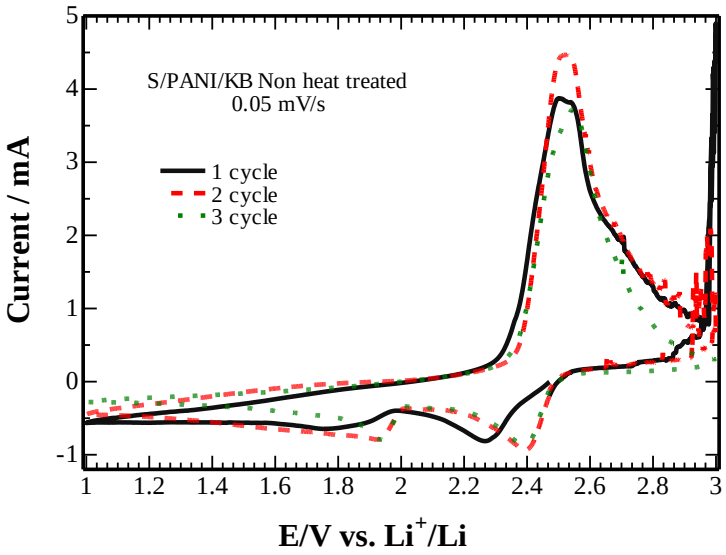

Figure 4.8 Cyclic voltammogram of the cell with not heat treated S/PANI/KB, cycling rate 0.05 mV/s

In general, heat treated samples have higher peak intensity and similarity between oxidation and reduction peaks, they are more stable performance over cycles as well.

In conclusion, there is a tendency, that the heat treated sample have better electrochemical performance and give higher discharge capacity, this could be attributed to the cross-link reactions between conducting polymer and sulphur happening during the heat treatment as shown by Zhao *et al.* in [178] for S ternary composite with PANI, so sulphur could be trapped in composites not only by physical adsorption. The heat treatment regime in this work was different from the one applied by Zhao *et al.* [178], in their study they heat treated the sample for up to 24 hours in N_2 atmosphere. Even though this shows the necessity of S composite heat treatment, thus all subsequent samples were heat treated.

4.2.3 Effect of current collector

S/PANI/KB composites were tested at 167.5 mA g^{-1} (0.1 C) on Ni foam (**Fig. 4.9**) and Al foil (**Fig. 4.10**) as current collectors. Initial charge-discharge profile do not vary significantly, but from the discharge capacity retention profile it can be seen that the discharge capacity for Al foil samples over 100 cycles drops significantly compared to the sample on Ni foam.

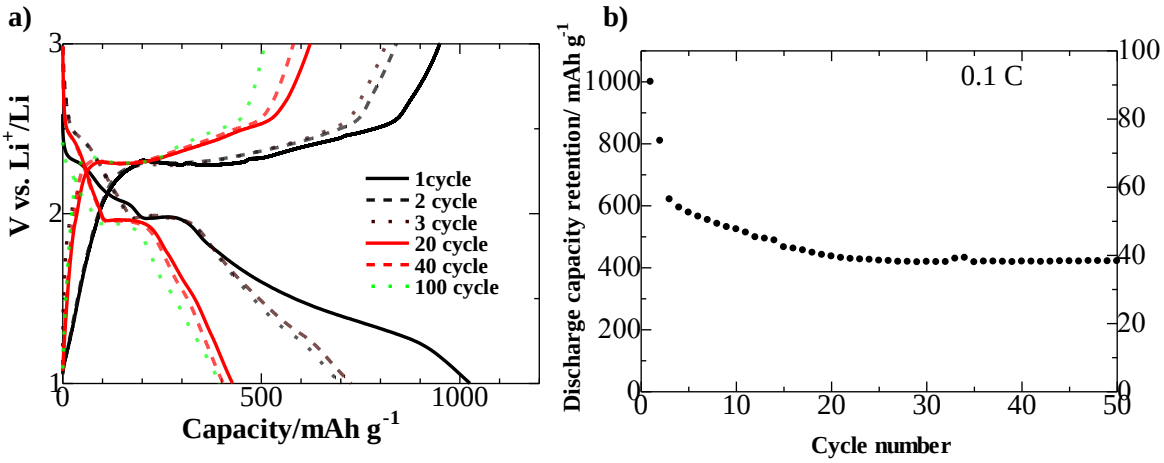

Figure 4.9 a) Charge-discharge profiles of cells with the ternary composites (S/PANI/KB), heat treated on Ni Foam, 0.1 C; b) discharge capacity retention for the same sample.

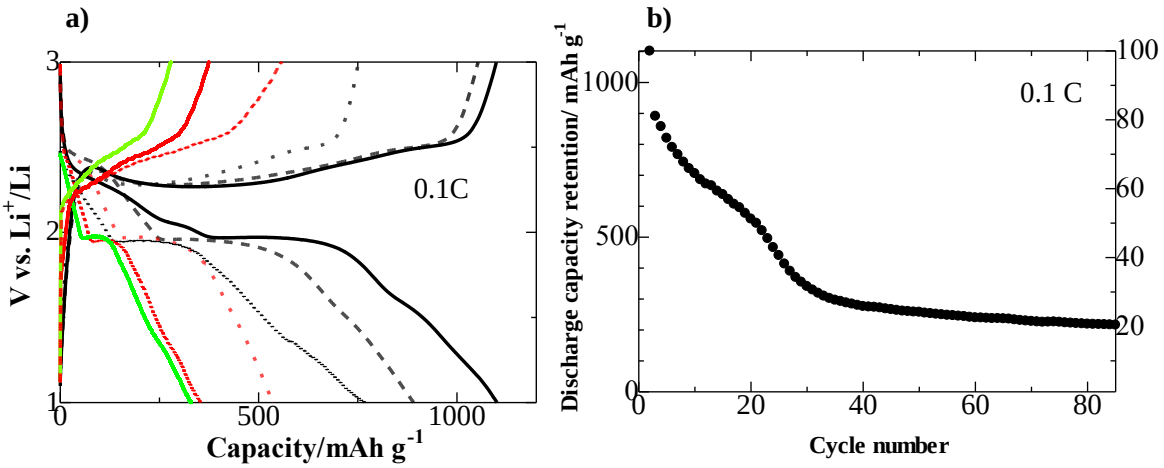

Figure 4.10 a) Charge-discharge profiles of cells with the ternary composites (S/PANI/KB), heat treated on Al foil, 0.1 C; b) discharge capacity retention for the same sample

As seen from **Fig. 4.9b** within the initial 20 cycles the discharge capacity of S/PANI/KB composite on Ni foam decreased quickly to ca. 400 mA h g^{-1} and became relatively stable over the subsequent 80 cycles. Whereas for the same composite on Al foil the discharge capacity decreased after 25th cycle to ca. 250 mA h g^{-1}, that is ca. 20% of the initial discharge capacity.

This confirms the initial results and shows that electrochemical performance of the cell with porous current collector Ni foam is more stable, this may also be due to Al reaction with sulphur as described by Zhang [123]. Ni foam is heavier and thicker compared to Al foil, thus theoretically it is less prefereable in terms of achieving high gravimetric and volumetric energy densities. However, it allows increasing the active material loading as well as improved the battery performance.

4.3 Effect of metal oxide additives

4.3.1 Experimental

The synthesis of $Mg_{0.6}Ni_{0.4}O$ was carried out as described by Zhang *et al*. in [73] by the self propagating high temperature synthesis method. 0.6 mol $Mg(NO_3)_2$, 0.4 mol $Ni(NO_3)_2$ were dissolved in 100 mL deionized water and glycine was added into the solution. The solution was thoroughly stirred and boiled to evaporate the excess water. The resulting liquid was placed and heated in an oven at 200°C, where it ignited and underwent a self-sustaining combustion process. The final product was an ash composed of nickel and magnesium oxides. The powder was calcined at different temperatures for 6 h in air and then ground in an agate mortar.

Sulphur, polyaniline and $Mg_{0.6}Ni_{0.4}O$ (as prepared) or Al_2O_3 were mixed in the mass ratio of 4:1:0.25 by wet ball milling at 800 RPM for 3 hours with ethanol as a dispersant. The sulphur/polyaniline binary composite was mixed in the same way in the mass ratio of 4:1.

The S-composites were dried in an air-ventilated oven for 2 h at 100 °C to remove the remaining ethanol; and finally heat treated in two subsequent steps for 3 h at 160 °C followed by 3 h at 300 °C under argon in a tube furnace.

The electrodes were prepared by mixing the active material (S/PANI, S/PANI/Al_2O_3, S/PANI/$Mg_{0.6}Ni_{0.4}O$ composites) with KB, PVDF in a mass ratio of 80:10:10, respectively, in N-methyl-2-pyrrolidone. The resultant slurry was uniformly spread onto a Ni foam discs with a diameter of 1.6 cm and dried at 70 °C for 12 h in air-ventilated oven. After this, the electrodes were pressed by a hydraulic press at 5 MPa to enhance contact between the active material and Ni foam current collector.

The thickness achieved was ca. 60 μm, and the mass of the electrodes were in a range 8–10 mg cm^{-2}, which gives a resultant areal capacity of over 2 mA h cm^{-2}. For a fair comparison the electrodes examined were of equal mass.

Electrochemical tests of the S/composites were performed using the coin-type cells (CR2032) with lithium metal foil as the counter electrode. CR2032 coin-type cells were assembled in a glove box filled with high purity argon by sandwiching a polypropylene separator between the composite cathode and lithium anode and using 1 M $LiPF_6$ TEGDME as the electrolyte.

Galvanostatic charge/discharge and cyclic voltammetry were used to test the electrochemical properties of the cathode materials. CV was conducted using a potentiostat (Gamry, Reference 3000) at a scan rate of 0.05 mV s^{-1} between 1 and 3 V *vs.* Li^+/Li. The cells were cycled galvanostatically using a multichannel battery tester (BT-2000, Arbin), in the range 1 to 3 V *vs.* Li^+/Li at 0.1 C. Impedance measurements were conducted by means of a potentiostat with frequency response analyser (Gamry, Reference 3000). The frequency of AC impedance was varied from 0.1 Hz to 1 MHz with applied voltage amplitude of 5 mV. Applied currents and specific capacities were calculated on the basis of the mass of S in the cathode. All electrochemical measurements were performed at room temperatures.

4.3.2 Physical characterisation of S-composites

Fig. 4.11 shows the XRD pattern of $Mg_{0.6}Ni_{0.4}O$ powder. The diffraction peaks at 2Θ = 6º, 16.7º, 19.5º, 27º, 6º, 32.4º, 34º were attributed to (001), (111), (200), (220), (311), (222) planes of the face centred cubic structure of $Mg_{0.6}Ni_{0.4}O$. This shows that the synthesised material is $Mg_{0.6}Ni_{0.4}O$ powder. The microstructure of the $Mg_{0.6}Ni_{0.4}O$ was also studied by TEM (**Fig. 4.12**). The TEM image in **Fig.4.12** shows that $Mg_{0.6}Ni_{0.4}O$ has nanostructure which consists of the particles less than 30 nm, and a mean diameter d_p = 20 nm. The particle size distribution was obtained from the grayscale TEM image by applying ImageJ software. The grayscale input image was passed through a histogram enhancement step to reduce the effects of different lighting conditions at the background.

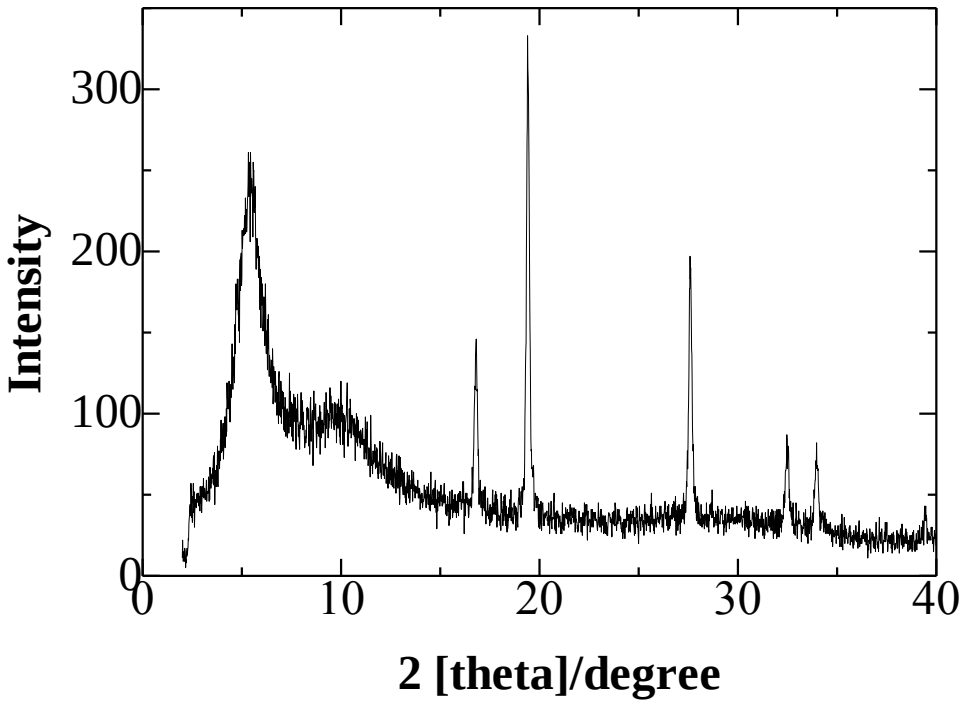

Figure 4.11. XRD pattern of the as prepared $Mg_{0.6}Ni_{0.4}O$

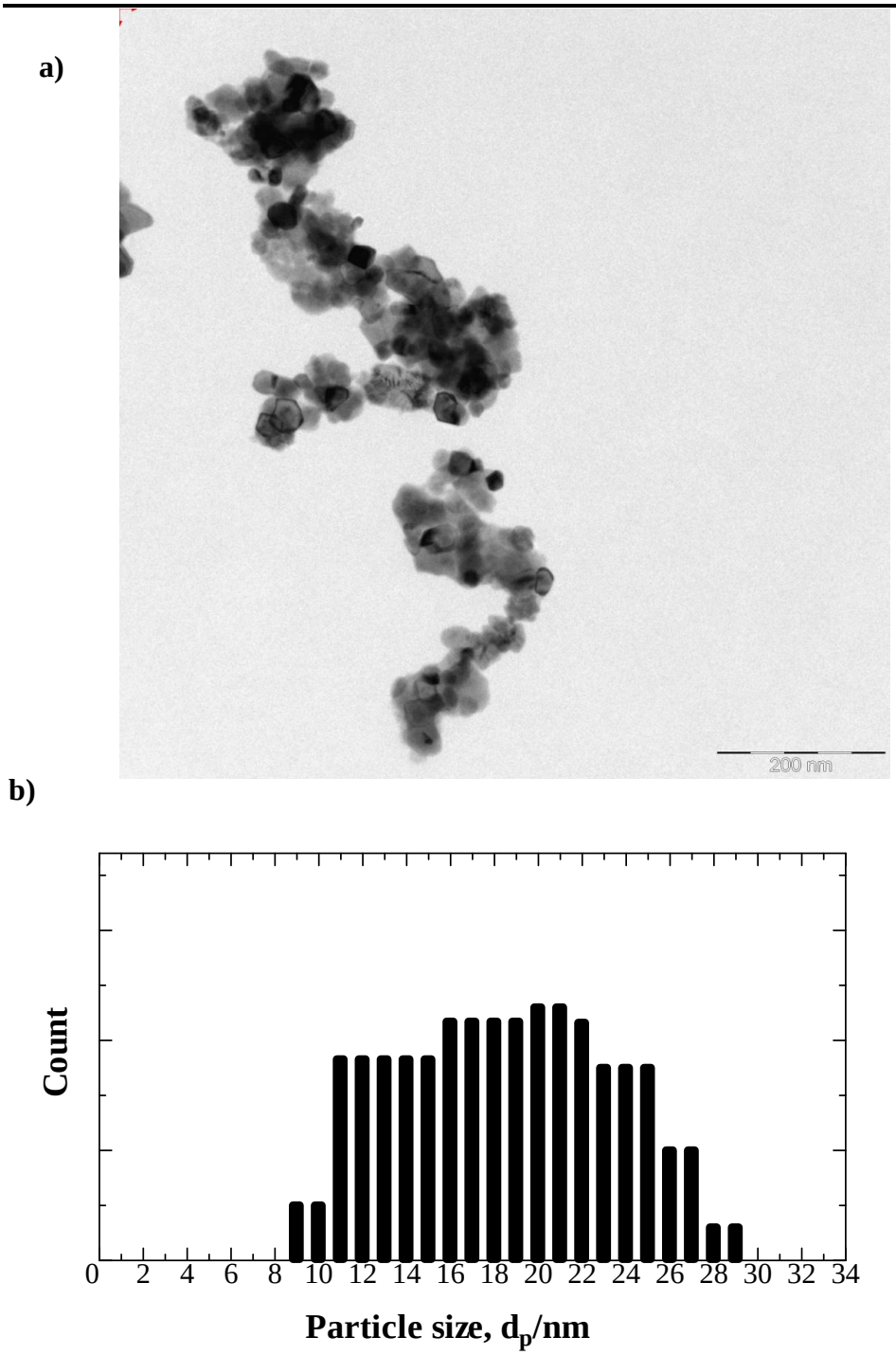

Figure 4.12 a) TEM image of $Mg_{0.6}Ni_{0.5}O$; b) particle size distribution

The composition of the sulphur composites prepared in this study is given in **Table 4.2**.

Chemical analysis has shown ca. 30 % of sulphur loss during the heat treatment process (**Table 4.2**).

Table 4.2. List of S-composites

S composite	**Initial mass ratio respectively**	**Initial S content, mass %**	**S content after the heat treatment by CHNS, mass %**
S/PANI	4:1	80 %	43
S/PANI / $Mg_{0.6}Ni_{0.4}O$	4:1:0.25	≈76 %	42
S/PANI / Al_2O_3	4:1:0.25	≈76 %	42

In **Table 4.3** the BET specific area of the S-composites is given: S/PANI/$Mg_{0.6}Ni_{0.4}O$ has the highest BET area of 18.1 m^2 g^{-1} among the S-composites prepared in this work.

The BET isotherm obtained was of type 1, which is known to correspond to macroscopic surface area: because of the sulphur content of the composite, and its tendency to sublime at elevated temperatures, it is not possible to carry out the heat pre-treatment typical of BET measurements, without the risk of damaging the analysis equipment. It is expected therefore that adsorbed water, particularly in the micro-pores of the composite material may still be present and affects the obtained results and values. By contrast, Zhao *et al.* [75] report BET analysis for a PANI/C (Sigma-Aldrich Co) composite material, the type 4 BET isotherm was obtained, indicative of a mesoscopic pore structure within the macroscopic particles.

Table 4.3 BET area of the samples

Sample name	**BET area ($m^2 g^{-1}$)**
$Mg_{0.6}Ni_{0.4}O$ as-prepared	54
Al_2O_3	144
S/PANI	11
S/PANI / $Mg_{0.6}Ni_{0.4}O$	18
S/PANI/ Al_2O_3	13

The morphology of the fresh S composites is presented in **Fig. 4.13.** It can be seen that the S/PANI composite (**Fig. 4.13a**) has an agglomerated plate-like structure. The addition of metal oxides changes the morphologies of the composites (**Fig. 4.13b** and **Fig. 4.13c**), resulting in a number of irregular pores and rougher surfaces as it mainly consisted of smaller primary particles with different diameters, leading to the higher specific surface area. The formation of a mesoporous structure will favour the electrolyte penetration into the electrodes, enhancing ion transport and charge transfer. It was also observed that the Al_2O_3 addition had a smaller influence on the composite morphology than that of $Mg_{0.6}Ni_{0.4}O$. The S/PANI/Al_2O_3 composite has morphology similar to that of the bare S/PANI composite, but with a much smaller pore diameter. The porous microstructure of the pure PANI material is shown in **Fig. 4.13 d**

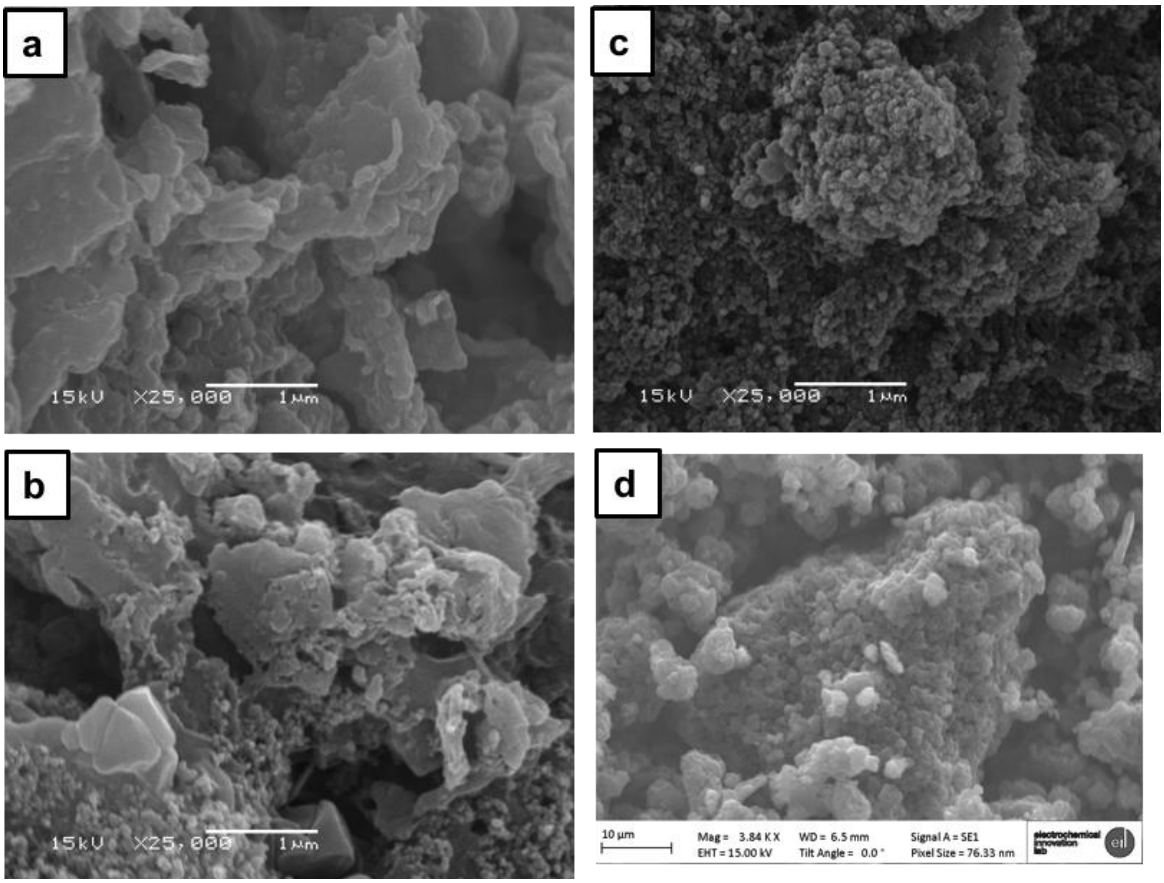

Figure 4.13 SEM images of the composites: a) S/PANI; b) S/PANI/Al_2O_3; c) S/PANI/ $Mg_{0.6}Ni_{0.4}O$; d) pure PANI

The thermogravimetric analysis (TGA) of S-composites and bare sulphur powder are shown in **Fig. 4.14**; the mass loss due to the sulphur evaporation occurs in the temperature range from 200 to 350 °C; it can be seen that the bare sulphur was burned completely at 330 °C, the composites undergo a further mass loss due to decomposition of other components in the samples, in agreement with the literature data [73]. The mass losses detected from the TGA data agree with the CHNS results on the S content in the heat treated samples. For S composites the gradual pattern of the curves demonstrated that sulphur was well trapped within the internal pores of PANI. The first mass loss at around 200 °C could also be associated with the decomposition of sulphonic acid and a part of amino – sulphur interaction. It can be seen that the thermal behaviour of the sample with $Mg_{0.6}Ni_{0.4}O$ was different from that of other composites: a second plateau from 280 to 350 °C could be observed. This

could be due to the morphology difference caused by the $Mg_{0.6}Ni_{0.4}O$ additive and formation of the internal pore space: so the sample contains two types of sulphur; one closer to the surface (easy to evaporate) and another one trapped in the internal pore space (consequently more difficult to evaporate).

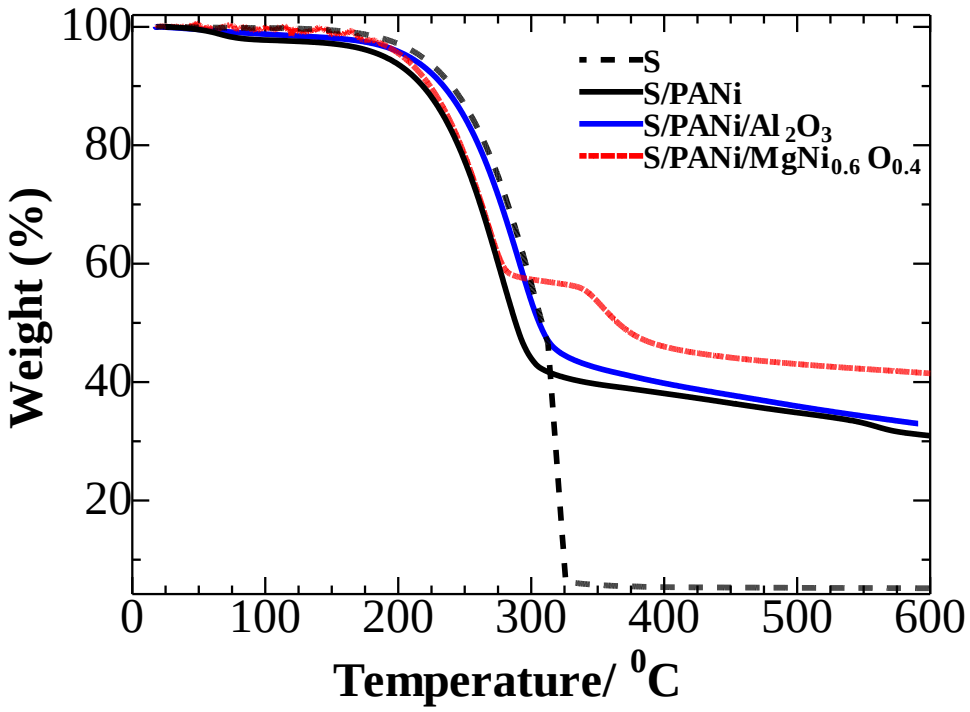

Figure 4.14 Thermogravimetric curves of S and S-composites.

Fig. 4.15 shows the SEM images of the initial (i) and cycled (ii) composite cathodes. The cycled composite cathodes were discharged/charged in the lithium half cell at 0.1C for 25 times and removed from the cell for the SEM analysis. It can be seen that significant morphology changes occur upon cycling for the S/PANI (**Fig.4.15a**) binary composite.

Although the sample with nanoparticles of Al_2O_3 had an initial structure different from that of the S/PANI system, with a highly porous morphology and relatively dense surface, upon cycling this composite underwent noticeable morphology changes and became similar to that of the S/PANI composite, with evidence of active material

agglomeration (**Fig 4.15 b)**. The active material agglomeration in the studied systems suggested its separation from the conductive agent, thus the separated non-conductive parts of the active material did not appear to take part in any further electrochemical operations, resulting in lower sulphur utilisation and a rapid capacity loss.

In contrast, the morphology of S/PANI/$Mg_{0.6}Ni_{0.4}O$ (**Fig 4.15 c)** did not change remarkably upon cycling; intact particles were bound together in the cycled cathode and retained morphology similar to that of the initial composite cathode.

The elemental mapping presented in **Fig. 4.16** shows that both $Mg_{0.6}Ni_{0.4}O$ and Al_2O_3 were uniformly mixed with sulphur and polyaniline, and no sulphur accumulation was observed on the surface.

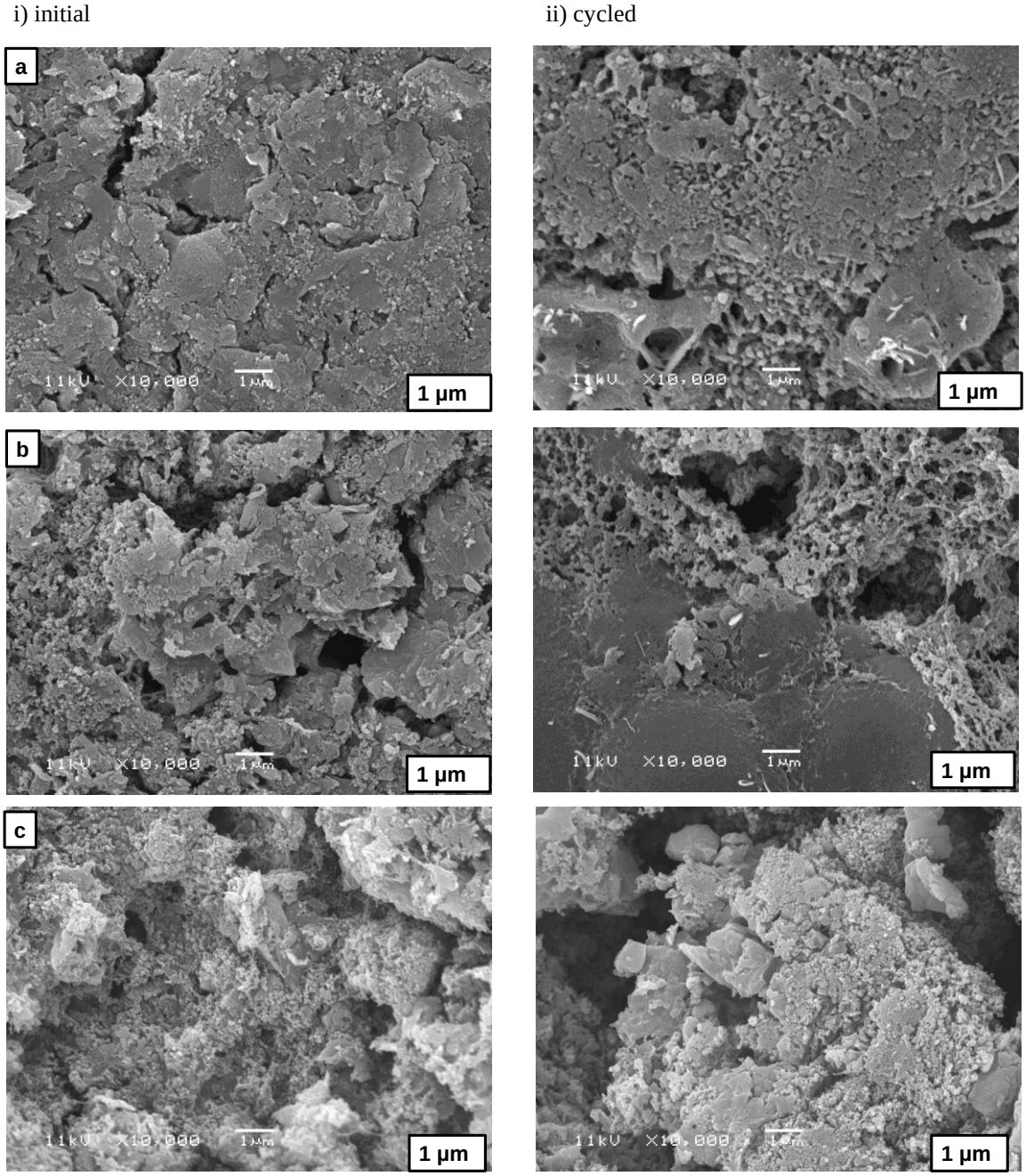

Figure 4.15 SEM images of electrodes before (i) and after 25 cycles (ii) a) S/PANI; b) S/ PANI/ Al_2O_3; c) S/PANI/ $Mg_{0.6}Ni_{0.4}O$**.**

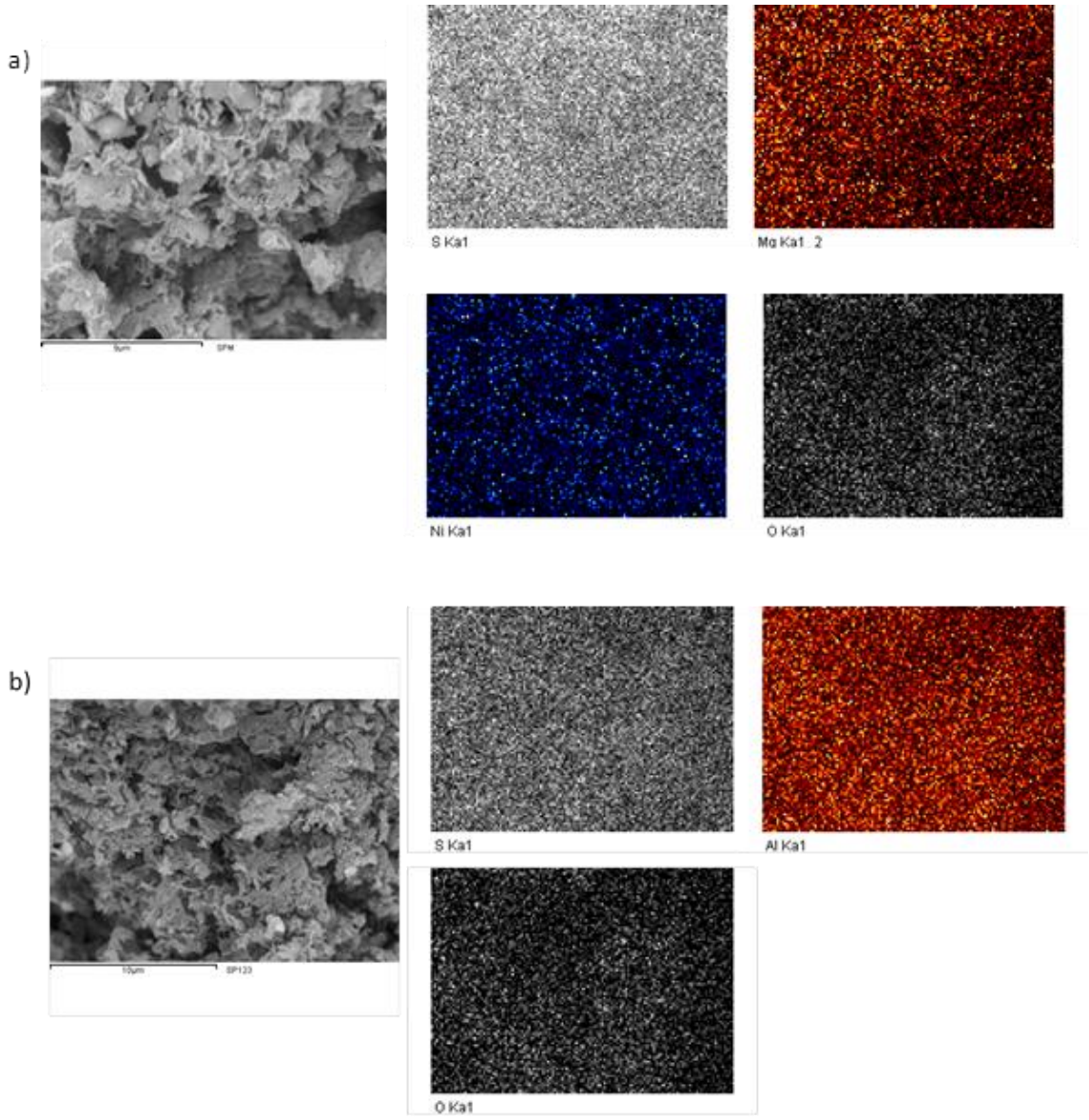

Figure 4.16. EDS elemental mapping of a) S/PANI/ $Mg_{0.6}Ni_{0.4}O$; b) S/PANI/ Al_2O_3.

4.3.3 Electrochemical properties of S – composites cells

Fig. 4.17 presents the cyclic voltammograms (CV) of a lithium-sulphur cell with the S/PANI, S/PANI/$Mg_{0.6}Ni_{0.4}O$ and S/PANI/Al_2O_3 composites cathodes, which exhibit different features of reversible operation of a Li/S cell.

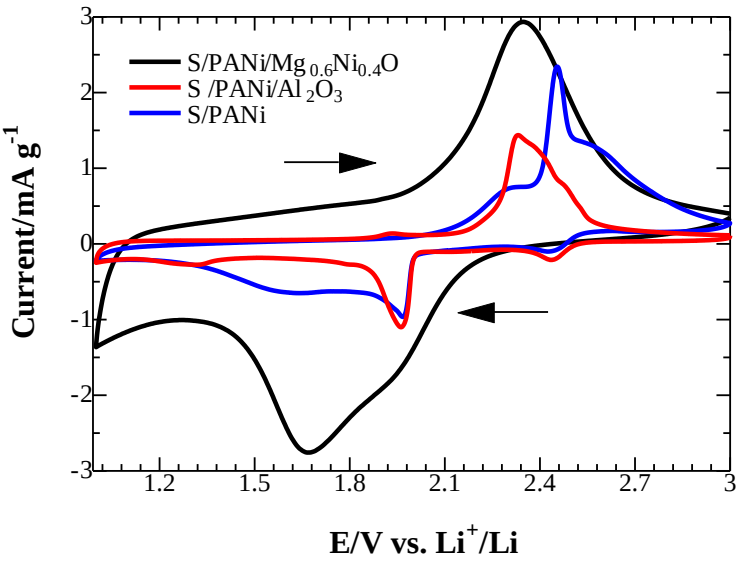

Figure 4.17 CV curves of a lithium cell with S/PANI, S/PANI/Al_2O_3 and S/PANI/$Mg_{0.6}Ni_{0.4}O$ composite cathodes; cycling rate 0.05 mV/s.

A cathodic peak for S/PANI composite located at 2.4 V was attributed to the reduction of elemental sulphur into soluble polysulphides (Li_2S_x, $2<x\leq8$), whereas the following reduction peak around 2.0 V was assigned to the further reduction of polysulphides to insoluble polysulphides (Li_2S_2, Li_2S). The peaks, observable as shoulders in the CV at ca. 2.25 V and 2.5 V are thought to be due to inter-reaction between soluble polysulphides (the poly-sulphide shuttle effect).

During the reverse sweep, the CV shows a sharp anodic peak ca. 2.35 V that was assigned to a reversible conversion of polysulphides to sulphur. Thus the electrochemical behaviour of the S/PANI composite followed typical sulphur cathode oxidation/reduction trends in lithium batteries.

Similar trends were observed in the CV curves of the S/PANI/Al_2O_3 composite, although the redox peaks of the S/PANI/Al_2O_3 cathode were slightly shifted towards each other, which could be due to the lower polarization. No additional peaks were

associated with the Al_2O_3, indicating that this additive was electrochemically inactive in the selected potential region.

Likewise, the $Mg_{0.6}Ni_{0.4}O$ additive was not electrochemically active in the selected voltage region. On the initial voltage cycle for this system there was a pronounced reduction process (**Fig. 4.18**), which was similar to that observed in previous work of some of the authors [73] for the S/PAN/$Mg_{0.6}Ni_{0.4}O$ composite. It is believed that this process is due to the side reactions and the SEI formation. It is also observed in the galvanostatic charge-discharge test, the initial discharge profile (**Fig.4.19**) is different from the subsequent profiles, suggesting that there is a pronounced polarization between the reduction and the oxidation peaks. It is also noteworthy that the high potential polarization caused the single broad cathodic and anodic peaks representing overlapped processes: between soluble, high order polysulphides (i.e. Li_2S_N, $n \geq 3$) and insoluble, low order polysulphides (Li_2S_n, $n \leq 2$), inherent to the Li/S battery [8], [180], [181].

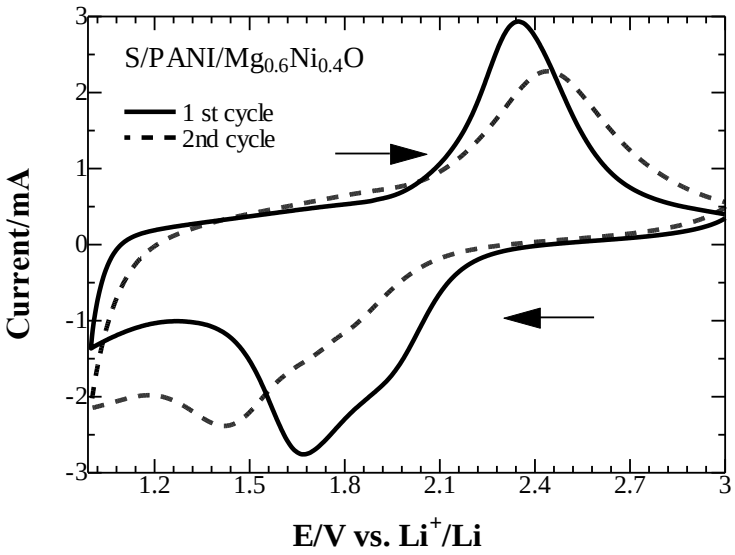

Figure 4.18 CV curves of a lithium cell with S/ PANI/ $Mg_{0.6}Ni_{0.4}O$, cycling rate 0.05 mV/s.

The CV of S/PANI/$Mg_{0.6}Ni_{0.4}O$ composite compared to S/PANI and S/PANI/ Al_2O_3 composites (**Fig. 4.17)** has a larger cathodic and anodic current density peaks, suggesting that this composite has a higher discharge capacity and active sulphur utilization (ca. 90%), which is in agreement with the charge-discharge data. These effects might also have been due to the adsorbing and catalytic activity of the $Mg_{0.6}Ni_{0.4}O$ additive. The additive acted as an adsorbent of lithium polysulphides, reducing the shuttle effect of the polysulphides, and, as shown by the SEM results, the additive prevented agglomeration of the active material and preserved the higher conductivity of the sample. The CV data complies with that previously reported in the literature [73].

Fig. 4.19 shows the initial galvanostatic charge-discharge profiles of the S/PANI, S/PANI/Al_2O_3 and S/PANI/$Mg_{0.6}Ni_{0.4}O$ composites. It can be seen that the $Mg_{0.6}Ni_{0.4}O$ and Al_2O_3 additives enhanced the sulphur utilisation in the cathode, and these composites exhibited much higher capacity than the 'bare' S/PANI system. Furthermore, the S/PANI/$Mg_{0.6}Ni_{0.4}O$ composite cathode exhibited the highest capacity among the studied systems. It should be noted that at the initial discharge the S/PANI/$Mg_{0.6}Ni_{0.4}O$ composite exhibited a continuous voltage decline which is a known phenomenon for sulphur composite cathodes and attributed to the side reactions of a solid electrolyte interphase (SEI) formation. Starting from the following cycle, this composite exhibited the typical Li/S potential profile features associated with the reversible reaction of Li and S. The short discharge plateau ca. 2.5 V is related to the formation of higher-order soluble lithium polysulphides (Li_2S_n, $n \geq 4$), followed by a plateau around 2.0 V, which reflects the transition of the polysulphides into lithium sulphide Li_2S. The kinetics of the latter reaction were slower than that of the polysulphide formation, which agrees with the literature data [168] and the CV data obtained in this work.

Another observation for the S/PANI/$Mg_{0.6}Ni_{0.4}O$ composite compared with the S/PANI and S/PANI/Al_2O_3 counterparts is a reduction of the charge and discharge voltage gap; this reflects a reduced polarization in the system, and has been reported in previous work for the S/polyacrylonitrile/$Mg_{0.6}Ni_{0.4}O$ composite [73].

Fig. 4.19d shows the composite cathodes' cyclability in a lithium sulphur half-cell. It can be seen that the S/PANI composite exhibited an initial discharge capacity of ca. 1025 mA h g^{-1} and the cell loses ca. 75% of this value within the first 20 cycles, with a stabilized discharge capacity of 300 - 400 mA h g^{-1}. For comparison, the S/PANI - NHT composite was prepared by simple wet ball milling of sulphur and PANI at room temperature with no heat treatment step (catergorised here as NHT). As seen in **Fig. 4.19 d**, the cell with S/PANI exhibited a slightly better discharge capacity than the cell with S/PANI – NHT, clearly indicating that heat treatment of S composites gave better electrochemical performance. This could be attributed to the cross-linking reactions between the conducting polymer and sulphur occurring during the heat treatment, so sulphur could have been stored in composites not only by physical adsorption but by chemical bonding, as was shown by Zhao *et al.* for S ternary composite with PANI [75].

It can be seen from **Fig. 4.19d** that the initial discharge capacity of the S/PANI/Al_2O_3 cathode is 1392 mA h g^{-1} and it retained a capacity of 612 mA h g^{-1}after 100 cycles.

The S/PANI/$Mg_{0.6}Ni_{0.4}O$ composite delivered a capacity of 1448 mA h g^{-1} at the initial cycle, and 1220 mA h g^{-1} at the following cycle, indicating a high sulphur utilization (ca. 89.5%). The cell with this cathode retained ca. 48% of the initial value after 100 cycles, exhibiting ca. 772 mA h g^{-1}.

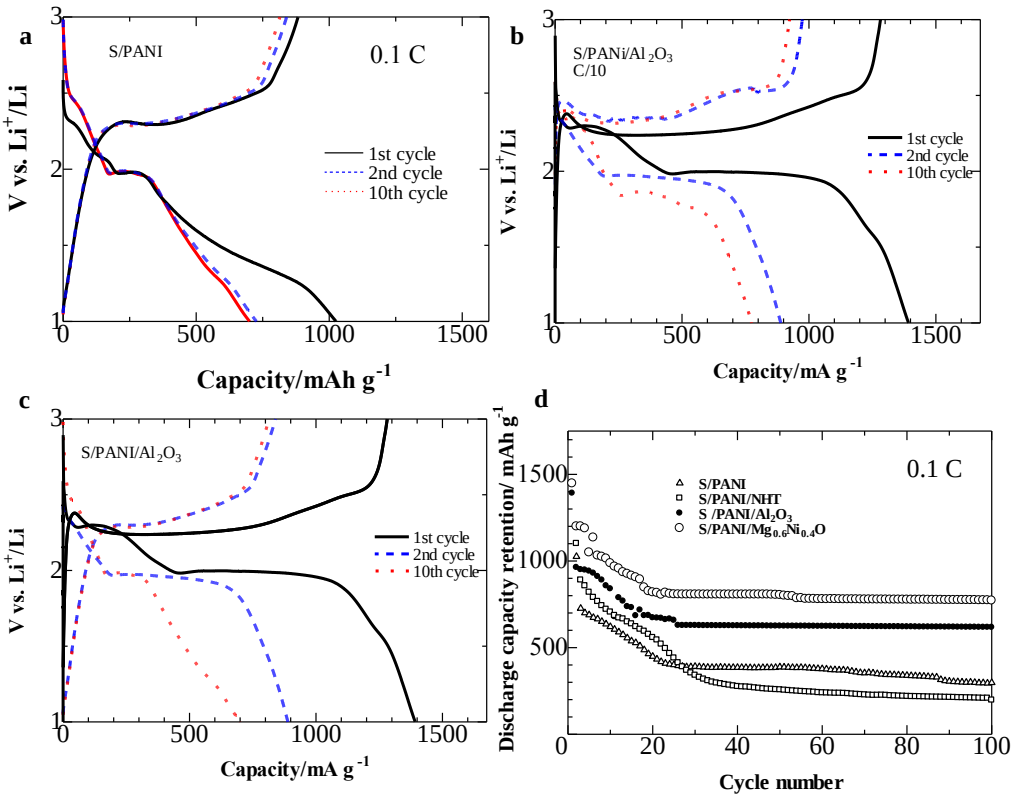

Figure 4.19. Charge-discharge profiles of lithium cells with a) S/PANI, b) S/PANI/Al_2O_3 and c) S/PANI/$Mg_{0.6}Ni_{0.4}O$ composites cathodes at 0.1 C; d) cyclability of lithium cells with S/PANI, S/PANI – NHT, S/PANI/Al_2O_3 and S/PANI/$Mg_{0.6}Ni_{0.4}O$ composites cathodes at 0.1 C.

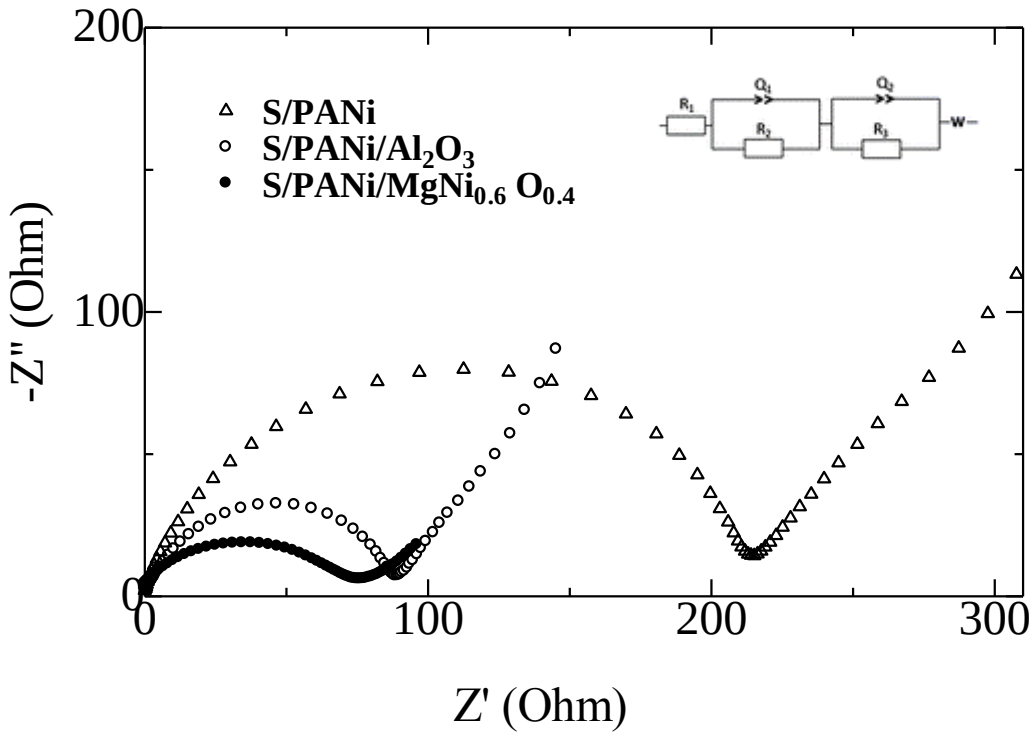

Figure 4.20 EIS impedance plots of fresh lithium cells with the S/PANI, S/PANI/Al_2O_3 and S/PANI/ $Mg_{0.6}Ni_{0.4}O$ cathodes.

Electrochemical impedance spectroscopy (EIS) was employed to investigate the effect of the $Mg_{0.6}Ni_{0.4}O$ and Al_2O_3 additives on the electrochemical behaviour of the S/PANI composite cathode. **Fig. 4.20** shows the EIS spectra of fresh lithium cells with and without the oxide additives.

Equivalent circuit analysis for each composite was conducted, and shown to be in agreement with Zhang *et al.* [50] as shown in **Fig. 4.20** in the inset. In this model, R_1 is the internal resistance of the tested battery, R_2 and R_3 represent the passivation film and charge-discharge transfer, Q_1 and Q_2 are the constant phase elements responsible for the double layer capacitance and W is the Warburg resistance related to the lithium diffusion process. The fitted impedance parameters are listed in the **Table 4.4**. It can be seen that for all the composites the Nyquist plots represent the Randles-like

equivalent circuit behaviour, and comprise of depressed semicircles in the high-to-medium frequency region due to the charge transfer resistance, followed with an inclined linear region (the so-called Warburg impedance) at low frequency due to the ion diffusion impedance within the cathode [28, 30]. It can be seen that the charge transfer semicircles (R_2 + R_3) for both composites with the metal oxide additives (98.15 Ω and 88.23 Ω respectively for S/PANI/ Al_2O_3 and S/ PANI/ $Mg_{0.6}Ni_{0.4}O$) were much smaller than the no-additive S/PANI system (208.06 Ω), with the $Mg_{0.6}Ni_{0.4}O$ composite exhibiting the lowest charge transfer resistance.

Table 4.4. The EIS simulation parameters

Cathodes	**R_1 (Ω)**	**R_2 (Ω)**	**R_3 (Ω)**	**Q_1 (μF)**	**Q_2 (μF)**	**W ($\Omega\ s^{-1/2}$)**
S/PANI	1.9	82.2	125.8	1.6	3.2	86.0
S/PANI/ Al_2O_3	2.9	56.6	41.5	5.1	2.4	58.9
S/PANI/ $Mg_{0.6}Ni_{0.4}O$	1.7	51.7	36.6	7.3	0.7	21.1

Summary

Sulphur/ conductive polymer composites were prepared by a simple wet ball milling followed by heat treatment. The use of wet ball milling and heat treatment allows the fabrication of homogenous sulphur-conductive polymer composite. The milling time and rotation speed have been optimized. Improvements on the milling processes showed that well dispersed and small sulphur particles well mixed with conducting materials improves the sulphur utilization which results in an increased battery performance in the first cycle.

For S/PAN/KB and S/PANI/KB composites it was shown that the heat treated samples have better electrochemical performance and give higher discharge capacity that could be attributed to the cross-link reactions between conducting polymer and sulphur happening during the heat treatment.

Addition of $Mg_{0.6}Ni_{0.4}O$ led to a reduction in polarization (charge transfer impedance) and improved performance. For the ternary composite S/ PANI /$Mg_{0.6}Ni_{0.4}O$/, a specific capacity of 1448 mA h g^{-1} was delivered in the initial discharge and a reversible capacity of ~900 mA h g^{-1} was obtained after 10 cycles. It was shown that the addition of $Mg_{0.6}Ni_{0.4}O$ to S/PANI composite improved the composite morphology upon cycling, kinetics and electrochemical performance of the cell. The addition of Al_2O_3 also improved the S/PANI composite's electrochemical performance, delivering an initial discharge capacity of 1392 mA h g^{-1} with the retained capacity of 612 mA h g^{-1}after 100 cycles, which was lower than for the $Mg_{0.6}Ni_{0.4}O$ additive.

The results indicate that the metal oxide nano-composite additives enhanced the electrochemical performance of the S electrodes. The composites with metal oxide additives had a more homogenous morphology compared with the initial S/PANI cathode. However, the alumina additive had a lesser enhancement effect on the sulphur/polyaniline composite compared with $Mg_{0.6}Ni_{0.4}O$ additives.

To conclude, these simple but industrially viable cell configurations can be further improved by the use of electrolyte additives or fitting the electrolyte composition. In

the next chapters the electrolyte effect as well as the processes responsible for the degradation of the battery will be studied.

CHAPTER V: OPTIMISATION OF ELECTROLYTE

Li/S cell electrochemical performances are known to be highly dependent on the electrolyte, as it has more functionality compared to LiB's electrolyte [81], [123], [127], [182]. Therefore in this chapter the fitting between S/ PANI /$Mg_{0.6}Ni_{0.4}O$ composite cathode and electrolyte was explored.

5.1 Introduction

Many of the limitations of Li/S technology are related to polysulphide solubility, consequently the electrolyte plays a critical role and its composition may control the battery performance.

As was described in chapter 2 polysulphides dissolve in conventional organic electrolytes, diffuse back and forward between the two electrodes generating a chemical shuttle, a so called "shuttle phenomenon" explained first by Mikhaylik *et al.* [183]. This phenomenon shortens the battery life as it leads to the deposition of solid species on the negative electrode lithium metal and may lead to "endless" charge process.

The shuttle phenomenon originates from the concentration gradients difference inside the cell. The high order polysulphides are formed at the positive electrode, therefore positive side has higher concentration of them, move towards the negative electrode, where their concentration is much less. On the lithium metal surface they are reduced to low order polysulphides, which in turn diffuse back to the positive in order to form the concentration gradient.

In general chemical terms, following the Le-Chatelier's principle, that means that any change in the reaction environment and any additive to the electrolyte or to the electrodes that leads to the shift in equilibria that involve intermediate products (Li polysulphides) will be reflected on the cell potential and its cyclability to the higher extent. It was shown previously in a number of publications[45], [81], [83], [123] that solvent in the electrolyte can change the reaction mechanism and thus have an effect on the cell voltage; the effects of varying the amount of electrolyte [133], salt concentration [134], [184] and viscosity also were studied as factors to influence the battery performance.

Approaches conducted on the electrolyte composition in terms of targeting polysulfide shuttle mitigation include use of additives, such as lithium nitrate ($LiNO_3$) [185], which is well known to stabilize the metallic surface; use of polysulphides in the system [135], thus applying "common-ion effect"; and recently using high salt concentration electrolytes [134], so called "solvent-in-salt" principle.

Each of these approaches has its limitations and advantages. Such as, it was shown by Zhang *et al.* [185] that while discharging to the potentials below 1.6 V the irreversible reduction of $LiNO_3$ at the carbon surface in the positive electrode occurs, however it was not observed in few studies [133], [186]. The effect of lithium polysulphides introduction to solve the dissolution of active material issue is questionable, as these polysulphides are electrochemically active as well and may introduce "extra" capacity. Increasing the salt concentration leads to the lower conductivity and high viscosity of the electrolytes as well this option is less economically viable taking into account cost of lithium salt.

The most widespread electrolytes accepted for Li/S cells by many research groups due to its solvability of polar polysulphides and appropriate ion mobility are based on binary mixtures of different ethers, mostly 1,3-dioxolane (DOL) and tetraethylene glycol dimethylether (tetraglyme, TEGDME).

Therefore, here we will compare the impact of different salt concentration of the electrolytes on the example of single TEGDME with LiTFSI electrolyte (the

concentration were varied from 1M to 3M); introduction of 0.3 M $LiNO_3$ additive and use of DOL as co-solvent in high salt concentration electrolyte on the overall Li/S cell performance. DOL was selected a co-solvent as it is known that it has lower viscosity, thus the effect of viscosity is taken into account as well. This will help to find the optimal composition and fitting between positive electrode and electrolyte. For this purpose here we used S/ PANI /$Mg_{0.6}Ni_{0.4}O$ composite cathode, in this work it showed the best performance as well as it is known that $Mg_{0.6}Ni_{0.4}O$ has polar surface and can absorb lithium polysulphides.

5.2 Experimental

5.2.1 Electrolytes preparation

Electrolyte solutions were prepared in a glove-box filled with argon; the residual water content was measured by using a Metrohom Karl–Fisher titrator and was found to be below 20 ppm. Lithium bis(trifluoromethane sulfonyl imide (LiTFSI) was stirred for 8 hours in tetra(ethylene glycol) dimethyl ether (TEGDME) in the glove box filled with Argon. **Table 5.1** lists all the electrolyte compositions used in this work.

Table 5.1 List of electrolytes

Label	**Electrolyte**
E1	1 M LiTFSI in TEGDME
E2	3 M LiTFSI in TEGDME
E3	3 M LiTFSI in TEGDME:DOL (1:1)
E4	1M LiTFSI with 0.3M $LiNO_3$ in TEGDME

In **Table 5.2** the physical characteristics of TEGDME and DOL are summarized.

Table 5.2 List of solvents and their physical properties [187]:

Solvent	Molecular weight	Density, g/cm^3	Normal boiling point, C	Normal melting point, C	Viscosity at 25 ºC	Dielectric constant
DOL	74.08	1.060	78	-95	0.6	7.1
TEGDME	222.28	1.009	275	-30	4.05	7.9

TEGDME has a glyme structure, low dielectric constant and high donor number. DOL also has low dielectric constant, but lower viscosity compared to TEGDME and lower solvation [187]. Due to these properties DOL is mostly used as a co-solvent, so here we used DOL as a co-solvent, mainly to see the difference with the viscosity, although we should also note different solvation properties of DOL which can also affect the system.

5.2.2 Cell assembly and measurements

The electrodes were prepared as described in chapters 2 and 4; active material is S/PANI/$Mg_{0.6}Ni_{0.4}O$, as it demonstrated the best performance in this work. For a fair comparison the electrodes examined were of equal mass.

Electrochemical tests of the S/composites were performed using the coin-type cells (CR2032) with lithium metal foil as the counter electrode. CR2032 coin-type cells were assembled in a glove box filled with high purity argon (99.9995% purity) by sandwiching a polypropylene separator (Celgard, MTI Inc.) between the composite cathode and lithium anode and using a relevant electrolyte. Symmetric cells were used to study solely the contribution of electrolyte and its interaction with lithium, and assembled also in the glove box by sandwiching a polypropylene separator (Celgard, MTI Inc.) soaked in the electrolyte between two lithium metal discs.

Galvanostatic charge/discharge and cyclic voltammetry (CV) were used to test the electrochemical properties of the batteries with different electrolyte composition.

CV was conducted using a potentiostat (Gamry, Reference 3000) at a scan rate of 0.1 mV s^{-1} between 1.5 and 3 V *vs.* Li^+/Li. The cells were cycled galvanostatically using a multichannel battery tester (BT-2000, Arbin), in the range 1.5 to 3 V *vs.* Li^+/Li at 0.2 C.

Impedance measurements were conducted by means of potentiostat (Gamry, Reference 3000) and potensistat/galvanostat (VMP3, Biologic). The frequency of AC impedance was varied from 0.1 Hz to 1 MHz with applied voltage amplitude of 5 mV. Impedance data analysis was performed on EC-Lab 10.17 software (Biologic). Applied currents and specific capacities were calculated on the basis of the mass of S in the cathode. All electrochemical measurements were performed at room temperatures.

5.3 Results and discussion

5.3.1 Battery performance

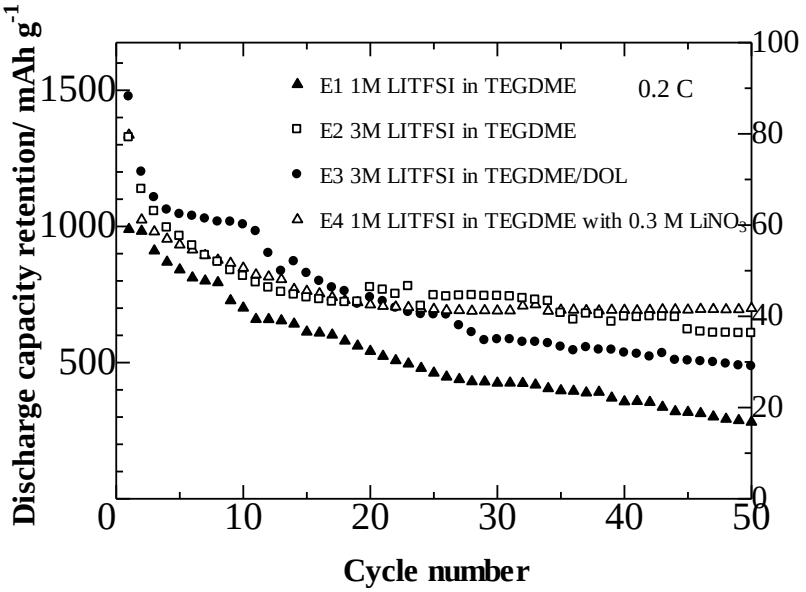

Figure 5.1 Comparison of cycle lives of S/PANI/$Mg_{0.6}Ni_{0.4}O$ electrode with different electrolytes

In **Fig. 5.1** the comparison of batteries cycle life with different electrolytes is presented, the chosen c-rate is 0.2C. At least three cells with the same electrolyte were tested to justify the results presented.

The use of a co-solvent DOL was found to improve the first initial discharge characteristics of Li/S cell, the sample E3 with 3M LiTFSI in DOL/TEGDME demonstrated the highest initial discharge capacity of 1476 mA h g^{-1}, probably resulting from the lowering viscosity of the electrolyte compared to TEGDME based electrolyte and higher availability of lithium ions in solution. However, the capacity fading was higher in comparison with the sample E2 with single TEGDME solvent and the same 3M salt concentration after about 20 cycles.

Capacity fading was observed for all the samples and a comparatively better performance resulted from the sample E4 with $LiNO_3$ additive. The addition of 0.3 M $LiNO_3$ improved the initial capacity as well; it was enhanced to 1214 mA h g^{-1} compared to 989 mA h g^{-1} reached by the bare sample E1. This complies with previous reports on $LiNO_3$ additive use [183], [185], [188].

Generally, the high lithium salt concentrated electrolytes enhanced the battery performance and cycle stability. The discharge capacity of 552 mA h g^{-1} for the sample E2 and 482 mA h g^{-1} for the sample E3 after 50 cycles were retained, whereas the discharge capacity for 1M LiTFSI quickly discharged to 245 mA h g^{-1}. It could be concluded that increasing the concentration leads to a better performance of the battery. The sample with electrolyte E1 (1M LiTFSI in TEGDME) has the lowest performance compared to other cells.

To investigate the electrochemical reaction process in the samples and the effect of changing electrolyte parameters (concentration, co-solvent and $LiNO_3$ additive) the measurement of impedance spectroscopy during cycles was conducted. The Nyquist plots of the samples are presented in the **Fig. 5.2** illustrating their impedance trends upon cycling.

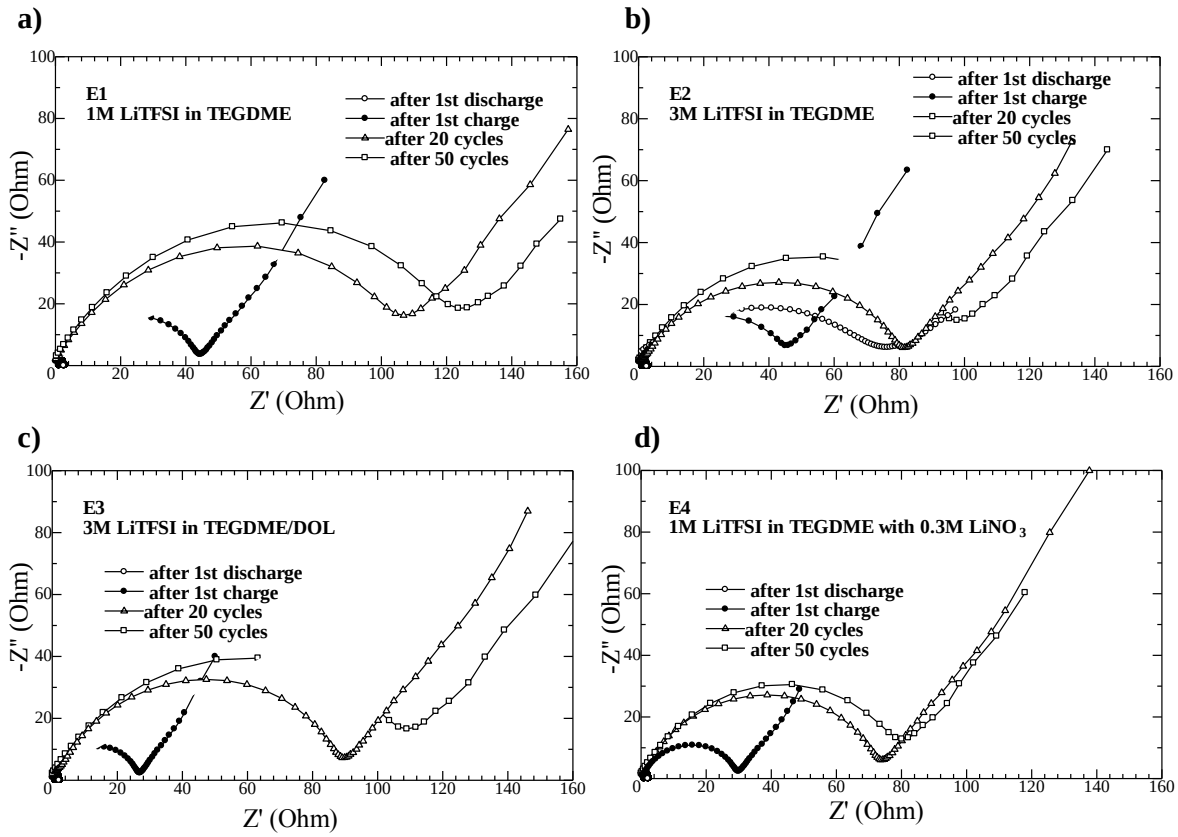

Figure 5.2 EIS plots of S/PANI/$Mg_{0.6}Ni_{0.4}O$ electrode with different electrolytes (after 1st. 20th, and 50th cycles) from top left a) 1M TEGDME, E1; b) 3M TEGDME, E2; c), E3; 3M DOL/TEGDME d) E4, 1M TEGDME with 0.3M $LiNO_3$

All the plots present a compressed semicircular loop in the high to low frequency range, the diameter of the loop corresponds to the charge-transfer resistance and a straight line in the low frequency range relates to Warburg diffusion process.

The lower charge transfer resistance (R_t) compared to the sample with single TEGDME sample E1 was found in all other samples, which is in compliance with cycling results and performance in the first cycles.

It can be seen that the EIS spectra for the samples changes upon cycling with a different pattern. The magnitude of the semicircles increases with increasing cycling

number that is in connection to battery degradation upon cycling. However the magnitude of this increase is different. To explore this relationship the Nyquist plots were fitted by using the circuit model illustrated in the **Fig. 5.3** and all fitted elements are presented in **Table 5.3.**

The total impedance of the sample with E1 electrolyte is larger compared to other samples that corresponds to the battery charge-discharge data. The capacity fade happens rapidly in the sample with E1 electrolyte and the gap between 1^{st} and 20^{th} cycles impedance plots is relatively larger compared to the samples with higher concentration and $LiNO_3$ additive as could be seen from the **Fig.5.4.**

The addition of $LiNO_3$ and introduction of DOL reduces the R_t as could be seen from the impedance plots after 1^{st} charge. However as the cycle number increases the change of R_t is varying. The best stability is shown by the sample E4 with $LiNO_3$, that is in agreement with the cyclability data. Whereas the R_t values of the sample E3 with the mixed electrolyte demonstrates that the system is not stable and although it has lower resistance compared to TEGDME alone the cycle properties were better with TEGDME alone as a solvent.

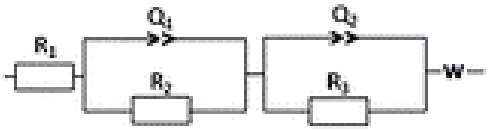

Figure 5.3 Electric circuit model used

Table 5.3 Fitted values for the equivalent circuit elements in **Fig. 5.3** by simulation of impedance spectra in **Fig. 5.2**

Electrolyte	**1 cycle**					
	R_1 (Ω) $\times 10^2$	**R_2 (Ω)**	**R_3 (Ω)**	**Q_2 (μF)**	**Q_3 (μF)**	**W ($\Omega\ s^{-1/2}$)**
E1	65	30	12	8.1×10^{-5}	5.5×10^{-5}	3
E2	95	41	10	5.1	2.4	22
E3	33	21	4	8.7×10^{-4}	7.5×10^{-4}	3
E4	27	21	7	1.5×10^{-3}	9.;8×10^{-4}	2

Electrolyte	**20 cycle**					
	R_1 (Ω) $\times 10^2$	**R_2 (Ω)**	**R_3 (Ω)**	**Q_2 (μF) $\times 10^3$**	**Q_3 (μF) $\times 10^{-4}$**	**W ($\Omega\ s^{-1/2}$)**
E1	7.4	57	38	8.1	2	6
E2	80	41	29	0.3	0.2	5
E3	96	61	22	1.1	4	5.5
E4	9	28	13	0.1	3	4

Electrolyte	**50 cycles**					
	R_1 (Ω) $\times 10^2$	**R_2 (Ω)**	**R_3 (Ω)**	**Q_2 (μF) $\times 10^3$**	**Q_3 (μF) $\times 10^4$**	**W ($\Omega\ s^{-1/2}$)**
E1	30	86	26	8.9	2.7	3.5
E2	87	64	23	3.1	0.1	6
E3	9	83	15	2.9	8.9	6
E4	0.3	62	13	2.1	2.7	4

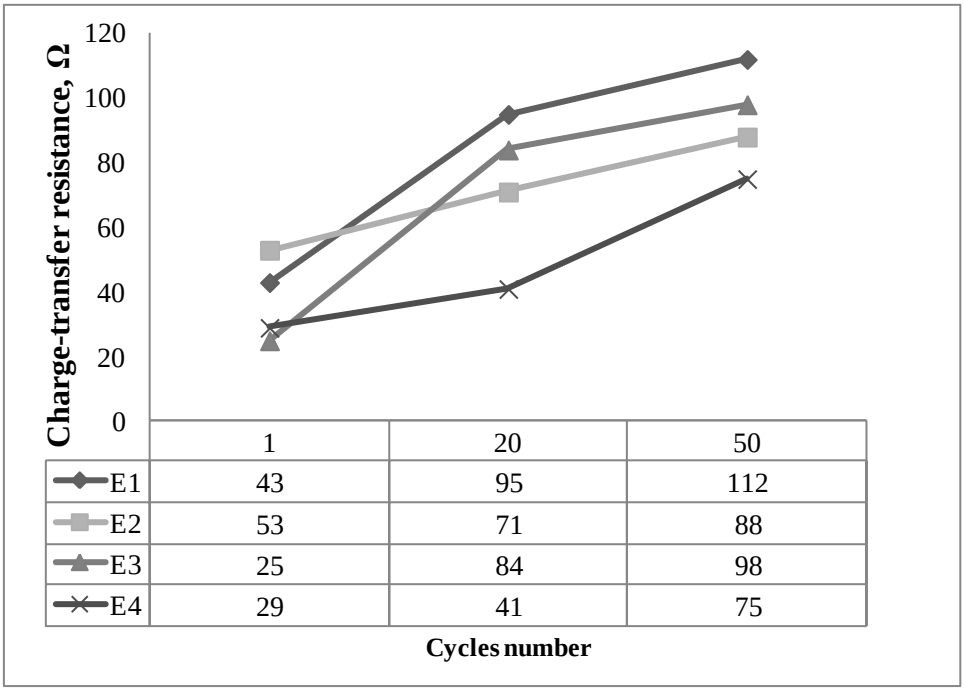

	1	20	50
E1	43	95	112
E2	53	71	88
E3	25	84	98
E4	29	41	75

E1 - 1 M LiTFSI in TEGDME
E2 - 3 M LiTFSI in TEGDME
E3 - 3 M LiTFSI in TEGDME:DOL
E4 -1 M LiTFSI with 0.3M$LiNO_3$ in TEGDME

Figure 5.4 The dependence of charge transfer resistance (R_t) on cycling

The initial three charge/discharge curves of the S/PANI/ $Mg_{0.6}Ni_{0.4}O$ composite with different electrolytes are shown in the **Fig. 5.5.** There are two typical discharge plateaus and the initial cycle is slightly different with the hysteretic slope which can be assigned to the initial reduction of S in S/PANI composite due to the chemical interaction between C-S bonds.

The increase of lithium salt concentrations has an effect on the appearance of the first plateau, it is shorter compared to the samples with 1M LITFSI. The potential polarization is also between charge potential plateau and the second discharge plateau is increasing with the increase of concentration, but nearly stays the same with the addition of $LiNO_3$.

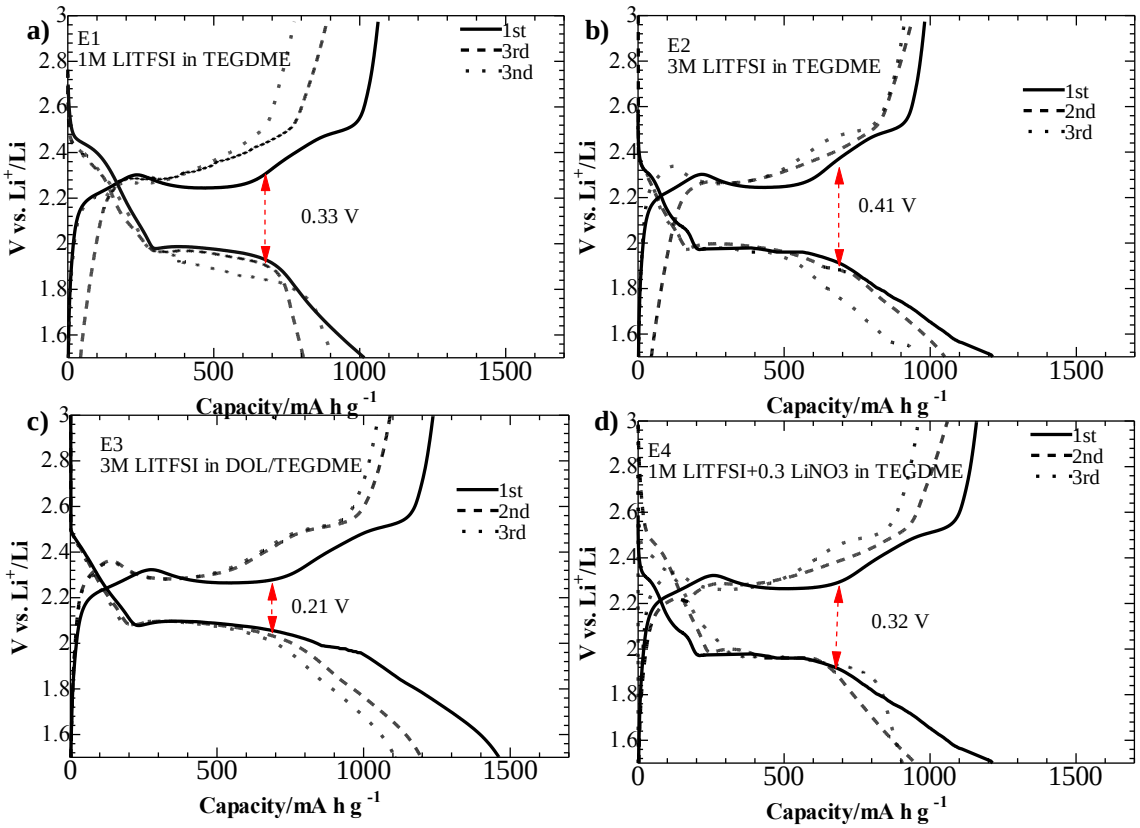

Figure 5.5 The charge-discharge profiles of samples from top left a) 1M TEGDME, E1; b) 3M TEGDME, E2; c) 3M DOL/TEGDME, E3; d) 1M TEGDME with 0.3M $LiNO_3$ E4..

It could be noticed that with addition of DOL, and thus changing the solvation environment, the second plateau on the discharge profile is at higher voltage of 2.05 V compared to the samples with TEGDME solvent with the second plateau at 1.95V. The distance between the charge and the second discharge plateau is shorter. That could be attributed to the lowering the viscosity and thus better wetting of the electrodes.

Typical cyclic voltammogramms of the prepared cells with different electrolytes are shown in the **Fig. 5.6.** It is found from CVs that there are two cathodic peak potentials of 2.4 and 1.8 in the electrolyte with 1 M LiTFSI due to the two step reduction of sulphur. With increasing the lithium salt concentration in the electrolytes the cathodic

peak potentials are gradually shifted as shown in the **Fig. 5.6.** In analogy with charge-discharge profile it could be seen that CV profile for DOL/TEGDME solvent is different shape and shifted, although has the same number of peaks. Two cathodic peaks for DOL/TEGDME solvent are at 2V and 2.3V, whereas the cathodic peaks for TEGDME solvent are at 1.8V and 2.35-2.4 V.

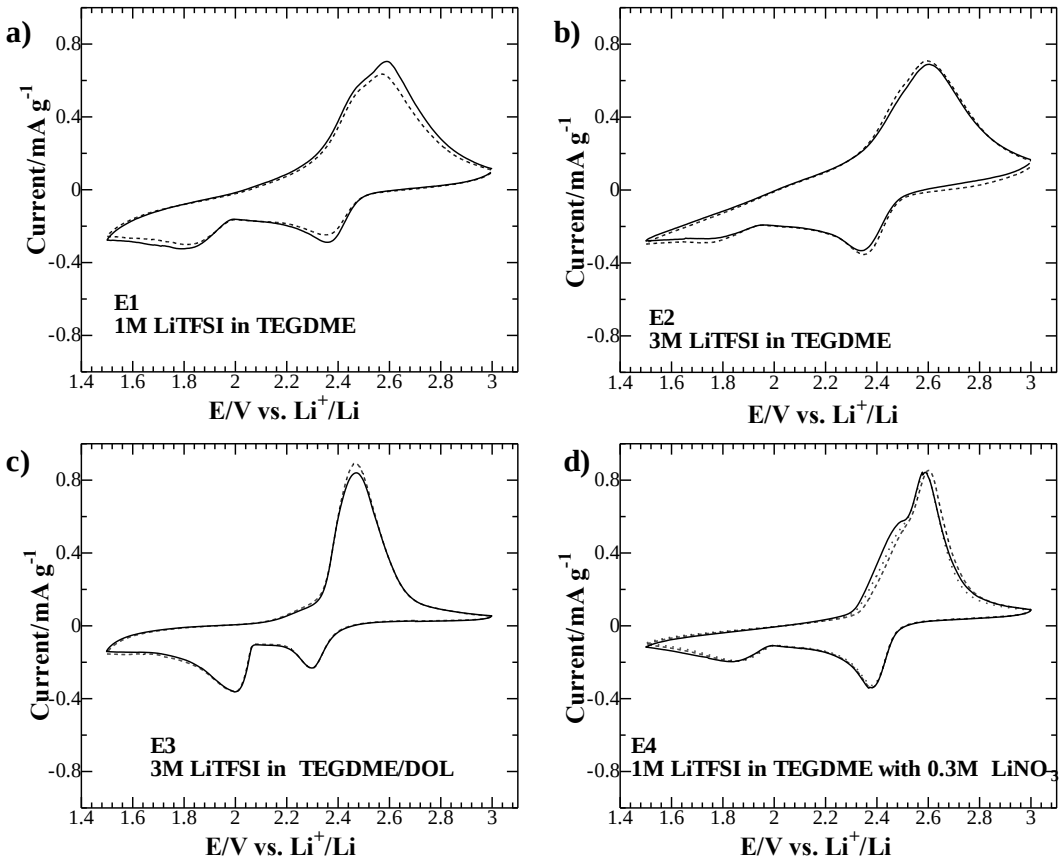

Figure 5.6 Cyclic voltammograms of S/PANI/ $Mg_{0.6}Ni_{0.4}O$ electrode with different electrolytes (2nd cycle and 3rd cycles) from top left a) 1M TEGDME, E1; b) 3M TEGDME, E2; c) 3M DOL/TEGDME, E3; d) 1M TEGDME with 0.3M $LiNO_3$ E4.

To further investigate these trends EIS was performed on symmetrical coin cells. It is known the solid electrolyte interphase (SEI) layer forms immediately after the contact between Li electrode and electrolyte caused by Li metal high activity. One way to study the SEI formation caused by the contact of Li metal with electrolyte is to apply EIS on the symmetric lithium metal/electrolyte/lithium metal cells, this method have

been widely used to study the formation of a SEI on lithium anodes. Additionally the ionic conductivity of the electrolytes at room temperature was determined. The obtained EIS spectra are shown in **Fig. 5.7.**

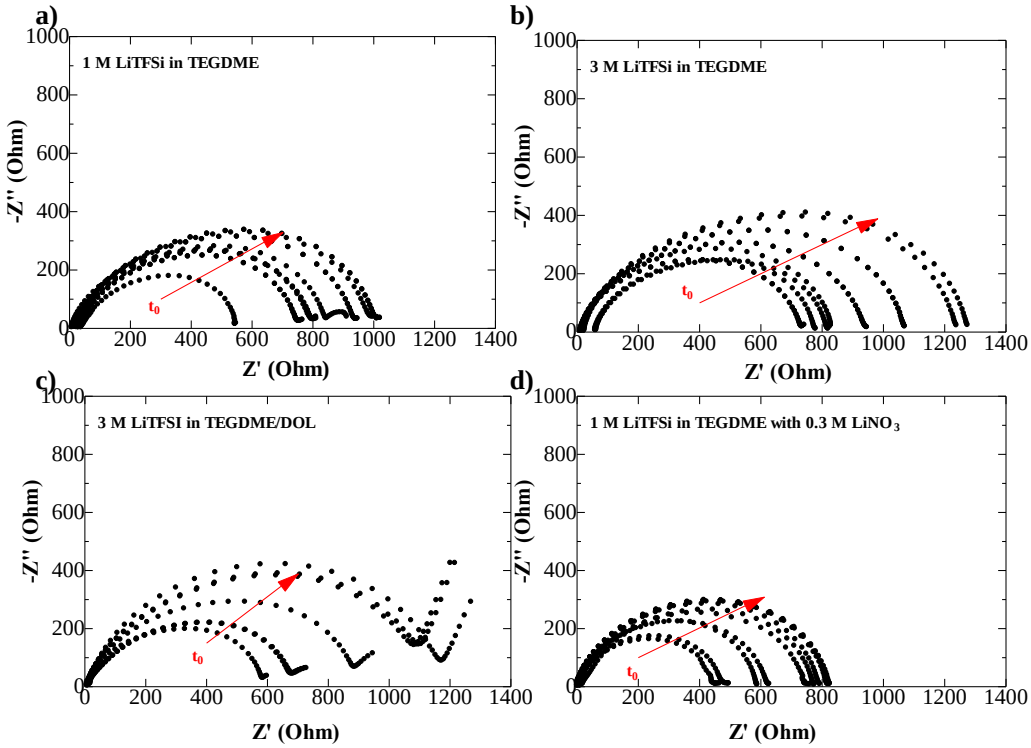

Figure 5.7 EIS spectra of symmetric Li/Li cell stored for 10 days and measured each day. from top left a) 1M TEGDME, E1; b) 3M TEGDME, E2; c) 3M DOL/TEGDME, E3; d) 1M TEGDME with 0.3M $LiNO_3$ E4.

The interfacial resistance on fresh is relatively small for all traditional electrolytes; however the resistance increases slowly during the subsequent storage which indicates that the SEI layer is not stable and takes time to form it. Thus the stability of the system is indicated by the changes in the EIS Nyquist plots. Therefore the increasing resistance suggest that there is a continuous reaction between the lithium metal electrode and the electrolyte components which leads to unstable interface. The EIS spectra for the sample E4 with $LiNO_3$ additive has less changed over 10 days storage compared to other samples. That indicated the reduction of resistance on lithium

anode with the addition of $LiNO_3$. As expected from the literature the addition of $LiNO_3$ leads to a stable SEI layer, whereas increasing lithium salt concentration does not have the same effect and even leads to the less stable EIS spectra compared to bare 1M LiTFSI in TEGDME electrolyte.

As it could be seen from the ionic conductivity data (**Table 5.4**) with the increase of lithium salt concentration the viscosity increases as well, but ionic conductivity decreases. It is expected that the mobility of lithium ions decreased as well, as the solution is more viscous and thus the solvation properties are different. But at the same time highly concentrated electrolytes are lithium ions rich and the reaction is preferably moving towards the formation of the end products. Thus, high viscosity limits the ion transport processes but reduces the diffusion processes as well.

Table 5.4 Ionic conductivity of the electrolytes

	Electrolyte	**Conductivity (mS cm^{-1})**
E1	1 M LiTFSI in TEGDME	8.2
E2	3 M LiTFSI in TEGDME	3.96
E3	3 M LiTFSI in TEGDME:DOL (1:1 mL)	6.52
E4	1M LiTFSI with 0.3M $LiNO_3$ in TEGDME	11.3

Summary

Choosing a right electrolyte is important for successful lithium sulphur battery. Ethereal electrolytes are the most common Li/S battery electrolytes, as they have high solubility of polysulphides. In the liquid electrolytes the solubility of intermediate products – polysulphides is an inevitable process and possibly suppress the growth of Li dendrite as well. However it can also cause internal polysulphide shuttle and endless charge process.

There are two mechanisms that have been considered here: increasing the salt concentration and addition of lithium nitrate.

The nearly saturated LiTFSI make the intermediate products dissolution process difficult and thus helps to avoid the shuttle mechanism. Thus the high concentration lithium salt has a great impact on the cycle stability by suppressing the shuttle mechanism. In comparison the discharge capacity is quickly decreased for the composite in the electrolyte with 1M LiTFSI, whereas increasing the concentration the cycle stability was optimised. However, viscosity of the solvent also contributes to the stability of the system over cycling. It was observed that the cycle properties were better with TEGDME alone as a solvent, rather than with DOL/TEGDME mixed solution. In general, the high concentrated electrolytes have better stability over cycling, although do not improve the initial capacity of the cell. This behaviour could be attributed to the improved lithium ion availability and the decrease of solubility, thus preventing the shuttle mechanism.

Indeed, the addition of $LiNO_3$ improve the cell performance with the different mechanism with the formation of strong EIS, which can be regarded as a border between the liquid electrolyte and electrode that controls intercalation, diffusion and the charge transfer reaction and could be attributed to the reduction of interfacial resistance on lithium anode. Although a detailed description and discussion of the characteristics and performance of $LiNO_3$ additive is beyond the scope of this study, it

could be concluded that it is beneficial to use this additive over the increasing of lithium salt concentration.

The dissolution of polysulphides plays an important role in the battery kinetics' and could be considered as essential part of Li/S battery operation. The developed cathode demonstrated high capacity and ability to retain the morphology upon cycling, however with the variation of electrolyte content the battery operation could be improved further.

CHAPTER VI: TOMOGRAPHY STUDIES

In the previous chapters, Li/S battery optimisation was approached by changing the cathode structure and the electrolyte content. In this chapter we attempt to understand the Li/S battery degradation mechanism by utilizing lab based X-ray micro-tomographic imaging to non-destructively examine microstructural changes in lithium/sulphur battery before and after lithiation.

6.1 Introduction

There are a number of issues that limit the application of conventional characterization techniques such as the low melting point of sulphur, polysulphide instability in air and the change of physical state of the S electrode. The Li/S battery has been widely studied by various *ex-situ* techniques that have helped to broaden understanding of its chemistry and processes, but have also brought some controversies, particularly as most of the previously mentioned issues appear due to a high reactivity of lithium polysulphides in the air. Moreover Li_2S hydrolyses in air producing H_2S.

Therefore, *in-situ* methods are preferable for studies of the Li/S battery. Although *in-situ* and *operando* methods have been widely applied in the study of lithium ion batteries, there is a limited application in Li/S system and often these methods need to be modified and redesigned to account for the S electrode specifics. The most common *in-situ* techniques applied in Li/S system are: XRD characterization of sulphur cathodes [150],

[151], [158], *in-situ* Raman [159]; *in-operando* UV-vis [160] which provides chemical and electrochemical behaviour of Li/S battery, they are also one or two-dimensional.

X-ray computed tomography (CT) is a non-destructive technique that has the ability to reveal essential information across the thickness of the electrode to explore the evolution of the Li/S battery electrode microstructure in three dimensions, over time.

In this work we adopt a 3D X-ray imaging approach to examine the electrode both *ex-situ* at nano-scale, and *in-situ* at the micro-scale in order to study the fundamental changes in S electrode with cycling. The *in-situ* X-ray tomography provides an advantage of being a non-destructive and powerful technique for cell diagnostic and new materials design. During these analyses, the cell was not disrupted, thus the change of all layers and active material loss upon cycling was observed and quantified.

6.2 Experimental procedure

6.2.1 Design considerations for *in-situ* X ray tomography

An *in-situ* characterisation of a battery requires a cell that enables analysis without its disassembly. The design of such cell depends on the particular battery technology to be considered (in this case Li/S battery), the type of X-ray sources and the imaging mode. For the cell components selection the following factors have to be considered:

- The X-ray must be transmitted into the material to be analysed, therefore a suitable material should be X-ray transparent;
- The material of the cell components should be not only mechanically, but chemically stable;
- The cell should have electrical contact for both electrodes;
- The cell has to be hermetically sealed due to the high reactivity of Li and polysulphides mainly with water and air;

- The cell should be easy to fabricate in the glove box and electrodes and separator could be easily placed accordingly.

As described in chapter 3 for this purpose a modified PFA Swagelok© cell developed by Taiwo *et al.* in [190] was used.

The cell was placed inside a Zeiss Xradia Versa 520 micro-CT instrument and positioned on the sample stage as shown in **Fig. 6.1**. **Fig.6.2** shows a 3D tomographic reconstruction without any image processing, recorded prior to any electrochemical test and taken within the *in-situ* cell. The full electrode fits into the field of view to allow tracking of all battery components: electrodes and separator.

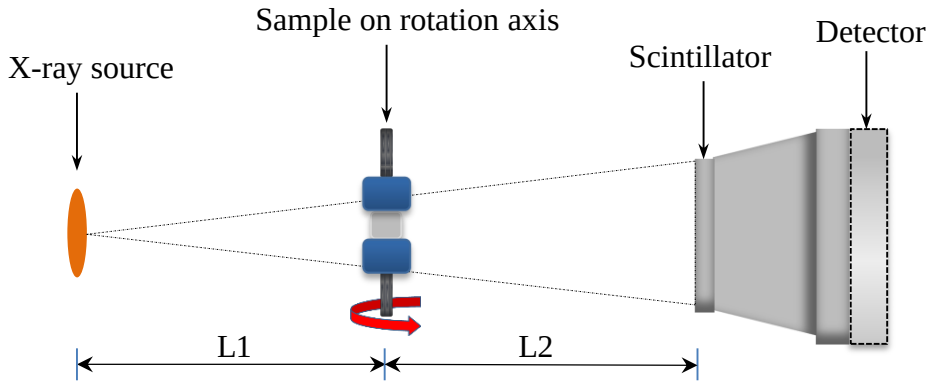

Figure 6.1 Configuration of the *in-situ* X-ray tomography experimental set–up. The *in-situ* cell is mounted on a motorized goniometric head.

L1 is the source to sample distance; L2 is the sample to detector distance

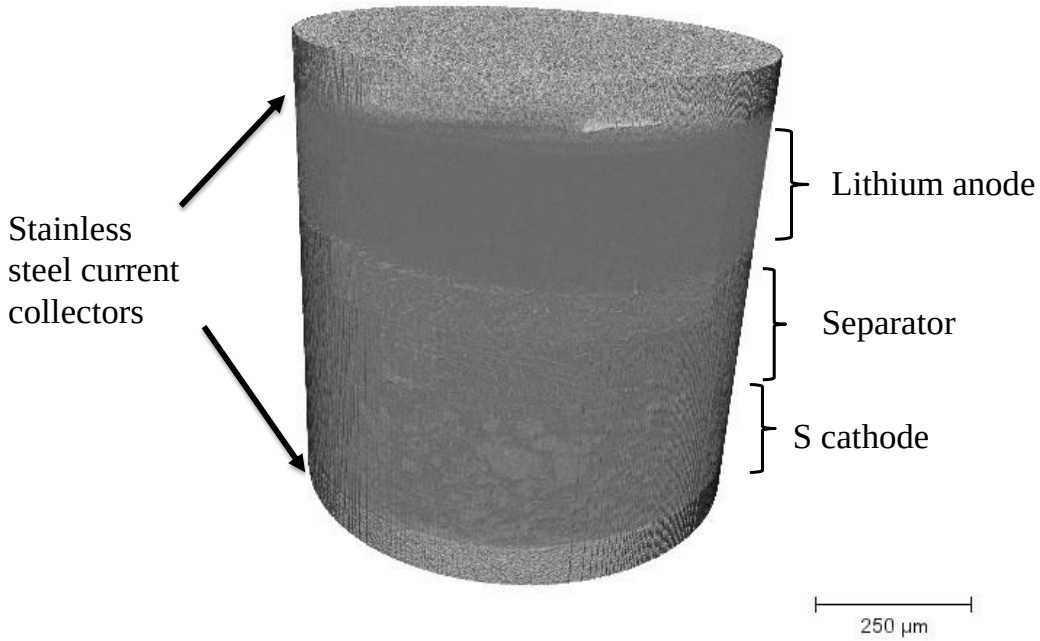

Figure 6.2 3D image of fresh Li/S cell taken within the *in-situ* cell with no image processing.

The batteries with modified 1/8" PFA Swagelok© unions were assembled in a glove box filled with high purity argon (99.9995% purity) with O_2 and H_2O levels kept at below <0.5 ppm.

The glass fibre separator (Whatman GF/D) punched to 1/8" was placed on top of the cathode and soaked with 1M LiTFSI in TEGDME electrolyte. The lithium metal foil punched slightly less than 1/8" to avoid short circuit was then placed on the separator and then finally closed with plastic screws.

Prior to assembly in the PFA cell, the electrodes were also scanned *ex-situ* (**Fig. 6.3 c, d**) and the resulting 3-D reconstructions of the composite electrode materials were compared to those generated from the *in-situ* tomography scans (**Fig 6.3 a, b**). The sample scanned

ex-situ was not under compression during imaging and not in contact with electrolyte. S particles can be clearly identified due to differences in X-ray attenuation coefficients.

Several samples within the *in-situ* setup were scanned in this study. The list of samples is given below in the **Table 6.1**, the electrode formulation is the same and described in the subsequent section.

Table 6.1 Summary of scans performed on S/C electrode in Swagelok© Cell within the *in-situ* set-up

	Sample description	**Scans performed**
Sample A	Swagelok© Cell with S electrode of ca.250 (10^{-6} m) thickness	1. Uncycled, fresh, 2. After full discharge.
Sample B	Swagelok© Cell with S electrode of ca.250 (10^{-6} m) thickness	1. Uncycled, fresh; 2. After 2 cycles.
Sample C	Swagelok© Cell with S electrode of ca.250 (10^{-6} m) thickness	1. Uncycled, fresh; 2. After 2 cycles; 3. After 10 cycles.

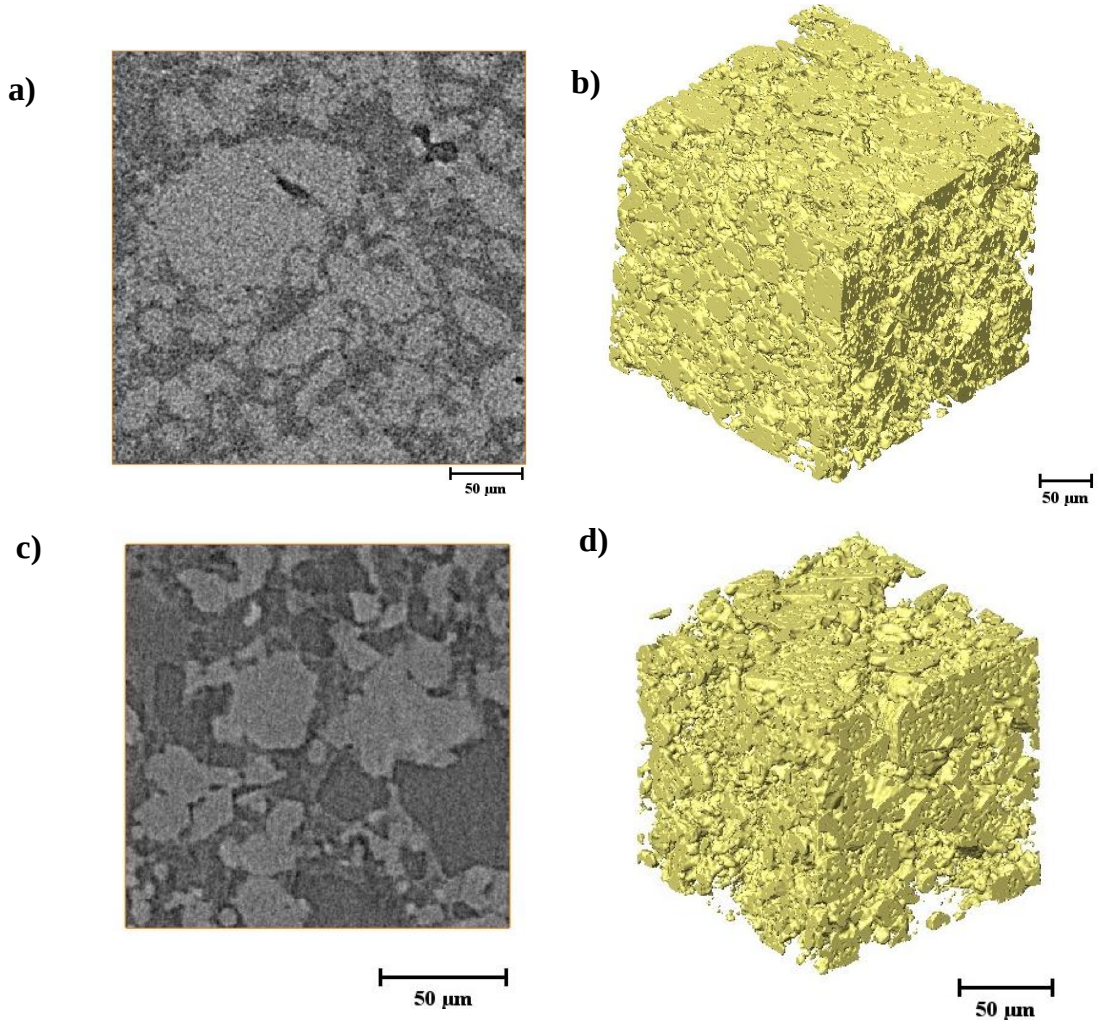

Figure 6.3 a) A reconstructed slice from a tomographic image of the S/C cathode made within the *in-situ* set up; b) Volume rendering of the cropped region following segmentation within the *in-situ* set up; c) A reconstructed slice from a tomographic image of the S/C cathode made *ex-situ*; d) Volume rendering of the cropped region following segmentation made *ex-situ.* All images from micro-XCT dataset.

6.2.2 Electrode preparation

In this baseline study elemental mixture of S and carbon black composite was employed as an active material in Li/S batteries for all micro-CT samples.

S, conductive carbon black (Super C65, Timcal) and polyvinylidene fluoride binder (PVDF) were mixed using an agate pestle and mortar in a 8:1:1 weight ratio with NMP to form a slurry that was then cast on 1/8" stainless steel pins and dried in a vacuum oven overnight. The resulting thickness of the S-cathodes were between 200-250 μm, thus the sulphur loading is >10 mg/cm^2.

In the preliminary studies fresh sulphur electrodes based on elemental S and S/PANI/ $Mg_{0.6}Ni_{0.4}O$ fabricated in this work were scanned *ex-situ* in Versa directly on stainless steel current collector to adjust experiment settings and to compare results with *in-situ* set-up, however the particle size of S/PANI/ $Mg_{0.6}Ni_{0.4}O$ composite is beyond the resolution of the X-ray micro-tomography instrument. Therefore it was decided to continue the micro-CT study with elemental S (S/C) electrode.

6.2.3 Electrochemical characterization

Electrochemical characterization was performed on the S-composite used for the modified Li/S Swagelok© cells by charge discharge cycling in a galvanostat/potentiostat (Interface 1000, Gamry Instruments) with constant current densities of 0.10 mA/cm^2 . Potentiostatic electrochemical impedance spectroscopy (EIS) was also carried out in a galvanostat/potentiostat (Interface 1000, Gamry Instruments) on uncycled Li/S batteries before and after tomography, with an AC voltage of 20 mV r.m.s in the range of frequencies of 1 Hz and 1 MHz.

6.2.4 X-ray micro-tomography

The assembled Li/S Swagelok© cells were scanned *in-situ* before and after cycling at 0.10 mA/cm^2 current density. The *in-situ* X-ray micro-tomography was performed using a Xradia Versa 520 laboratory micro-tomography instrument. Scans were carried out with the tube voltage set at 50 kV and a low energy filter.

For the scans the source and detector were positioned at the minimum distance to achieve the highest possible intensity, therefore no significant geometric magnification and propagation-based phase contrast effects were expected. 3D datasets were collected at 20X optical magnification in absorption-contrast mode, and a binning of 2 was set on the 2048x2048 px CCD detector, resulting in a pixel size of ca. 780 nm and a field of view of ca. 750 μm.

For each set of tomography data, 1601 radiographic projections were acquired over a 360° sample rotation range. The radiographic projections were collected and reconstructed into a 3D volume using a standard ZEISS Xradia's proprietary cone beam filtered back projection algorithm (XRM Reconstructor). The resulting image stacks for the further image processing were imported into Avizo Lite 9.0 (Visualization Sciences Group, FEI Company).

6.2.5 X-ray nano-tomography

For the *ex-situ* scan, a sample fragment of S composites coated on the stainless steel pins was mounted onto a needle to obtain a sufficiently small sample to match the nano-CT field of view (FOV 65 μm × 65 μm) , consequently the samples was of ca. 65 μm in diameter.

For the *ex-situ* X-ray absorption contrast nano-tomography, a Zeiss Xradia Ultra 810 nano-tomography instrument was employed. Scans were carried out with a micro-focus rotating Cr anode X-ray source (MicroMax-007HF, Rigaku) with the tube voltage set at 35 kV and current at 25 mA, providing pseudo-monochromatic source energy of 5.4keV. In the "large field of view" mode, pixel binning of 2 was set on the 1024x1024 px CCD detector, resulting in a pixel size of the reconstructed tomograms of ca. 126 nm.

6.2.6 Image post-processing, segmentation and analysis

The resulting image stacks reconstructed by a standard filtered back projection algorithm XRM Reconstructor were binarised in Avizo Lite (Visualization Sciences Group, FEI Company) and ImageJ for the image post-processing, segmentation and analysis.

In order to visually compare the relevant scan the rotational variations along the vertical axis between each tomographic scan were tracked. This was done by rotating the datasets axially to face the same orientation by visual identification of characteristic "landmarks" in the separator layer.

For a further image segmentation, histogram equalization was performed, and smoothing filters including non-local means, box and median filter were applied to the grayscale image sequences for image de-noising. For image analysis for each acquired tomographic volume, a cubic region of interest, which is the largest internal volume sulphur cathode excluding separator and lithium anode, was extracted: for samples A and B a subsection internal to the sulphur cathode of dimensions 660 × 680 × 220 voxels was selected that is based on a pixel size of 780 nm is ca. 515.8 μm × 531 μm × 171.93 μm ; for sample C a subsection of 660 x 680 x 265 voxels which based on a pixel size of 780 nm is 515.8 μm x 531 μm x 207.1 μm.

The data were segmented in Avizo by visual thresholding based on the difference between absorption coefficients for a sulphur phase and a binder/carbon/electrolyte phase. Image artefacts are removed by a dilation and erosion method as described in [162]. Following visual segmentation, the sulphur particles were separated by the "Separate Objects" module in Avizo and a "Border Kill" module was used to eliminate particles touching the border. The latter procedure is required for particle size distribution (PSD) studies to ensure that the particles analysed are completely internal to the sample volume.

Morphological parameters of the samples were extracted from the images by "Label Analysis" module in Avizo and binary label fields representing the segmented sulphur phase were exported as TIFF stacks for continuous particle size distribution analysis with

a plugin in ImageJ with the method described in [191]. Particles below the size of 1.5 μm in radius were excluded as they were not visually discernible at the given spatial resolution. The phase fraction was calculated with a Matlab function that averages the phase fraction of each plane horizontal to the z-axis that represents the distance from the current collector.

6.3 Results and Discussion

As the duration of the scan was ca. 24 hours, EIS was performed on sample A before and after scan to ensure that no side effects or self-discharge are taking place in these 24 hours and the X ray tomography does not affect the Li/S system.

Fig, 6.4 shows a visual comparison of the Nyquist plots recorded before and after tomographic scan. It can be seen that the Nyquist plots are very similar with only minor changes. Thus, it can be concluded that no electrochemical processes are taken place while scanning the object.

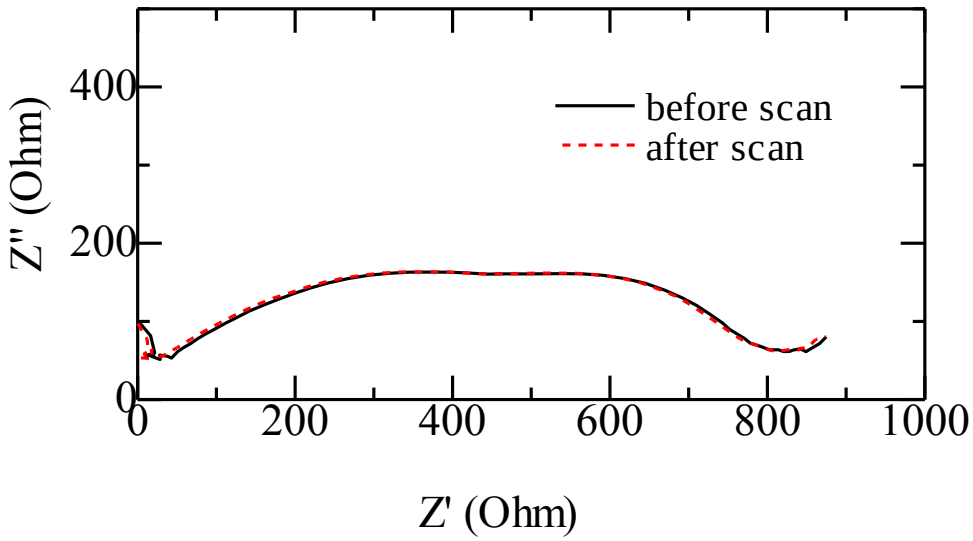

Figure 6.4 Nyquist impedance plots of uncycled Swagelok© Li/S battery, sample A before and after tomographic scan.

6.3.1 *In-situ* micro-tomography

The virtual slices of the same sample were assigned to show sulphur particles in the same spatial positions within the cell.

6.3.1.1 Sample A

Sample A was discharged to 1V and imaged before and after full discharge. **Fig. 6.5** shows virtual slices obtained from the micro-tomography scans of sample A. It could be seen from **Fig. 6.5b** that there no S particles were observed after the full discharge. This is also in agreement with *in-situ* XRD studies done by Canas *et al.* [151] in which they did not detect any peaks of crystalline sulphur after 20% DOD and instead of that some cavities were present on the SEM images of the top layer.

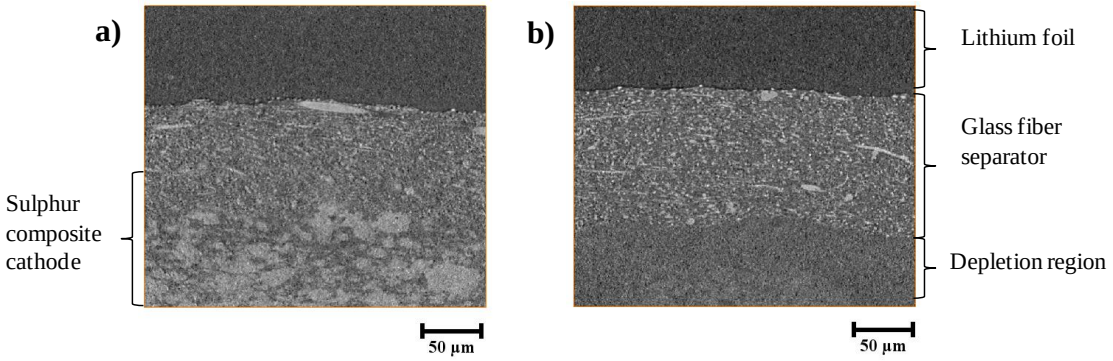

Figure 6.5 from left (a,b) 2D virtual slices from tomography images of Sample A: before and after full discharge at 0.1 mA. Scale bar 50 µm.

Another observation from **Fig. 6.5 a, b** is the expansion of the separator layer from its original thickness that is associated with the increase of liquid state upon cycling and thus the viscosity of the electrolyte.

The discharge profile of Sample A is shown in F**ig 6.6**, from the discharge capacity the active material utilization is only ca. 30%. Additionally some amount of sulphur has dissolved in the electrolyte. However, this does not exclude that some quantity of solid sulphur is still present in smaller sizes which are below the resolution obtainable by micro-tomography. The discharge profile demonstrates the typical Li/S battery behaviour with two characteristic plateaus: short at ~2.3 V representing conversion of elemental

sulphur to higher order polysulphides and long at ~2.1 V representing the conversion of S and higher order polysulphides to Li_2S_2 and Li_2S V.

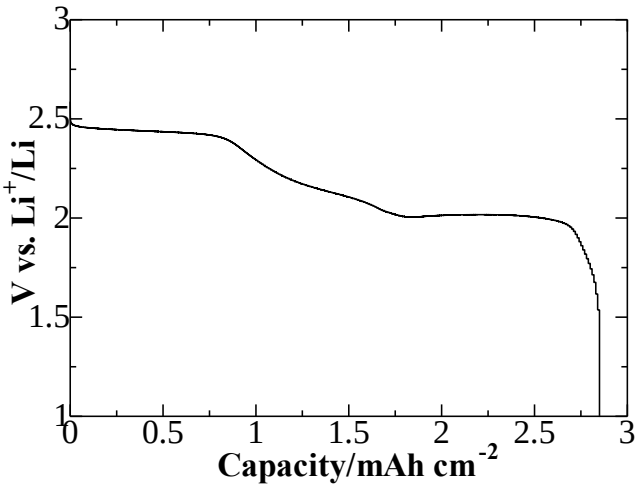

Figure 6.6 Discharge profile of Sample A

6.3.1.2 Sample B

Sample B was discharged to 1.5V and charged to 3V for two cycles and imaged before and after the 2nd cycle. **Fig. 6.7** shows virtual slices obtained from the micro-tomography scans of sample B. In **Fig. 6.7b** sulphur particles are still visible after cycling, but the appearance of a top layer depletion is observed. Expansion of the separator layer from its original thickness after cycling could be also observed. However, one should note, that electrode's wetting was not controlled, although an excess of electrolyte was put in the cell.

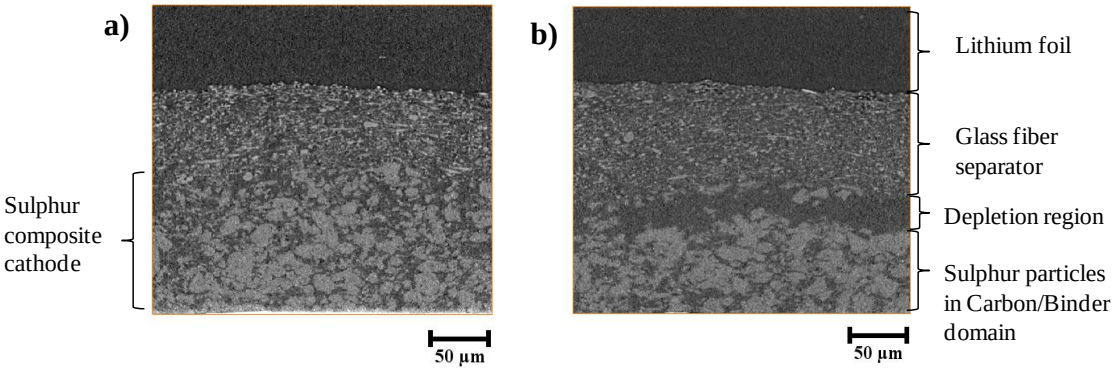

Figure 6.7 from left (a,b) 2D virtual slices from tomography images of Sample B: before and after full discharge at 0.1 mA. Scale bar 50 µm.

The volume rendering for this sample B presented in **Fig. 6.8** shows the retracted sulphur phase. From this image the top layer depletion and sulphur particles agglomeration could be observed.

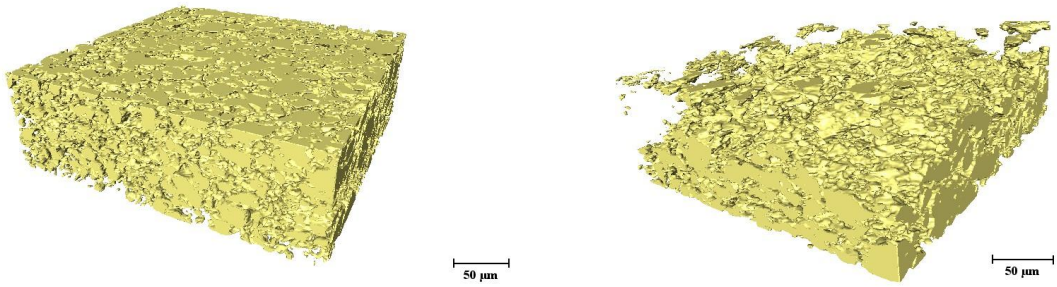

Figure 6.8 Volume rendering of the sulphur phase for (a) the uncycled cathode and (b) for the cathode after 2 cycles. Sample B. Scale bar represents 50 µm

In **Table 6.2** morphological parameters for sample B are summarized, these parameters were not defined for sample A as no S particles were visually observed after the full discharge.

Table 6.2 Morphological parameters obtained from the reconstructed datasets, pixel size for micro-tomography samples is 780 nm.

Cycling state	Sulphur volume (10^7 μm^3)	Sulphur mass loading (mg/cm^2)	Volume specific surface area (μm^{-1})
Uncycled	2.297	17.09	0.255
2 cycles	1.641	12.20	0.178

Afterwards this sample B was cycled for a further 8 cycles. From the cyclability data presented in **Fig. 6.9** it could be seen that there is a profound loss in the discharge capacity after the first cycle and no significant changes upon the following cycles.

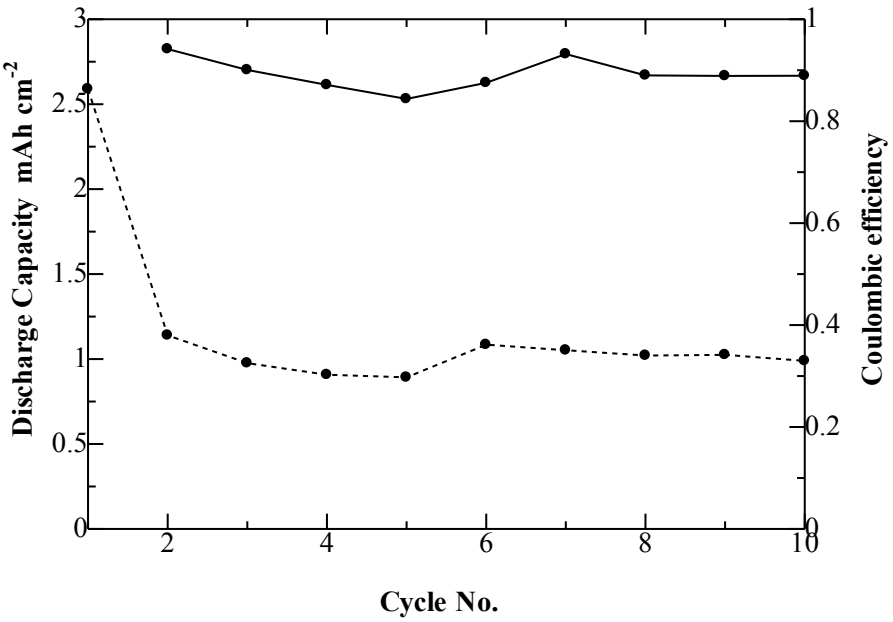

Figure 6.9 Discharge capacity and Coulombic efficiency as a function of cycle's number

6.3.1.3 Sample C

Generally, the electrode morphology changes significantly after the initial cycle and moves towards the equilibrium after second cycle, that correlates to the electrodes' cyclability data as well. Therefore, Sample C was discharged and charged for ten cycles and imaged before and after the 2^{nd} and 10^{th} cycles. The results obtained in this sub-section are presented in [192].

The three virtual slices of Sample C are shown in the **Fig.6.10**. The slices are aligned in the same spatial positions. The appearance of a depletion layer after 2 and 10 cycles can clearly be observed in both the virtual slices as well. The thickness of this depletion layer after 2 and 10 cycles does not change significantly and in some regions become thinner with cycling. This was analysed further as a function of electrode's thickness and presented in **Fig. 6.14**.

The Sample C was further analysed to calculate the sulphur loading and particle size distribution.

The volume renderings of the Sample C electrodes are presented in **Fig. 6.11** with the depletion region along with clear signs of agglomeration of sulphur particles.

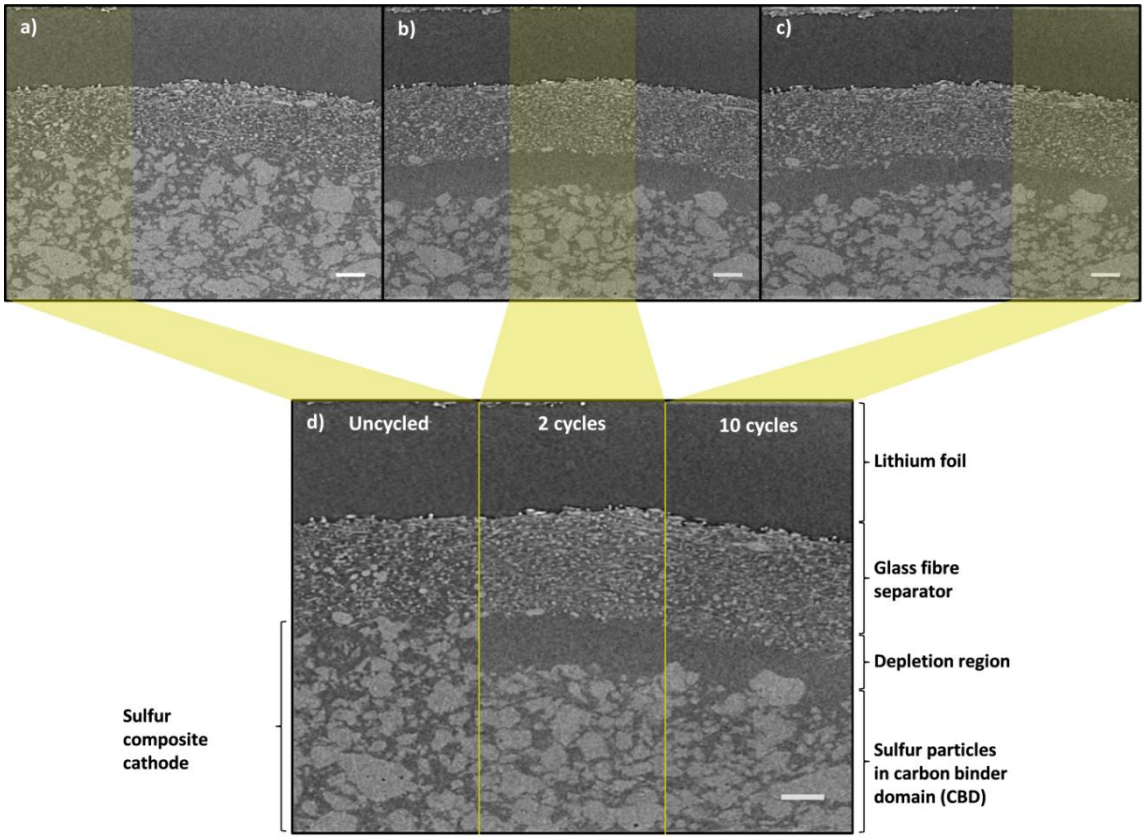

Figure 6.10 from top left (a,b,c) 2D virtual slices from tomography images of Li/S cell before and after cycling for 2 cycles and 10 cycles at 0.1 mA. (d) Combined image of same virtual slice across different cycles. Scale bar 50 μm.

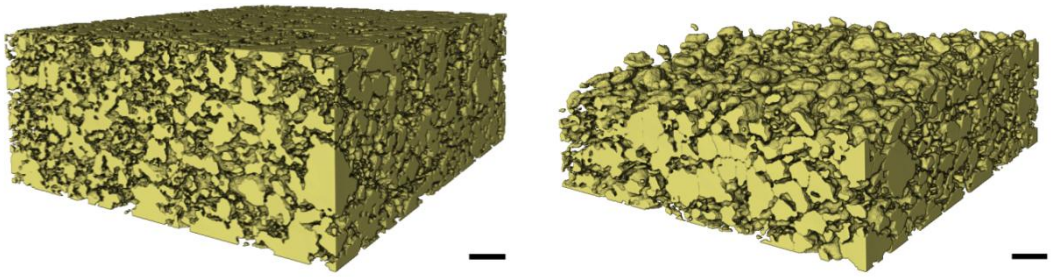

Figure 6.11 Volume rendering of the sulphur phase for a) uncycled cathode and b) the cathode after 10 cycles. Scale bar represents 50 μm

The electrochemical performance of Sample C is presented in **Fig.6.12**. The initial areal capacity of 2.1 mAh cm^{-2} was achieved a significant drop in discharge capacity after the first cycle to around 1.5 mAh cm^{-2} was observed.

Morphological parameters obtained from the reconstructed datasets are presented in **Table 6.3**, sulphur mass loading is presented in terms of mass of sulphur per geometrical surface area of cathode (areal mass loading).

The change in sulphur mass loading for the fresh uncycled and after 2 cycles is in agreement with the charge-discharge data. There is a significant loss of active material is observed from the fresh electrode to the second cycle. However a moderate recovery in sulphur mass loading on the cathode, from 14.18 mg cm^{-2} to 18.73, mg cm^{-2} between the 2nd and 10th cycles does not correlate directly to the charge-discharge data.

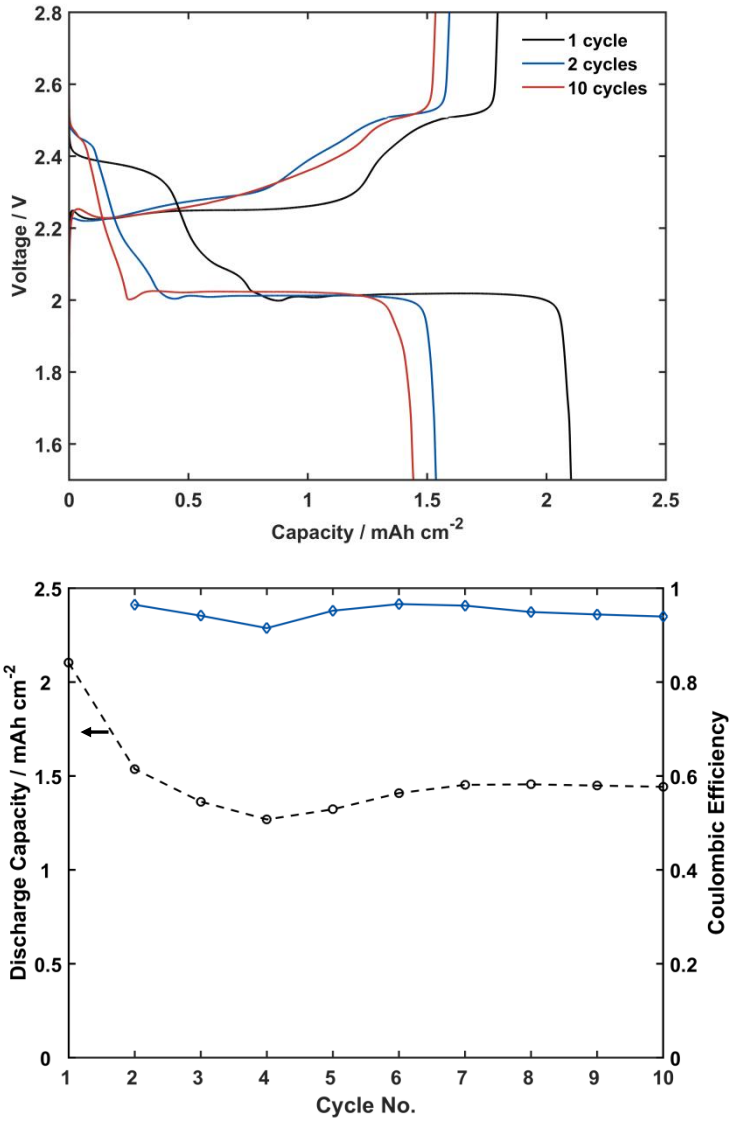

Figure 6.12 a) Charge/Discharge profile for the S-composite cathode after 1, 2 and 10 cycles. b) Discharge capacity and Coulombic efficiency as a function of cycle's number.

During the discharge, the active material leaves the carbon/binder matrix in the form of elemental sulphur and dissolves in the electrolyte as it was discussed above, whereas during charge it forms back to solid state in Li_2S. Thus, during this process we observe

the active material loss; some part is disconnected from the conductive network and that result in carbon/binder phase agglomeration where cavities are taken place. Additionally there is a possibility of nano-sized sulphur particles formations, that are electrochemically active and contribute to the charge discharge processes but are not visible due to the resolution of the used X-ray tomography: solid particles less than 1.5 μm in radius are excluded from the calculation. Also these nano-sized particles tend to agglomerate that might be a reason for a mass recovery observed after 10^{th} cycle.

In **Table 6.3** the values for uncycled sulphur cathode by *ex-situ* nano tomography and by *in-situ* micro tomography vary due to the different imaging conditions of the sample, in particular the different scan resolution. The sample prepared for *ex-situ* nano tomography was not under compression during imaging, therefore the sulphur loading observed is lower than expected.

Table 6.3. Morphological parameters obtained from the reconstructed datasets, pixel size for micro-tomography samples is 780nm and pixel size for nano-tomography sample is 126nm (for equations used to obtain these parameters see Appendix A).

Cycling state	Sulphur volume (10^7 μm^3)	Sulphur mass loading (mg/cm^2)	Volume specific surface area (μm^{-1})
Uncycled	2.804	20.86	0.347
2 cycles	1.848	14.18	0.308
10 cycles	2.439	18.73	0.259
Uncycled (*Ex-situ* nano-tomography sample)	0.00393	4.22	0.646

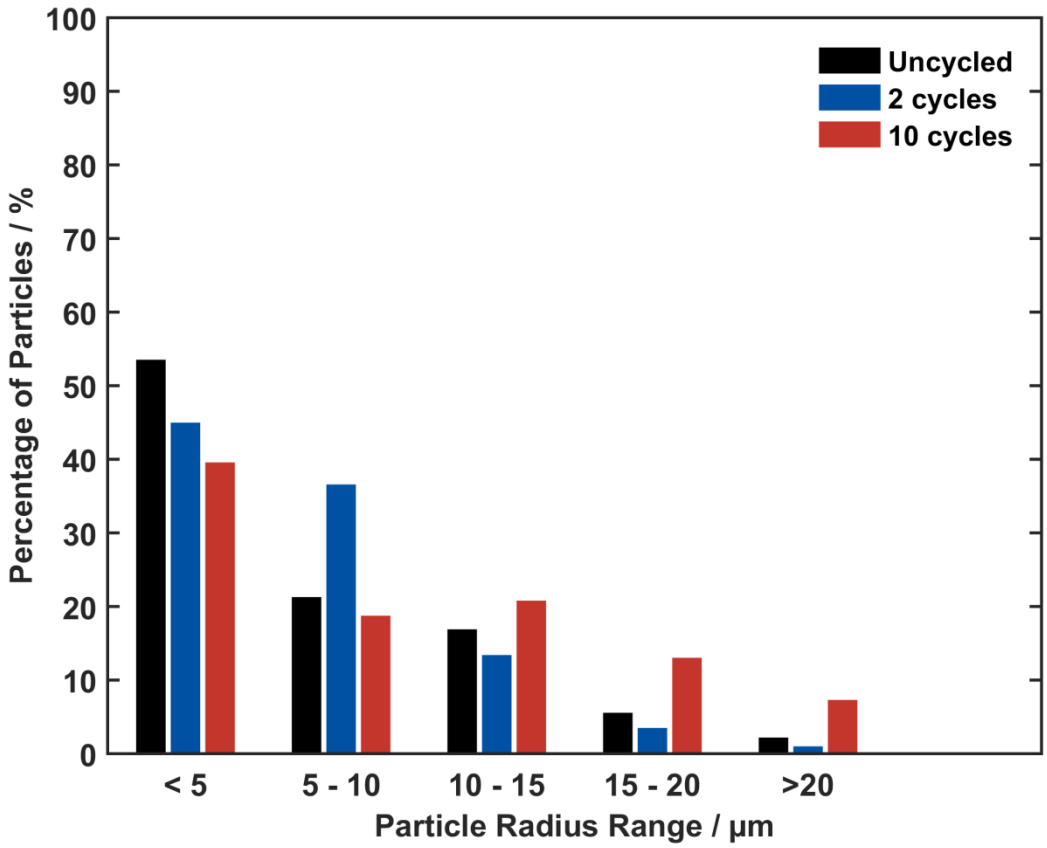

Figure 6.13. Continuous particle size distribution of sulphur particles in Sample C before and after cycling for 2 and 10 cycles

In **Fig. 6.13** the sulphur particles size distribution is shown. It was determined in the sub-volume using a continuous particle size distribution method as proposed by Holzer *et al.* [193]. Initially the sulphur particles were clustered below the 10 µm size range, given the micron sized particles used, but there is a tendency for particle agglomeration upon cycling. The mean particle size radius increases from 6.41 µm for the uncycled electrode to 9.11 µm for the electrode after 10 cycles, which also results from sulphur re-deposition from its original location upon cycling.

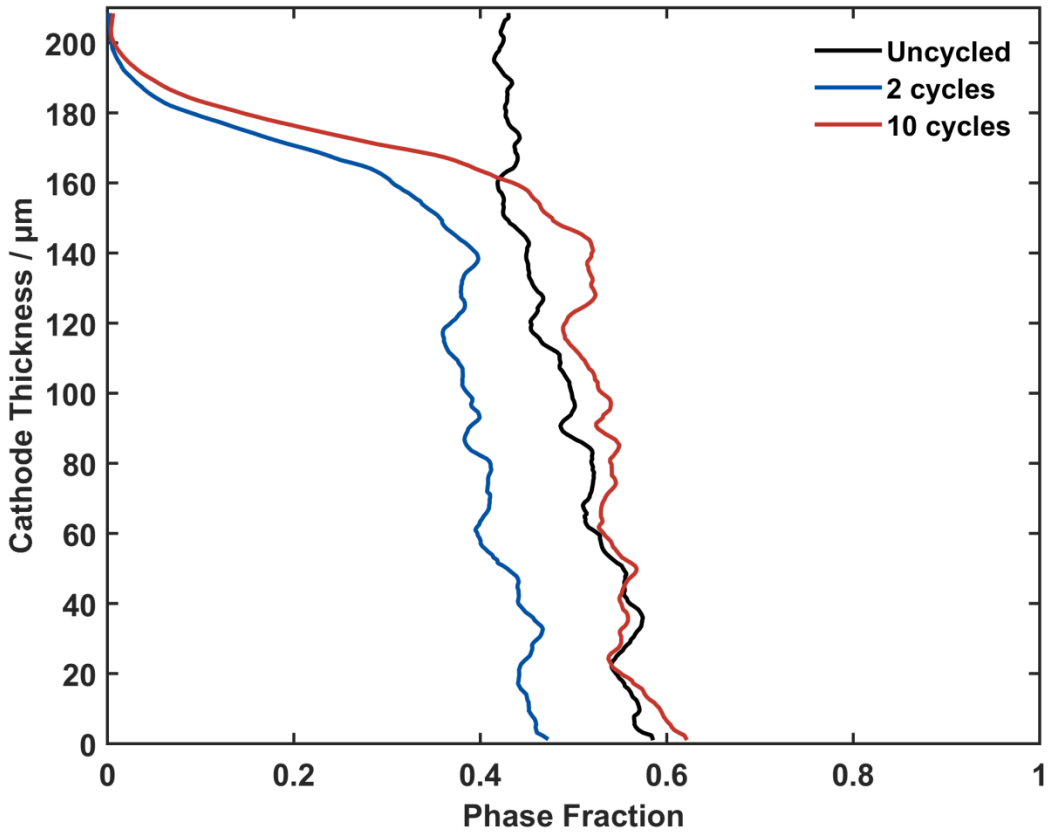

Figure 6.14 Sulphur phase fraction as a function of thickness of the electrode where 0um represents the current collector

The dissolution of sulphur particles upon cycling is uneven, this could be observed visually from the scans and it is supported by the phase fraction as a function of the electrode' thickness which is shown in the **Fig. 6.14.** Sulphur dissolution is particularly evident at the top of the electrode closest to the separator which contains electrolyte.

The initial dissolution of sulphur particles depends on the electrolyte composition and amount, as it dictates the solubility of sulphur and its products. Secondly, sulphur dissolution and re-deposition may occur at the sites with higher electrical conductivity as

opposed to their original locations. Additionally sulphur that is not trapped in the carbon host structure will dissolve first, as well as by mass transport limitations within the thickness of the electrode.

6.3.2 Nano-X ray tomography of S electrodes

In micro-CT *in-situ* imaging, the sulphur phase and the binder/carbon/electrolyte phase were segmented based on absorption coefficients differences; the carbon/binder domain and pore/electrolyte phases are segmented into a single phase due to the limited difference in grayscale contrast.

To distinguish the carbon/binder and pore/electrolyte phases, as well as to better understand the mixing of sulphur and carbon binder phases e*x-situ* Zernike phase contrast nano-tomography was performed on a sample of the as-coated sulphur composite.

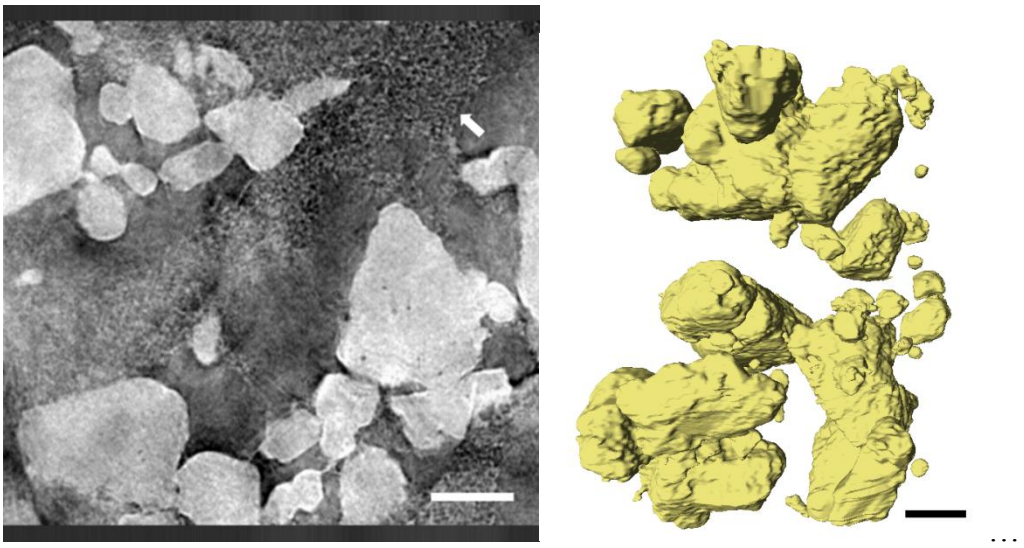

Figure 6.15 left (a) X-ray phase contrast nanotomography on S-composite used (scale bar 10um), carbon binder domain (CBD) indicated by the white arrow; right (b) volume rendering of segmented sulphur particles (scale bar 10um)

The image in **Fig. 6.15a** of the fresh S-C composite sample shows the nano-scopic resolution required for the features of the carbon binder domain (white arrow) to become distinct. Therefore, it is not expected that the morphological detail of carbon/binder domain will be distinguishable under the micro-tomographic datasets, (and instead, for micro-CT, the segmentation is concerned with two phases - the carbon/binder lumped with the pore phase, and the solid sulphur phase). Furthermore it is acknowledged that at the resolution obtainable by micro-tomography, sulphur particles below the resolution limit (i.e. nano sized sulphur particles) will not be detected.

Additionally S composites synthesized in this work for cathode optimization S/PANI/Al_2O_3, S/PANI/ $Mg_{0.6}Ni_{0.4}O$ were also imaged in *ex-situ* Zernike phase contrast in nano-CT.

Fig. 6.16 and 6.17 shows the nano-scale architectures of the Li/S composite, revealing an intimate mixture of the S composite and carbon/binder phases. The image resolution is sufficient to isolate larger particles, and provides further demonstration of the potential of nano-CT to inform the characterisation and optimisation of electrode microstructures across multiple length scales. However, correlative, higher resolution imaging may also be considered in future, to identify the microstructural details of the binder domain which at finer length scales. In this study we have only pursued qualitative description of the obtained images.

Furthermore, as this nano-CT data is collected at a single X-ray energy, it is not possible in the current image to distinguish, by grayscale contrast, the active material and binder domain.

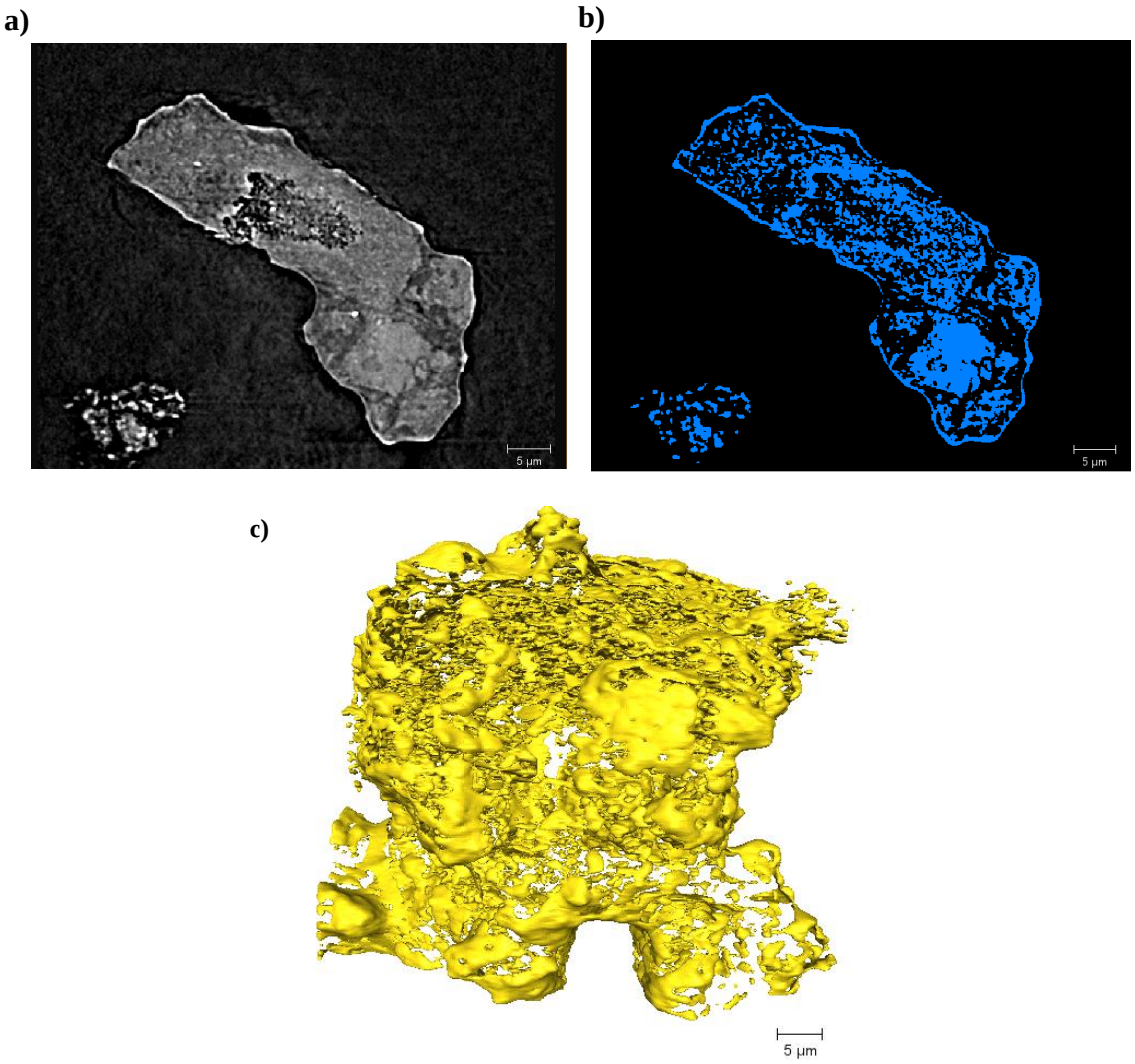

Figure 6.16 Reconstructed slice for top left (a) X-ray phase contrast nanotomography on S-PANI/Al_2O_3 composite electrode (scale bar 5um); right (b) corresponding binary segmented slice; bottom (c) volume rendering of segmented S/PANI/Al_2O_3 (scale bar 5um).

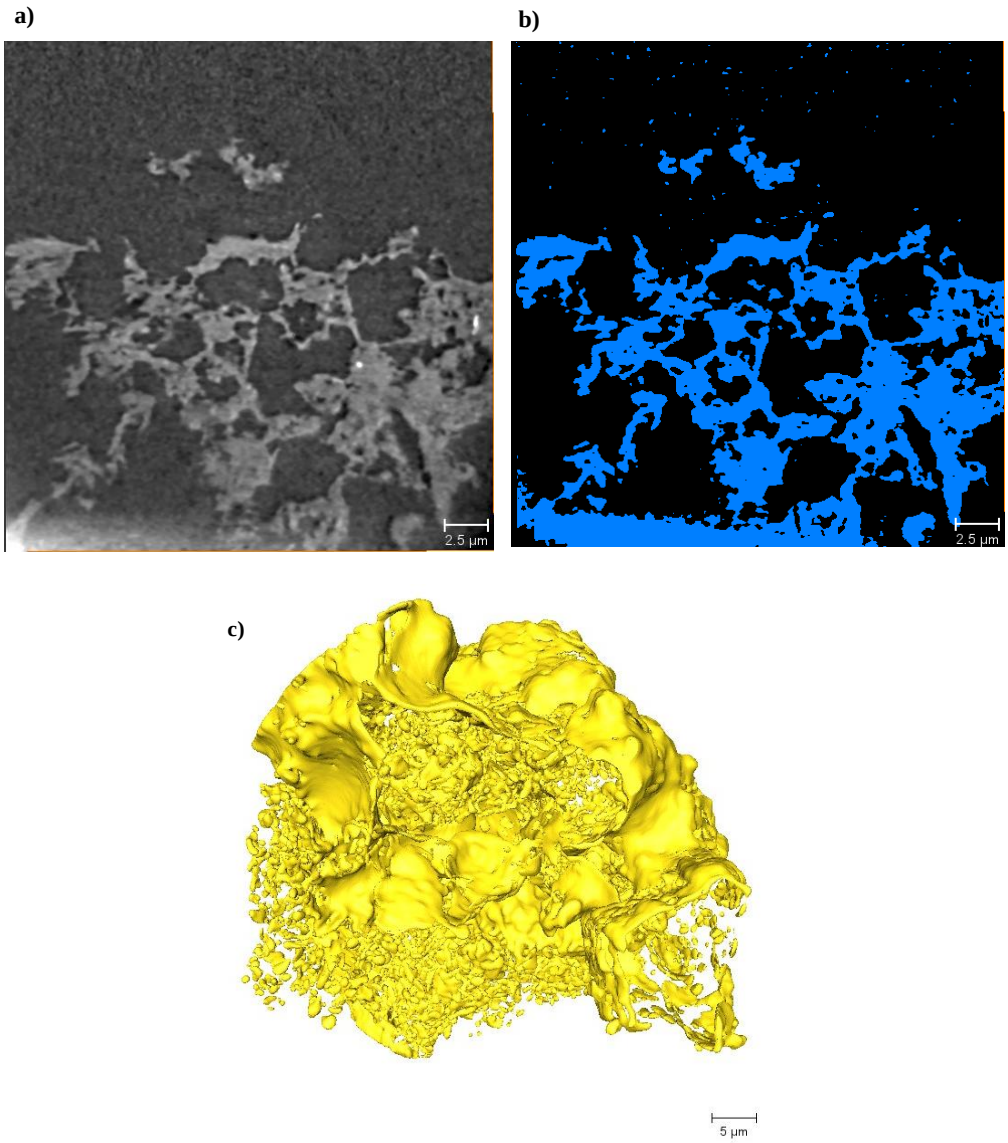

Figure 6.17 Reconstructed slice for top left (a) X-ray phase contrast nano-tomography on S/PANI/ $Mg_{0.6}Ni_{0.4}O$ composite electrode (scale bar 2.5um); right (b) corresponding binary segmented slice; bottom (c) volume rendering of segmented S/PANI/$Mg_{0.6}$ $Ni_{0.4}O$ (scale bar 5um).

Fig. 6.16 reveals the nano-scale architecture of the Li/S composite, revealing an intimate mixture of the S, PANI and Al2O3 phases. The image resolution is sufficient to isolate larger particles, and provides further demonstration of the potential of nano-CT to inform the characterisation and optimisation of electrode microstructures across multiple length scales. However, correlative, higher resolution imaging may also be considered in future, to identify the microstructural detail of the binder domain which occurs at finer length scales.

Furthermore, as this nano-CT data is collected at a single X-ray energy, it is not possible in the current image to distinguish, by grayscale contrast, the active material and binder domain. In future, segmentation of the material phases based on morphology, or by combination of absorption and phase contrast data may aid in the process.

Summary

The study of morphological changes upon cycling in Li/S cells is crucial in order to design the best electrode configuration as the discharge capacity and cycle retention is directly linked with the morphology of the electrodes. To date studies of the morphological changes of Li/S battery were made under *ex-situ* conditions, in contact with air, that reveals the main transformations occurring in the electrode surface. However, to study the real formation and distribution of particles, *in-situ* measurements that will be able to provide 3D image of the electrode are needed.

In this chapter, the Li/S battery was imaged *in-situ* by lab scale micro X-ray tomography instrument to study the structural modifications as a function of electrochemical cycling, additionally fresh composites were imaged in higher resolution to be able to observe nanoscopic particles.

3D reconstructions of the tomographic datasets revealed a layer of sulphur depletion closest to the separator. This suggests that significant mass transport limitations exist within thick film sulphur cathodes. Furthermore, shifts to larger sulphur particle sizes with cycling corroborate previous report of sulphur agglomeration. Nano-tomography data confirms that the nanoscopic length-scale of carbon particles and S composites hinder efforts to segment the CBD in micro-tomography.

It also showed that electrolyte plays an important role; and in future X-ray tomography could be combined with other techniques to study the liquid state in *in-situ* setup, such as UV-vis or FTIR.

To conclude, this *in-situ* methodology allowed direct observation of a battery's morphology within cycling and to track dynamically the bulk changes happening in the battery. X-ray tomography proved to be a powerful tool for Li/S battery investigation, that

should help in understanding the degradation mechanism of Li/S battery and its further optimization.

CHAPTER VII. CONCLUSIONS AND FUTURE WORK

In this chapter the main points of the work are summarized: a summary on battery optimization, characterization and investigation of key parameters for Li/S is provided, with an emphasis on cathode and electrolyte respectively.

The Li/S system has advantages over conventional lithium ion battery owing to its high theoretical capacity of 1675 m Ah $g^{-1}$and has significant potential for applications in EV. Combined with its abundant availability and low environmental impact, this makes sulphur the most promising cathode for lithium batteries for large scale applications as well.

However, there are still challenges that need to be overcome that hinder its successful commercialization. Amongst them, the significant morphology change of the positive electrode state upon cycling that makes this system very different from a conventional intercalation or alloy electrode. A more comprehensive understanding of the system is required for further improvements and optimisation; despite intensive research there are often disagreements in the literature.

A universal reference mechanism, applicable to all Li/S systems does not yet exist, the reason lies in the fact that there are so many parameters (cycling conditions, electrolyte nature, sulphur composite, sulphur to electrolyte ratio, active material loading etc.) which change the equilibrium and the involved reactions.

Aiming to develop Li/S battery in the initial stage of the work we focused on the preparation of positive electrodes and methodology development. Thus the composition of the positive electrode has been considered as described in Chapter 4. Commercially viable cell configurations with conducting polymers polyaniline and polyacrylonitrile were developed by a simple ball milling method. The fabrication process was optimised, resulting in well dispersed and small sulphur particles mixed with conducting agents leading to an improvement in battery performance. The effect of addition of a small amount of $Mg_{0.6}Ni_{0.4}O$ or Al_2O_3 to sulphur/polyaniline composite performance was evaluated.

In particular, high rate charge-discharge capability was obtained for S/PANI/$Mg_{0.6}Ni_{0.4}O$ composite, which demonstrated an initial discharge capacity of ca. 1500 mA h g^{-1} with a retained capacity of ca. 500 m Ah g^{-1}after 100 cycles. It was shown that the addition of $Mg_{0.6}Ni_{0.4}O$ leads to a homogenous electrode morphology; upon cycling this additive helps to retain morphology similar to that of the initial composite cathode. The alumina additive had a lesser enhancement effect, but still improved battery electrochemical performance delivering an initial discharge capacity of ca. 1400 mA h g^{-1} with a retained capacity of ca. 600 m A h g^{-1}after 100 cycles.

Cathodes with Ni foam and Al foil as current collectors showed different cycle performance, with superior performance observed for Ni foam, which may be due to its porous structure. This implies that the electrode morphology has a pronounced effect on the cell performance and the cycling behaviour of rechargeable Li/S is dictated by the evolution of the morphology of the positive electrode.

Chapter 5 describes work on the electrolyte optimisation to find out the effects of varying electrolyte's parameters on battery performance. The optimised cathode with S/PANI/$Mg_{0.6}Ni_{0.4}O$ composite was tested with electrolytes to study the effect of electrolytes parameters varying; including the addition of commonly used lithium nitrate. It is known that $Mg_{0.6}Ni_{0.4}O$ has a polar surface and act as polysulphides absorbing agent, thus it presumably has effect on the electrolyte and participate in the shuttle mechanism. As electrolyte the mixed solution of the 1,3-dioxolane (DOL) and

TEGDME (v/v 1/1) with lithium bis(trifluoromethanesulfonyl) imide (LiTFSI) and TEGDME with LiTFSI were selected. There are two optimisation mechanisms were considered: increasing the salt concentration and addition of lithium nitrate to compare the effect on the cell performance.

In order to evaluate the effect of changing electrolyte parameters the measurement of impedance data over cycling was conducted, additionally symmetrical cells were built and measured by EIS to study solely electrolytes interaction with lithium anode.

In general there is a high dependency of Li/S battery performance on the electrolyte content. It was shown that increasing the electrolyte concentration affected several electrolyte properties including conductivity, viscosity, Li ions solvation capability and it leads to the higher battery performance and stability. However, similar results in terms of battery performance could be achieved with the addition of $LiNO_3$. These results provide evidence of the significant importance of the electrolyte in the Li/S system.

It was shown that choosing the right electrolyte is as important for successful Li/S batteries as the electrodes themselves, as the dissolution of sulphur is an inevitable process in the typical organic electrolytes utilised. The optimised S/PANI/$Mg_{0.6}Ni_{0.4}O$ cathodes demonstrated high capacity and the ability to retain the morphology upon cycling, however with the variation of electrolyte content the battery operation could be improved further. In terms of further work one may consider further optimisation of cathode and electrolyte matching. Simple sulphur electrodes are able to give the results comparable or better than the ones with complex architectures often with the use of expensive precursors, such as hierarchical ordered porous carbons, metal organic frameworks, classical carbon nanotubes, incorporation of the graphene and graphene oxide and etc.

The sulphur content in the developed electrodes could be improved further thus to address the issue of low volumetric energy density. Further work should be conducted to develop cells with lower lithium to sulphur ratios, this may be achieved by increasing the sulphur mass loading. One way that could be considered further is use

of 3D current collector that helps to increase the mass loading and to achieve the mechanical integrity; in general porous current collectors can help to mitigate the electrode volume change issue, whilst providing the same electrode surface area. Further optimization in terms of 3D current collector thickness and porosity, and influence on the system are required.

It is also important to replace the lithium metal anode or protect it in order to operate Li/S battery safely and avoid dendrite formation. In metallic lithium free cells, such as S integrated with pre-lithiated Si or graphite anode or Li_2S with Si or graphite, the compatibility with electrolytes should be considered first and well balanced. Thus the full cell configuration has to be examined, taking into account such parameters as lithium-sulphur and sulphur-electrolyte ratios. These parameters are widely acknowledged today whilst a few years ago they were not even included in the reports.

In a coin cell configuration, where the practical amount of electrolyte is not known, it is difficult to study the effect of sulphur/electrolyte ratio. A standard value could not be applied since it strongly depends on the electrode and electrolyte composition, as well as the nature of separator. It would be a good practice for future works to report these parameters, thus a better comparison between systems could be achieved. Further optimisation could be considered in terms of sulphur-electrolyte ratio and electrolyte content in the cell.

The sulphur content in the developed electrodes could be improved further thus to address the issue of low volumetric energy density. Further work should be conducted to develop cells with lower lithium to sulphur ratios, this may be achieved by increasing the sulphur mass loading.

Chapter 6 focused on the effect of the cathode microstructure on the rate of electrochemical transformation and the penetration depth of electrochemical reactions into the bulk of the positive electrode. That was studied by a novel *in situ* and *ex situ* X-ray tomography technique. Here we aimed to find a correlation between electrodes' morphology and electrochemical performance.

The work presented in chapter 6 provided an insight into the bulk micro-structural characterisation of Li/S battery in *in-situ* set up and provides a proof of concept of the advantages of using X-ray CT to study Li/S battery evolution within cycles.

Further studies on the influence of the composition of the positive electrode and its morphology on the electrochemical performance of the system are required. In terms of further work one may employ nano- X -ray CT for which the electrode geometry must be optimised to fit the field of view.

It was shown that 3-dimensional reconstructions of a Li-S battery electrode can provide valuable data related to the electrode architecture and geometrical parameters. This study could be improved further to study the performance over longer cycle life. For this, it is also important to change the current collector to commonly used Al or carbon-coated Al for a better comparison with literature data and also to avoid the self-discharge effect on stainless steel current collector. Additionally such parameters as sulphur/electrolyte ratio are important to control while scanning the same type of electrode.

Additionally one may consider combining X-ray CT technique with any other spectroscopy methods such as UV-vis or Raman to identify the intermediates while cycling and correlate this data with morphological changes.

Microscopic methods such *in-situ* X-ray tomography, TEM and AFM will be also helpful to study the morphological changes over the cycles and can provide information on the local volume changes.

Another promising approach that has been used in the literature [10] for Li/S cell intermediates identification is analysis of organic electrolyte with UV−visible absorption spectroscopy.

In general while thinking of improving Li/S battery one should consider the whole system and optimisation of only one parameter is not sufficient, limitations of positive electrodes are strongly linked to the electrolyte composition as well as to the lithium anode. Tailoring electrolyte and electrodes parameters is as important in Li/S battery as development of efficient and easy scale-up positive electrode.

DISSEMINATION

The following are peer reviewed publications in which disseminate the work of this thesis:

- Yermukhambetova, A., Tan, C., Daemi, S., Bakenov, Z., Darr, J. A., Brett, D. J. L., Shearing, P. R. (2016). *Exploring 3D microstructural evolution in Li-Sulfur battery electrodes using in-situ X- ray Tomography*, Scientific Reports 6. ARTN 35291. doi:10.1038/srep35291.
- Yermukhambetova, A., Bakenov, Z., Zhang, Y., J.A Darr, J. A., Brett, D. J. L., Shearing, P. R. (2015). *Examining the effect of nanosized $Mg_{0.6}Ni_{0.4}O$ and Al_2O_3additives on S/polyaniline cathodes for lithium–sulphur batteries*, Journal of Electroanalytical Chemistry. doi:10.1016/j.jelechem.2015.10.032.

The following conferences were attended:

- Advances in Li- Battery Research, 2014, Liverpool. Poster: *Sulphur based Composite Cathode Materials for Rechargeable Lithium Batteries*.
- The 2nd International Seminar on Nanomaterials and Advanced Energy Storage Systems, 2014, Nazarbayev University, Astana, Kazakhstan. Presentation: *Sulphur based Composite Cathode Materials for Rechargeable Lithium Batteries.*

REFERENCES

[1] X. Yuan, H. Liu, and J. Zhang, *Lithium-Ion Batteries: Advanced Materials and Technologies (Green Chemistry and Chemical Engineering)*. CRC Press, 2011.

[2] P. Munshi, J. Pichel, and E. Kwei, "ENERGY STORAGE : GAME-CHANGING COMPONENT OF THE FUTURE GRID," no. February, pp. 41–43, 2009.

[3] H. Kawamoto, "Trends of R & D on Materials for High-power and Large-capacity Lithium-ion Batteries for Vehicles Applications," *Sci. Technol. Trends*, vol. 106, pp. 19–33, 2010.

[4] J. Axsen, A. Burke, and K. Kurani, "Batteries for plug-in hybrid electric Vehicles (PHEVs): goals and the state of technology circa 2008," 2008.

[5] L. Lu, X. Han, J. Li, J. Hua, and M. Ouyang, "A review on the key issues for lithium-ion battery management in electric vehicles," *J. Power Sources*, vol. 226, pp. 272–288, Mar. 2013.

[6] S. Al-Thyabat, T. Nakamura, E. Shibata, and A. Iizuka, "Adaptation of minerals processing operations for lithium-ion (LiBs) and nickel metal hydride (NiMH) batteries recycling: Critical review," *Miner. Eng.*, vol. 45, pp. 4–17, May 2013.

[7] D. Eroglu, K. R. Zavadil, and K. G. Gallagher, "Critical Link between Materials Chemistry and Cell-Level Design for High Energy Density and Low Cost Lithium-Sulfur Transportation Battery," *J. Electrochem. Soc.*, vol. 162, no. 6, pp. 982–990, 2015.

[8] X. Ji and L. Nazar, "Advances in Li–S batteries," *J. Mater. Chem.*, vol. 20, no. 44, p. 9821, 2010.

[9] S. Evers and L. Nazar, "New Approaches for High Energy Density Lithium–Sulfur Battery Cathodes," *Acc. Chem. Res.*, vol. 46, no. 5, pp. 1135–1143, May 2013.

[10] C. Barchasz, F. Molton, C. Duboc, J.-C. Leprêtre, S. Patoux, and F. Alloin, "Lithium/sulfur cell discharge mechanism: an original approach for intermediate species identification.," *Anal. Chem.*, vol. 84, no. 9, pp. 3973–80, May 2012.

[11] P. Bruce and S. Freunberger, "Li-O_2 and Li-S batteries with high energy storage," *Nat. Mater.*, vol. 11, no. December 2011, pp. 19–30, 2012.

[12] "Green Car Congress: US DOE awards more than $175M to 40 projects for advanced vehicle research and development." [Online]. Available: http://www.greencarcongress.com/2011/08/doe-20110810.html. [Accessed: 25-Feb-2014].

[13] "Chinese electric car battery technology R & D and market situation of interpretation - ECF Your Window On China Energy Market." [Online]. Available: http://www.energychinaforum.com/news/61841.shtml. [Accessed: 25-Feb-2014].

[14] "Sion Power." [Online]. Available: http://www.sionpower.com/. [Accessed: 05-Feb-2014].

[15] C. Cluzel and C. Douglas, "Cost and performance of EV batteries: Final report for The Committee on Climate Change," 2012.

[16] "Technology | Oxis Energy." [Online]. Available: http://www.oxisenergy.com/technology/. [Accessed: 25-Feb-2014].

[17] E. Peled, Y. Sternberg, A. Gorenshtein, and Y. Lavi, "Lithium-Sulfur Battery : Evaluation of Dioxolane-Based Electrolytes," vol. 136, no. 6, pp. 6–10, 1989.

[18] Y. Zhang, Y. Zhao, K. E. Sun, and P. Chen, "Development in Lithium / Sulfur Secondary Batteries," pp. 215–221, 2011.

[19] C. Barchasz, F. Mesguich, J. Dijon, J.-C. Leprêtre, S. Patoux, and F. Alloin, "Novel positive electrode architecture for rechargeable lithium/sulfur batteries," *J. Power Sources*, vol. 211, pp. 19–26, Aug. 2012.

[20] B. M. L. Rao and J. A. Shropshire, "Effect of Sulfur Impurities on Li/TiS_2

Cells," *J. Electrochem. Soc.*, vol. 128, no. 5, pp. 942–945, 1981.

[21] D. H. Collins, *Modern batteries. An introduction to electrochemical power sources*, Copublishe., vol. 14, no. 4. London, New York: Arnold, 1985.

[22] C. Glaize and S. Geniès, *Lithium Batteries and Other Electrochemical Storage Systems*. Hoboken, NJ USA: John Wiley & Sons, Inc., 2013.

[23] M. Yoshio, R. J. Brodd, and A. Kozawa, Eds., *Lithium-Ion Batteries*. New York, NY: Springer New York, 2009.

[24] T. B. Reddy and D. Linden, *Handbook of Batteries*, 4th editio. McGraw-Hill Professional, 2002.

[25] D. W. Murphy, F. J. DiSalvo, J. N. Carides, and J. V. Waszczak, "Topochemical reactions of rutile related structures with lithium," *Mat. Res. Bull.*, vol. 13, pp. 1395–1402, 1978.

[26] M. Lazzari and B. Scrosati, "An electrolyte cell based on two intercalation electrodes.," *J. Electrochem. Soc.*, vol. 127, pp. 773–774, 1980.

[27] J. Goodenough and K. Mizuchima, "US Patent 4302518," 1981.

[28] M. Armand, "No Title," in *NATO Symp. Materials Adv. Batteries*, 1980, pp. 145–161.

[29] B. L. Ellis, K. T. Lee, and L. F. Nazar, "Positive Electrode Materials for Li-Ion and Li-Batteries †," *Chem. Mater.*, vol. 22, no. 3, pp. 691–714, Feb. 2010.

[30] S. C. Nagpure, B. Bhushan, and S. S. Babu, "Multi-Scale Characterization Studies of Aged Li-Ion Large Format Cells for Improved Performance: An Overview," *J. Electrochem. Soc.*, vol. 160, no. 11, pp. A2111–A2154, Oct. 2013.

[31] M. Winter and J. Besenhard, "Insertion electrode materials for rechargeable lithium batteries," *Adv. Mater.*, no. 10, pp. 725–763, 1998.

[32] T. Ohzuku, A. Ueda, and N. Yamamoto, "Zero-Strain Insertion Material of of Li[Lil/3Tis/3]O4 for Rechargeable Lithium Cells," *J. Electrochem. ...*, vol. 142,

no. 5, pp. 2–6, 1995.

[33] J. Chen, "Recent Progress in Advanced Materials for Lithium Ion Batteries," *Materials (Basel).*, vol. 6, no. 1, pp. 156–183, Jan. 2013.

[34] J.-H. Shin, W. A. Henderson, and S. Passerini, "PEO-Based Polymer Electrolytes with Ionic Liquids and Their Use in Lithium Metal-Polymer Electrolyte Batteries," *J. Electrochem. Soc.*, vol. 152, no. 5, p. A978, 2005.

[35] J. L. Schaefer, Y. Lu, S. S. Moganty, P. Agarwal, N. Jayaprakash, and L. a. Archer, "Electrolytes for high-energy lithium batteries," *Appl. Nanosci.*, vol. 2, no. 2, pp. 91–109, Dec. 2011.

[36] P. B. Balbuena and Y. Wang, Eds., *Lithium-ion Batteries: Solid-electrolyte Interphase*. Imperial College Press, 2004.

[37] R. Spotnitz and J. Franklin, "Abuse behavior of high-power, lithium-ion cells," *J. Power Sources*, vol. 113, no. 1, pp. 81–100, Jan. 2003.

[38] S. Ramdon, B. Bhushan, and S. C. Nagpure, "*In situ* electrochemical studies of lithium-ion battery cathodes using atomic force microscopy," *J. Power Sources*, vol. 249, pp. 373–384, Mar. 2014.

[39] D.-W. Chung, P. R. Shearing, N. P. Brandon, S. J. Harris, and R. E. Garcia, "Particle Size Polydispersity in Li-Ion Batteries," *J. Electrochem. Soc.*, vol. 161, no. 3, pp. A422–A430, Jan. 2014.

[40] D. D. E. R. Wissenschaften and F. L. A. Mantia, "Characterization of Electrodes for Lithium-Ion Batteries through Electrochemical Impedance Spectroscopy and Mass Spectrometry," no. 17848, 2008.

[41] J. Światowska, V. Lair, C. Pereira-Nabais, G. Cote, P. Marcus, and A. Chagnes, "XPS, XRD and SEM characterization of a thin ceria layer deposited onto graphite electrode for application in lithium-ion batteries," *Appl. Surf. Sci.*, vol. 257, no. 21, pp. 9110–9119, Aug. 2011.

[42] S. Miao, M. Kocher, P. Rez, B. Fultz, R. Yazami, and C. C. Ahn, "Local electronic structure of olivine phases of LixFePO4.," *J. Phys. Chem. A*, vol.

111, no. 20, pp. 4242–7, May 2007.

[43] M. Lowe, J. Gao, and H. D. Abruña, “In operando X-ray studies of the conversion reaction in Mn3O4 lithium battery anodes,” *J. Mater. Chem. A*, vol. 1, no. 6, p. 2094, 2013.

[44] J. Li and J. R. Dahn, “An *In Situ* X-Ray Diffraction Study of the Reaction of Li with Crystalline Si,” *J. Electrochem. Soc.*, vol. 154, no. 3, p. A156, 2007.

[45] J. Gao, M. A. Lowe, Y. Kiya, and D. Abru, “Effects of Liquid Electrolytes on the ChargeÀDischarge Performance of Rechargeable Lithium / Sulfur Batteries : Electrochemical and in-Situ X-ray Absorption Spectroscopic Studies,” pp. 25132–25137, 2011.

[46] V. Rossi Albertini, P. Perfetti, F. Ronci, P. Reale, and B. Scrosati, “*In situ* studies of electrodic materials in Li-ion cells upon cycling performed by very-high-energy x-ray diffraction,” *Appl. Phys. Lett.*, vol. 79, no. 1, p. 27, 2001.

[47] a. Senyshyn, M. J. Mühlbauer, K. Nikolowski, T. Pirling, and H. Ehrenberg, “‘*In-operando*’ neutron scattering studies on Li-ion batteries,” *J. Power Sources*, vol. 203, pp. 126–129, Apr. 2012.

[48] J. B. Siegel, X. Lin, A. G. Stefanopoulou, D. S. Hussey, D. L. Jacobson, and D. Gorsich, “Neutron Imaging of Lithium Concentration in LFP Pouch Cell Battery,” *J. Electrochem. Soc.*, vol. 158, no. 5, p. A523, 2011.

[49] M. Itagaki, N. Kobari, S. Yotsuda, K. Watanabe, S. Kinoshita, and M. Ue, “*In situ* electrochemical impedance spectroscopy to investigate negative electrode of lithium-ion rechargeable batteries,” *J. Power Sources*, vol. 135, no. 1–2, pp. 255–261, Sep. 2004.

[50] Y. Zhang, Z. Bakenov, Y. Zhao, A. Konarov, T. N. L. Doan, K. E. K. Sun, A. Yermukhambetova, and P. Chen, “Effect of nanosized Mg0.6Ni0.4O prepared by self-propagating high temperature synthesis on sulfur cathode performance in Li/S batteries,” *Powder Technol.*, vol. 235, pp. 248–255, Feb. 2013.

[51] D. Marmorstein, T. H. Yu, K. A. Striebel, F. R. Mclarnon, J. Hou, and E. J.

Cairns, “Electrochemical performance of lithiumrsulfur cells with three different polymer electrolytes,” pp. 219–226, 2000.

[52] H. Yamin and E. Peled, “Electrochemistry of nonaqueous lithium/sulfur cell,” *J. Power Sources*, vol. 9, pp. 281–287, 1983.

[53] Y. V. Mikhaylik and J. R. Akridge, “Low Temperature Performance of Li/S Batteries,” *J. Electrochem. Soc.*, vol. 150, no. 3, p. A306, 2003.

[54] M. L. B. Rao, “US3413154.pdf.” 1968.

[55] D. Hebert, J., Ulam, “US3043896.pdf.” 1962.

[56] D. Mole, V., Moss, “US3532543.pdf.” .

[57] Y. Jung and S. Kim, “New approaches to improve cycle life characteristics of lithium–sulfur cells,” *Electrochem. commun.*, vol. 9, no. 2, pp. 249–254, Feb. 2007.

[58] D. Aurbach, E. Pollak, R. Elazari, G. Salitra, C. S. Kelley, and J. Affinito, “On the Surface Chemical Aspects of Very High Energy Density, Rechargeable Li–Sulfur Batteries,” *J. Electrochem. Soc.*, vol. 156, no. 8, p. A694, 2009.

[59] H. Yamin, A. Gorenshtein, J. Penciner, Y. Sternberg, and E. Peled, “Lithium Sulfur Battery,” pp. 7–10, 1988.

[60] Y. V. Mikhaylik and J. R. Akridge, “Polysulfide Shuttle Study in the Li/S Battery System,” *J. Electrochem. Soc.*, vol. 151, no. 11, p. A1969, 2004.

[61] Y. Yang, G. Zheng, and Y. Cui, “Nanostructured sulfur cathodes.,” *Chem. Soc. Rev.*, vol. 42, no. 7, pp. 3018–32, Apr. 2013.

[62] X. Ji, K. T. Lee, and L. F. Nazar, “A highly ordered nanostructured carbon-sulphur cathode for lithium-sulphur batteries.,” *Nat. Mater.*, vol. 8, no. 6, pp. 500–6, Jun. 2009.

[63] G. He, X. Ji, and L. Nazar, “High ‘C’ rate Li-S cathodes: sulfur imbibed bimodal porous carbons,” *Energy Environ. Sci.*, vol. 4, no. 8, p. 2878, 2011.

[64] C. Liang, N. J. Dudney, and J. Y. Howe, “Hierarchically Structured

Sulfur/Carbon Nanocomposite Material for High-Energy Lithium Battery," *Chem. Mater.*, vol. 21, no. 19, pp. 4724–4730, Oct. 2009.

[65] R. Elazari, G. Salitra, A. Garsuch, A. Panchenko, and D. Aurbach, "Sulfur-impregnated activated carbon fiber cloth as a binder-free cathode for rechargeable Li-S batteries.," *Adv. Mater.*, vol. 23, no. 47, pp. 5641–4, Dec. 2011.

[66] L. S. Cells, L. Ji, M. Rao, H. Zheng, L. Zhang, O. Y. Li, and W. Duan, "Graphene Oxide as a Sulfur Immobilizer in High Performance," pp. 18522–18525, 2011.

[67] M. Sun, S. Zhang, T. Jiang, L. Zhang, and J. Yu, "Nano-wire networks of sulfur–polypyrrole composite cathode materials for rechargeable lithium batteries," *Electrochem. commun.*, vol. 10, no. 12, pp. 1819–1822, Dec. 2008.

[68] J. Wang, J. Chen, K. Konstantinov, L. Zhao, S. H. Ng, G. X. Wang, Z. P. Guo, and H. K. Liu, "Sulphur-polypyrrole composite positive electrode materials for rechargeable lithium batteries," *Electrochim. Acta*, vol. 51, no. 22, pp. 4634–4638, Jun. 2006.

[69] Y. Fu and A. Manthiram, "Core-shell structured sulfur-polypyrrole composite cathodes for lithium-sulfur batteries," *RSC Adv.*, vol. 2, no. 14, p. 5927, 2012.

[70] Y. Zhang, Z. Bakenov, Y. Zhao, A. Konarov, T. N. L. Doan, M. Malik, T. Paron, and P. Chen, "One-step synthesis of branched sulfur/polypyrrole nanocomposite cathode for lithium rechargeable batteries," *J. Power Sources*, vol. 208, pp. 1–8, Jun. 2012.

[71] X. Liang, Y. Liu, Z. Wen, L. Huang, X. Wang, and H. Zhang, "A nano-structured and highly ordered polypyrrole-sulfur cathode for lithium–sulfur batteries," *J. Power Sources*, vol. 196, no. 16, pp. 6951–6955, Aug. 2011.

[72] J. Li, K. Li, M. Li, D. Gosselink, Y. Zhang, and P. Chen, "A sulfur–polyacrylonitrile/graphene composite cathode for lithium batteries with excellent cyclability," *J. Power Sources*, vol. 252, pp. 107–112, Apr. 2014.

[73] Y. Zhang, Y. Zhao, A. Yermukhambetova, Z. Bakenov, and P. Chen, "Ternary sulfur/polyacrylonitrile/Mg0.6Ni0.4O composite cathodes for high performance lithium/sulfur batteries," *J. Mater. Chem. A*, vol. 1, no. 2, p. 295, 2013.

[74] L. Wang, X. He, J. Li, M. Chen, J. Gao, and C. Jiang, "Charge/discharge characteristics of sulfurized polyacrylonitrile composite with different sulfur content in carbonate based electrolyte for lithium batteries," *Electrochim. Acta*, vol. 72, pp. 114–119, Jun. 2012.

[75] X. Zhao, J.-K. Kim, H.-J. Ahn, K.-K. Cho, and J.-H. Ahn, "A ternary sulfur/polyaniline/carbon composite as cathode material for lithium sulfur batteries," *Electrochim. Acta*, vol. 109, pp. 145–152, Oct. 2013.

[76] L. Xiao, Y. Cao, J. Xiao, B. Schwenzer, M. H. Engelhard, L. V Saraf, Z. Nie, G. J. Exarhos, and J. Liu, "A soft approach to encapsulate sulfur: polyaniline nanotubes for lithium-sulfur batteries with long cycle life.," *Adv. Mater.*, vol. 24, no. 9, pp. 1176–81, Mar. 2012.

[77] J. Jin, Z. Wen, G. Ma, Y. Lu, and K. Rui, "Mesoporous carbon/sulfur composite with polyaniline coating for lithium sulfur batteries," *Solid State Ionics*, vol. 262, pp. 170–173, Oct. 2013.

[78] D.-R. Chang, S.-H. Lee, S.-W. Kim, and H.-T. Kim, "Binary electrolyte based on tetra(ethylene glycol) dimethyl ether and 1,3-dioxolane for lithium–sulfur battery," *J. Power Sources*, vol. 112, no. 2, pp. 452–460, Nov. 2002.

[79] J.-W. Choi, G. Cheruvally, D.-S. Kim, J.-H. Ahn, K.-W. Kim, and H.-J. Ahn, "Rechargeable lithium/sulfur battery with liquid electrolytes containing toluene as additive," *J. Power Sources*, vol. 183, no. 1, pp. 441–445, Aug. 2008.

[80] Y. V. Mikhaylik, "(19) United States (12)," U.S. Pat. 2008/0193835 A1, 2008.

[81] C. Barchasz, J.-C. Lepretre, S. Patoux, and F. Alloin, "Revisiting TEGDME/DIOX Binary Electrolytes for Lithium/Sulfur Batteries: Importance of Solvation Ability and Additives," *J. Electrochem. Soc.*, vol. 160, no. 3, pp. A430–A436, Jan. 2013.

[82] B. D. Katz, M.-Y. Chu, L. C. Dejonghe, and S. J. Visco, “Liquid electrolyte lithium-sulfur batteries,” WO2001057943 A1, 2001.

[83] C. Barchasz, J.-C. Leprêtre, S. Patoux, and F. Alloin, “Electrochemical properties of ether-based electrolytes for lithium/sulfur rechargeable batteries,” *Electrochim. Acta*, vol. 89, pp. 737–743, Feb. 2013.

[84] M. Nagao, Y. Imade, H. Narisawa, T. Kobayashi, R. Watanabe, T. Yokoi, T. Tatsumi, and R. Kanno, “All-solid-state Li–sulfur batteries with mesoporous electrode and thio-LISICON solid electrolyte,” *J. Power Sources*, vol. 222, pp. 237–242, Jan. 2013.

[85] K. Jeddi, K. Sarikhani, N. Taheri, and P. Chen, “Stabilizing lithium / sulfur batteries by a composite polymer electrolyte containing mesoporous silica particles,” *J. Power Sources*, vol. 245, pp. 656–662, 2014.

[86] J. Jin, Z. Wen, X. Liang, Y. Cui, and X. Wu, “Gel polymer electrolyte with ionic liquid for high performance lithium sulfur battery,” *Solid State Ionics*, vol. 225, pp. 604–607, Oct. 2012.

[87] J. Hassoun, J. Kim, D.-J. Lee, H.-G. Jung, S.-M. Lee, Y.-K. Sun, and B. Scrosati, “A contribution to the progress of high energy batteries: A metal-free, lithium-ion, silicon–sulfur battery,” *J. Power Sources*, vol. 202, pp. 308–313, Mar. 2012.

[88] Y. Yang, M. T. McDowell, A. Jackson, J. J. Cha, S. S. Hong, and Y. Cui, “New nanostructured Li2S/silicon rechargeable battery with high specific energy.,” *Nano Lett.*, vol. 10, no. 4, pp. 1486–91, Apr. 2010.

[89] X. He, J. Ren, L. Wang, W. Pu, C. Wan, and C. Jiang, “Electrochemical characteristics of sulfur composite cathode for reversible lithium storage,” *Ionics (Kiel).*, vol. 15, no. 4, pp. 477–481, Aug. 2008.

[90] D. W. H. Rankin, “CRC handbook of chemistry and physics, 89th edition, edited by David R. Lide,” *Crystallogr. Rev.*, vol. 15, no. 3, pp. 223–224, Jul. 2009.

[91] T. H. L. Clarkson, George William Kaye, *Table of Physical and Chemical Constants*, 16, illust ed. Longman, 1995.

[92] "SUPER P® Conductive Carbon Black." [Online]. Available: http://www.timcal.com/scopi/group/timcal/timcal.nsf/pagesref/SCMM-7EVDTT?Opendocument&lang=en. [Accessed: 05-Mar-2014].

[93] "Product Finder Search - AkzoNobel Corporate." [Online]. Available: http://www.akzonobel.com/brands_products/product_search/. [Accessed: 05-Mar-2014].

[94] "Jacobi Carbons - Home." [Online]. Available: http://www.picacarbon.com/. [Accessed: 05-Mar-2014].

[95] "Activated Carbon Solutions - Eurocarb." [Online]. Available: http://www.eurocarb.com/?gclid=CNy72-S9_LwCFanjwgodaTYAoQ. [Accessed: 05-Mar-2014].

[96] "Material Safety Data Sheet." [Online]. Available: http://www.sdk.co.jp/assets/files/english/products/2094/2094_01.pdf. [Accessed: 05-Mar-2014].

[97] "Carbon Products | Products | Showa Denko Group." [Online]. Available: http://www.sdk.co.jp/english/products/137.html. [Accessed: 05-Mar-2014].

[98] "Graphistrength® website." [Online]. Available: http://www.graphistrength.com/en/. [Accessed: 05-Mar-2014].

[99] J. L. Wang, J. Yang, J. Y. Xie, N. X. Xu, and Y. Li, "Sulfur–carbon nano-composite as cathode for rechargeable lithium battery based on gel electrolyte," *Electrochem. commun.*, vol. 4, no. 6, pp. 499–502, Jun. 2002.

[100] Y. Zhao, Y. Zhang, Z. Bakenov, and P. Chen, "Electrochemical performance of lithium gel polymer battery with nanostructured sulfur/carbon composite cathode," *Solid State Ionics*, vol. 234, pp. 40–45, Mar. 2013.

[101] F. Wu, S. X. Wu, R. J. Chen, S. Chen, and G. Q. Wang, "Electrochemical performance of sulfur composite cathode materials for rechargeable lithium

batteries," *Chinese Chem. Lett.*, vol. 20, no. 10, pp. 1255–1258, Oct. 2009.

[102] L. Yuan, H. Yuan, X. Qiu, L. Chen, and W. Zhu, "Improvement of cycle property of sulfur-coated multi-walled carbon nanotubes composite cathode for lithium/sulfur batteries," *J. Power Sources*, vol. 189, no. 2, pp. 1141–1146, Apr. 2009.

[103] Y. Cao, X. Li, I. Aksay, J. Lemmon, Z. Nie, Z. Yang, and J. Liu, "Sandwich-type functionalized graphene sheet-sulfur nanocomposite for rechargeable lithium batteries.," *Phys. Chem. Chem. Phys.*, vol. 13, no. 17, pp. 7660–5, May 2011.

[104] W. Bao, Z. Zhang, Y. Qu, C. Zhou, X. Wang, and J. Li, "Confine sulfur in mesoporous metal–organic framework @ reduced graphene oxide for lithium sulfur battery," *J. Alloys Compd.*, vol. 582, pp. 334–340, Jan. 2014.

[105] Q. Tang, Z. Shan, L. Wang, X. Qin, K. Zhu, J. Tian, and X. Liu, "Nafion coated sulfur–carbon electrode for high performance lithium–sulfur batteries," *J. Power Sources*, vol. 246, pp. 253–259, Jan. 2014.

[106] D. Kumar and R. C. Sharma, "REVIEW ARTICLE ADVANCES IN CONDUCTIVE POLYMERS," *Eur. Polym.*, vol. 34, no. 8, pp. 1053–1060, 1998.

[107] Ю. А. Михайлин, *Электропроводящие полимеры*. Saint Peterburg, 2010.

[108] J. Jagur-Grodzinski, "Electronically conductive polymers," *Polym. Adv. Technol.*, vol. 13, no. 9, pp. 615–625, Sep. 2002.

[109] Y. Fu, Y.-S. Su, and a. Manthiram, "Sulfur-Polypyrrole Composite Cathodes for Lithium-Sulfur Batteries," *J. Electrochem. Soc.*, vol. 159, no. 9, pp. A1420–A1424, Aug. 2012.

[110] F. Wu, J. Chen, R. Chen, S. Wu, L. Li, S. Chen, and T. Zhao, "Sulfur/Polythiophene with a Core/Shell Structure: Synthesis and Electrochemical Properties of the Cathode for Rechargeable Lithium Batteries," *J. Phys. Chem. C*, vol. 115, no. 13, pp. 6057–6063, Apr. 2011.

[111] G.-C. Li, G.-R. Li, S.-H. Ye, and X.-P. Gao, "A Polyaniline-Coated Sulfur/Carbon Composite with an Enhanced High-Rate Capability as a Cathode Material for Lithium/Sulfur Batteries," *Adv. Energy Mater.*, vol. 2, no. 10, pp. 1238–1245, Oct. 2012.

[112] M.-S. Song, S.-C. Han, H.-S. Kim, J.-H. Kim, K.-T. Kim, Y.-M. Kang, H.-J. Ahn, S. X. Dou, and J.-Y. Lee, "Effects of Nanosized Adsorbing Material on Electrochemical Properties of Sulfur Cathodes for Li/S Secondary Batteries," *J. Electrochem. Soc.*, vol. 151, no. 6, p. A791, 2004.

[113] X. Han, Y. Xu, X. Chen, Y.-C. Chen, N. Weadock, J. Wan, H. Zhu, Y. Liu, H. Li, G. Rubloff, C. Wang, and L. Hu, "Reactivation of dissolved polysulfides in Li–S batteries based on atomic layer deposition of Al_2O_3 in nanoporous carbon cloth," *Nano Energy*, vol. 2, no. 6, pp. 1197–1206, Nov. 2013.

[114] Z. Zhang, Y. Lai, Z. Zhang, K. Zhang, and J. Li, "Al_2O_3-coated porous separator for enhanced electrochemical performance of lithium sulfur batteries," *Electrochim. Acta*, vol. 129, pp. 55–61, Feb. 2014.

[115] K. Dong, S. Wang, H. Zhang, and J. Wu, "Preparation and electrochemical performance of sulfur-alumina cathode material for lithium-sulfur batteries," *Mater. Res. Bull.*, vol. 48, no. 6, pp. 2079–2083, Jun. 2013.

[116] Y. J. Choi, B. S. Jung, D. J. Lee, J. H. Jeong, K. W. Kim, H. J. Ahn, K. K. Cho, and H. B. Gu, "Electrochemical properties of sulfur electrode containing nano Al_2O_3 for lithium/sulfur cell," *Phys. Scr.*, vol. T129, pp. 62–65, Dec. 2007.

[117] Y. Zhang, L. Wang, A. Zhang, Y. Song, X. Li, H. Feng, X. Wu, and P. Du, "Novel V2O5/S composite cathode material for the advanced secondary lithium batteries," *Solid State Ionics*, vol. 181, no. 17–18, pp. 835–838, Jun. 2010.

[118] Y. H. Liao, X. P. Li, C. H. Fu, R. Xu, L. Zhou, C. L. Tan, S. J. Hu, and W. S. Li, "Polypropylene-supported and nano-Al_2O_3 doped poly(ethylene oxide)–poly(vinylidene fluoride-hexafluoropropylene)-based gel electrolyte for lithium ion batteries," *J. Power Sources*, vol. 196, no. 4, pp. 2115–2121, Feb. 2011.

[119] S. Cheon, S. Choi, J. Han, and Y. Choi, "Capacity Fading Mechanisms on Cycling a High-Capacity Secondary Sulfur Cathode," pp. 2067–2073, 2004.

[120] B. Jin, J.-U. Kim, and H.-B. Gu, "Electrochemical properties of lithium–sulfur batteries," *J. Power Sources*, vol. 117, no. 1–2, pp. 148–152, May 2003.

[121] J. Sun, Y. Huang, W. Wang, Z. Yu, A. Wang, and K. Yuan, "Application of gelatin as a binder for the sulfur cathode in lithium–sulfur batteries," *Electrochim. Acta*, vol. 53, no. 24, pp. 7084–7088, Oct. 2008.

[122] J. M. Tarascon and M. Armand, "Issues and challenges facing rechargeable lithium batteries.," *Nature*, vol. 414, no. 6861, pp. 359–67, Nov. 2001.

[123] S. S. Zhang, "Liquid electrolyte lithium/sulfur battery: Fundamental chemistry, problems, and solutions," *J. Power Sources*, vol. 231, pp. 153–162, Jun. 2013.

[124] K. Hosaka, O. Shimamura, H. Horie, T. Saito, T. Kinoshita, T. Abe, and N. Kiriu, "Bipolar electrode batteries and methods of manufacturing bipolar electrode batteries," WO 2006061696 A2, 2006.

[125] R. D. Rauh, K. M. Abraham, G. F. Pearson, J. K. Surprenant, S. B. Brummer, and E. I. C. Corporation, "A Lithium / Dissolved Sulfur Battery with an Organic Electrolyte."

[126] N. Azimi, W. Weng, C. Takoudis, and Z. Zhang, "Improved Performance of Lithium-Sulfur Battery with Fluorinated Electrolyte," *Electrochem. commun.*, Oct. 2013.

[127] Z. Deng, Z. Zhang, Y. Lai, J. Liu, J. Li, and Y. Liu, "Electrochemical Impedance Spectroscopy Study of a Lithium/Sulfur Battery: Modeling and Analysis of Capacity Fading," *J. Electrochem. Soc.*, vol. 160, no. 4, pp. A553–A558, Jan. 2013.

[128] M. Barghamadi, A. S. Best, A. I. Bhatt, A. F. Hollenkamp, M. Musameh, R. J. Rees, and T. Rüther, "Lithium–sulfur batteries—the solution is in the electrolyte, but is the electrolyte a solution?," *Energy Environ. Sci.*, vol. 7, no. 12, pp. 3902–3920, Oct. 2014.

[129] S. S. Zhang, “Does the sulfur cathode require good mixing for a liquid electrolyte lithium/sulfur cell?,” *Electrochem. commun.*, vol. 31, pp. 10–12, Jun. 2013.

[130] H. S. Kim and C. S. Jeong, “Electrochemical properties of binary electrolytes for lithium-sulfur batteries,” *Bull. Korean Chem. Soc.*, vol. 32, no. 10, pp. 3682–3686, 2011.

[131] W. Wang, Y. Wang, Y. Huang, C. Huang, Z. Yu, H. Zhang, A. Wang, and K. Yuan, “The electrochemical performance of lithium-sulfur batteries with $LiClO_4$ DOL/DME electrolyte,” *J. Appl. Electrochem.*, vol. 40, no. 2, pp. 321–325, 2010.

[132] S. S. Zhang, “New insight into liquid electrolyte of rechargeable lithium/sulfur battery,” *Electrochim. Acta*, vol. 97, pp. 226–230, May 2013.

[133] S. Urbonaite and P. Novák, “Importance of ‘unimportant’ experimental parameters in Li–S battery development,” *J. Power Sources*, vol. 249, pp. 497–502, Mar. 2014.

[134] L. Suo, Y.-S. Hu, H. Li, M. Armand, and L. Chen, “A new class of Solvent-in-Salt electrolyte for high-energy rechargeable metallic lithium batteries.,” *Nat. Commun.*, vol. 4, p. 1481, Jan. 2013.

[135] E. S. Shin, K. Kim, S. H. Oh, and W. Il Cho, “Polysulfide dissolution control: the common ion effect.,” *Chem. Commun. (Camb).*, vol. 49, no. 20, pp. 2004–6, 2013.

[136] Y. Zhao, Y. Zhang, Z. Bakenov, and P. Chen, “Electrochemical performance of lithium gel polymer battery with nanostructured sulfur/carbon composite cathode,” *Solid State Ionics*, vol. 234, pp. 40–45, Mar. 2013.

[137] X. Yu, J. Xie, Y. Li, H. Huang, C. Lai, and K. Wang, “Stable-cycle and high-capacity conductive sulfur-containing cathode materials for rechargeable lithium batteries,” *J. Power Sources*, vol. 146, no. 1–2, pp. 335–339, Aug. 2005.

[138] H. Wang, W.-D. Zhang, Z.-Q. Deng, and M.-C. Chen, "Interaction of nitrogen with lithium in lithium ion batteries," *Solid State Ionics*, vol. 180, no. 2–3, pp. 212–215, Mar. 2009.

[139] N. Dudney, "Addition of a thin-film inorganic solid electrolyte (Lipon) as a protective film in lithium batteries with a liquid electrolyte," *J. Power Sources*, pp. 176–179, 2000.

[140] Y. M. Lee, N.-S. Choi, J. H. Park, and J.-K. Park, "Electrochemical performance of lithium/sulfur batteries with protected Li anodes," *J. Power Sources*, vol. 119–121, pp. 964–972, Jun. 2003.

[141] T. Kobayashi, Y. Imade, D. Shishihara, K. Homma, M. Nagao, R. Watanabe, T. Yokoi, A. Yamada, R. Kanno, and T. Tatsumi, "All solid-state battery with sulfur electrode and thio-LISICON electrolyte," *J. Power Sources*, vol. 182, no. 2, pp. 621–625, Aug. 2008.

[142] N. Machida, "Electrochemical properties of sulfur as cathode materials in a solid-state lithium battery with inorganic solid electrolytes," *Solid State Ionics*, vol. 175, no. 1–4, pp. 247–250, Nov. 2004.

[143] Y. Huang, J. Sun, W. Wang, Z. Yu, A. Wang, and K. Yuan, "Manufacturing method of positive pole plate of lithium-sulfur cell," CN 101399329, 2009.

[144] H. Sun, X. He, J. Ren, J. Li, C. Jiang, and C. Wan, "Hard carbon/lithium composite anode materials for Li-ion batteries," *Electrochim. Acta*, vol. 52, no. 13, pp. 4312–4316, Mar. 2007.

[145] X. He, J. Ren, L. Wang, W. Pu, C. Wan, and C. Jiang, "Li/S Lithium Ion Cell Using Graphite as Anode," in *ECS Transactions*, 2007, vol. 2, pp. 47–49.

[146] J. Ren, X. He, W. Pu, L. Wang, L. Li, C. Wan, and C. Jiang, "Preparation of lithium sulfureous secondary battery," CN 101420047, 2008.

[147] J. Hassoun and B. Scrosati, "A high-performance polymer tin sulfur lithium ion battery.," *Angew. Chem. Int. Ed. Engl.*, vol. 49, no. 13, pp. 2371–4, Mar. 2010.

[148] L. Yuan, X. Qiu, L. Chen, and W. Zhu, "New insight into the discharge process

of sulfur cathode by electrochemical impedance spectroscopy," *J. Power Sources*, vol. 189, no. 1, pp. 127–132, Apr. 2009.

[149] R. Elazari, G. Salitra, Y. Talyosef, J. Grinblat, C. Scordilis-Kelley, A. Xiao, J. Affinito, and D. Aurbach, "Morphological and Structural Studies of Composite Sulfur Electrodes upon Cycling by HRTEM, AFM and Raman Spectroscopy," *J. Electrochem. Soc.*, vol. 157, no. 10, p. A1131, 2010.

[150] J. Nelson, S. Misra, Y. Yang, A. Jackson, Y. Liu, H. Wang, H. Dai, J. C. Andrews, Y. Cui, and M. F. Toney, "*In Operando* X-ray diffraction and transmission X-ray microscopy of lithium sulfur batteries.," *J. Am. Chem. Soc.*, vol. 134, no. 14, pp. 6337–43, Apr. 2012.

[151] N. a. Cañas, S. Wolf, N. Wagner, and K. A. Friedrich, "In-situ X-ray diffraction studies of lithium–sulfur batteries," *J. Power Sources*, vol. 226, pp. 313–319, Mar. 2013.

[152] S. Xiong, K. Xie, Y. Diao, and X. Hong, "Oxidation process of polysulfides in charge process for lithium-sulfur batteries," *Ionics (Kiel).*, vol. 18, no. 9, pp. 867–872, 2012.

[153] Y. Wang, Y. Huang, W. Wang, C. Huang, Z. Yu, H. Zhang, J. Sun, A. Wang, and K. Yuan, "Structural change of the porous sulfur cathode using gelatin as a binder during discharge and charge," *Electrochim. Acta*, vol. 54, no. 16, pp. 4062–4066, 2009.

[154] H. S. Ryu, H. J. Ahn, K. W. Kim, J. H. Ahn, and J. Y. Lee, "Discharge process of Li/PVdF/S cells at room temperature," *J. Power Sources*, vol. 153, no. 2, pp. 360–364, 2006.

[155] T. D. Hatchard and J. R. Dahn, "*In Situ* XRD and Electrochemical Study of the Reaction of Lithium with Amorphous Silicon," *J. Electrochem. Soc.*, vol. 151, no. 6, p. A838, 2004.

[156] P. R. Shearing, L. E. Howard, P. S. Jørgensen, N. P. Brandon, and S. J. Harris, "Characterization of the 3-dimensional microstructure of a graphite negative

electrode from a Li-ion battery," *Electrochem. commun.*, vol. 12, no. 3, pp. 374–377, Mar. 2010.

[157] Y. K. Chen-Wiegart, P. Shearing, Q. Yuan, A. Tkachuk, and J. Wang, "3D morphological evolution of Li-ion battery negative electrode LiVO2 during oxidation using X-ray nano-tomography," *Electrochem. commun.*, vol. 21, pp. 58–61, Jul. 2012.

[158] S. Waluś, C. Barchasz, J.-F. Colin, J.-F. Martin, E. Elkaïm, J.-C. Leprêtre, and F. Alloin, "New insight into the working mechanism of lithium-sulfur batteries: *in situ* and *operando* X-ray diffraction characterization.," *Chem. Commun. (Camb).*, vol. 49, no. 72, pp. 7899–901, Sep. 2013.

[159] H. L. Wu, L. A. Huff, and A. A. Gewirth, "*In situ* raman spectroscopy of sulfur speciation in lithium-sulfur batteries," *ACS Appl. Mater. Interfaces*, vol. 7, no. 3, pp. 1709–1719, 2015.

[160] M. U. M. Patel, R. Demir-cakan, M. Morcrette, and J. Tarascon, "Li-S Battery Analyzed by UV / Vis in *Operando* Mode," pp. 1177–1181, 2013.

[161] V. Yufit, P. Shearing, R. W. Hamilton, P. D. Lee, M. Wu, and N. P. Brandon, "Investigation of lithium-ion polymer battery cell failure using X-ray computed tomography," *Electrochem. commun.*, vol. 13, no. 6, pp. 608–610, Jun. 2011.

[162] S. Komini Babu, A. I. Mohamed, J. F. Whitacre, and S. Litster, "Multiple imaging mode X-ray computed tomography for distinguishing active and inactive phases in lithium-ion battery cathodes," *J. Power Sources*, vol. 283, pp. 314–319, 2015.

[163] S. Komini, A. I. Mohamed, J. F. Whitacre, and S. Litster, "Multiple imaging mode X-ray computed tomography for distinguishing active and inactive phases in lithium-ion battery cathodes," *J. Power Sources*, vol. 283, pp. 314–319, 2015.

[164] L. Zielke, C. Barchasz, S. Waluś, F. Alloin, J.-C. Leprêtre, A. Spettl, V. Schmidt, A. Hilger, I. Manke, J. Banhart, R. Zengerle, and S. Thiele,

"Degradation of Li/S Battery Electrodes On 3D Current Collectors Studied Using X-ray Phase Contrast Tomography.," *Sci. Rep.*, vol. 5, no. April, p. 10921, 2015.

[165] N. A. Cañas, K. Hirose, B. Pascucci, N. Wagner, K. A. Friedrich, and R. Hiesgen, "Investigations of lithium–sulfur batteries using electrochemical impedance spectroscopy," *Electrochim. Acta*, vol. 97, pp. 42–51, May 2013.

[166] S. S. Zhang and D. T. Tran, "A proof-of-concept lithium/sulfur liquid battery with exceptionally high capacity density," *J. Power Sources*, vol. 211, pp. 169–172, Aug. 2012.

[167] R. K. Patterson, "Automated Pregl-Dumas technique for determining total carbon, hydrogen, and nitrogen in atmospheric aerosols.," *Anal. Chem.*, vol. 45, no. 3, pp. 605–9, 1973.

[168] Y.-X. Yin, S. Xin, Y.-G. Guo, and L.-J. Wan, "Lithium-sulfur batteries: electrochemistry, materials, and prospects.," *Angew. Chem. Int. Ed. Engl.*, vol. 52, no. 50, pp. 13186–200, Dec. 2013.

[169] T. Hang, D. Mukoyama, H. Nara, N. Takami, T. Momma, and T. Osaka, "Electrochemical impedance spectroscopy analysis for lithium-ion battery using Li4Ti5O12 anode," *J. Power Sources*, vol. 222, pp. 442–447, Jan. 2013.

[170] D. Andre, M. Meiler, K. Steiner, H. Walz, T. Soczka-Guth, and D. U. Sauer, "Characterization of high-power lithium-ion batteries by electrochemical impedance spectroscopy. II: Modelling," *J. Power Sources*, vol. 196, no. 12, pp. 5349–5356, Jun. 2011.

[171] V. S. Kolosnitsyn, E. V. Kuzmina, E. V. Karaseva, and S. E. Mochalov, "A study of the electrochemical processes in lithium–sulphur cells by impedance spectroscopy," *J. Power Sources*, vol. 196, no. 3, pp. 1478–1482, Feb. 2011.

[172] Z. Deng, Z. Zhang, Y. Lai, J. Liu, J. Li, and Y. Liu, "Electrochemical Impedance Spectroscopy Study of a Lithium/Sulfur Battery: Modeling and Analysis of Capacity Fading," *J. Electrochem. Soc.*, vol. 160, no. 4, pp. A553–

A558, Jan. 2013.

[173] E. Maire and P. J. Withers, “Quantitative X-ray tomography,” *Int. Mater. Rev.*, vol. 59, no. 1, pp. 1–43, 2014.

[174] S. R. Stock, “Recent advances in X-ray microtomography applied to materials,” *Int. Mater. Rev.*, vol. 53, no. 3, pp. 129–181, 2008.

[175] M. Ebner, F. Marone, M. Stampanoni, and V. Wood, “of Electrochemical and Mechanical,” *Sceince*, vol. 342, no. November, pp. 716–721, 2013.

[176] J. Wang, Y. C. K. Chen-Wiegart, and J. Wang, “In?situ three-dimensional synchrotron x-ray nanotomography of the (de)lithiation processes in tin anodes,” *Angew. Chemie - Int. Ed.*, vol. 53, no. 17, pp. 4460–4464, 2014.

[177] J. N. Weker, N. Liu, S. Misra, J. C. Andrews, Y. Cui, and M. F. Toney, “Insitu nanotomography and *operando* transmission X-ray microscopy of micron-sized Ge particles,” *Energy Environ. Sci.*, vol. 7, no. 8, p. 2771, 2014.

[178] X. Zhao, J.-K. Kim, H.-J. Ahn, K.-K. Cho, and J.-H. Ahn, “A ternary sulfur/polyaniline/carbon composite as cathode material for lithium sulfur batteries,” *Electrochim. Acta*, vol. 109, pp. 145–152, Oct. 2013.

[179] J. Wang, L. Liu, Z. Ling, J. Yang, C. Wan, and C. Jiang, “Polymer lithium cells with sulfur composites as cathode materials,” *Electrochim. Acta*, vol. 48, no. 13, pp. 1861–1867, 2003.

[180] A. Manthiram, Y. Fu, S.-H. Chung, C. Zu, and Y.-S. Su, “Rechargeable Lithium-Sulfur Batteries.,” *Chem. Rev.*, Jul. 2014.

[181] J. Yan, X. Liu, M. Yao, X. Wang, T. K. Wafle, and B. Li, “Long-Life, High-Efficiency Lithium–Sulfur Battery from a Nanoassembled Cathode,” *Chem. Mater.*, p. 150710061753007, Jul. 2015.

[182] N. Azimi, W. Weng, C. Takoudis, and Z. Zhang, “Improved performance of lithium–sulfur battery with fluorinated electrolyte,” *Electrochem. commun.*, vol. 37, pp. 96–99, Dec. 2013.

[183] Y. V. Mikhaylik and J. R. Akridge, “Polysulfide Shuttle Study in the Li/S

Battery System," *J. Electrochem. Soc.*, vol. 151, no. 11, p. A1969, 2004.

[184] Y. Z. Zhang, S. Liu, G. C. Li, G. R. Li, and X. P. Gao, "Sulfur/polyacrylonitrile/carbon multi-composites as cathode materials for lithium/sulfur battery in the concentrated electrolyte," *J. Mater. Chem. A*, vol. 2, no. 13, p. 4652, 2014.

[185] S. S. Zhang, "Role of $LiNO_3$ in rechargeable lithium/sulfur battery," *Electrochim. Acta*, vol. 70, pp. 344–348, May 2012.

[186] S. Xiong, K. Xie, Y. Diao, and X. Hong, "On the role of polysulfides for a stable solid electrolyte interphase on the lithium anode cycled in lithium–sulfur batteries," *J. Power Sources*, vol. 236, pp. 181–187, Aug. 2013.

[187] J. Scheers, S. Fantini, and P. Johansson, "A review of electrolytes for lithium e sulphur batteries," *J. Power Sources*, vol. 255, pp. 204–218, 2014.

[188] D. Aurbach, E. Pollak, R. Elazari, G. Salitra, C. S. Kelley, and J. Affinito, "On the Surface Chemical Aspects of Very High Energy Density, Rechargeable Li–Sulfur Batteries," *J. Electrochem. Soc.*, vol. 156, no. 8, p. A694, 2009.

[189] M. Pharr, K. Zhao, X. Wang, Z. Suo, and J. J. Vlassak, "Kinetics of Initial Lithiation of Crystalline Silicon Electrodes of Lithium-Ion Batteries," 2012.

[190] S. O. O., Taiwo, D. S., Eastwood, P. D., Lee, J. M., Paz-García, Stephen A., Hall, D. J. L., Brett, P. R., "In-Situ Examination of Microstructural Changes within a Lithium-Ion Battery Electrode using Synchrotron X-ray Microtomography O. O. Taiwo," vol. 69, no. 18, pp. 81–85, 2015.

[191] B. Münch and L. Holzer, "Contradicting geometrical concepts in pore size analysis attained with electron microscopy and mercury intrusion," *J. Am. Ceram. Soc.*, vol. 91, no. 12, pp. 4059–4067, 2008.

[192] A. Yermukhambetova, C. Tan, S. R. Daemi, and Z. Bakenov, "Exploring 3D microstructural evolution in Li-Sulfur battery electrodes using in-situ X-ray tomography," *Nat. Publ. Gr.*, no. October, pp. 1–9, 2016.

[193] L. Holzer, B. Muench, M. Wegmann, P. Gasser, and R. J. Flatt, "FIB-

nanotomography of particulate systems - Part I: Particle shape and topology of interfaces," *J. Am. Ceram. Soc.*, vol. 89, no. 8, pp. 2577–2585, 2006.

Appendix – Calculations to tables 6.2 and 6.3

The following equations were used to calculate the morphological parameters for samples A, B and C in chapter 6.

Number of voxels that belong to the sulphur structure was calculated by Avizo after image segmentation in the given subsection:

- for samples A and B a subsection internal to the sulphur cathode of dimensions 660 × 680 × 220 voxels was selected that is based on a pixel size of 780 nm is ca. 515.8 μm × 531 μm × 171.93 μm ;
- for sample C a subsection of 660 x 680 x 265 voxels which based on a pixel size of 780 nm is 515.8 μm x 531 μm x 207.1 μm.

Sulphur volume was calculated based on the voxel volume and the total number of voxels in the subsection:

$$\textit{Voxel volume} = [\textit{pixel size}]^3 = [0.78\ \textit{um}]^3 = 0.477\ \textit{um}^3\ \textit{per one voxel} \quad (9.1)$$

$$\textit{Sulphur volume} = \textit{Voxel volume} \times \textit{total number of voxels} \quad (9.2)$$

The sulphur mass loading can be calculated based on the sulphur density which is 2.04 g cm^{-3} and the loading per one voxel:

$$\textit{The total surface area of the subsection } A = x \times y \times [\textit{pixel size}]^2 \quad (9.3)$$

$$\textit{Number of voxels per surface area} = \textit{the total number of voxels in the subsection/ total surface area of the subsection} \quad (9.4)$$

$$\textit{Sulphur mass loading} = \textit{density of sulphur} \times \textit{voxel volume} \times \textit{voxel loading} \quad (9.5)$$

For example the total number of voxels in the subsection for sample A is 58725000.

Sulphur volume = Voxel volume $\times$ total number of voxels = 2.804×10^7 μm^3

The total surface area of the subsection A = $x \times y \times [\text{pixel size}]^2$ = 660 voxel $\times$ 680 voxel $\times 0.78^2$ pixel = 2.7×10^5 nm^2

Number of voxels per surface area = the total number of voxels in the subsection/ total surface area of the subsection = 2.14×10^2 voxels/nm^2

Mass loading = voxel density of sulphur $\times$ voxel loading = 2.04 g cm^{-3} $\times$voxel volume$\times$voxel loading = 20.86 mg cm^{-2}